SAPIENZA
UNIVERSITÀ DI ROMA

A Fabry-Perot interferometer for ground-based millimetric spectroscopy

Scuola di dottorato 'Vito Volterra' in Scienze Astronomiche, Chimiche, Fisiche, Matematiche e della Terra

Dottorato di Ricerca in Astronomia – XXV Ciclo

Candidate

Barbara Decina

ID number 699589

Thesis Advisor

Dr. Marco De Petris

A thesis submitted in partial fulfillment of the requirements
for the degree of Doctor of Philosophy in Physics

December 2012

Thesis defended on 21 January 2013
in front of a Board of Examiners composed by:

Prof. Fulvio Ricci (chairman)
Prof. Salvatore Capozziello
Prof. Fabio La Franca
Prof. Oscar Straniero
Prof. Marco Castellani

A Fabry-Perot interferometer for ground-based millimetric spectroscopy
Ph.D. thesis. Sapienza – University of Rome

This thesis has been typeset by LaTeX and the Sapthesis class.

Version: 21 January 2013

Author's email: barbara.decina@gmail.com

Contents

Introduzione

Le osservazioni di natura astrofisica e cosmologica a lunghezze d'onda millimetriche e sub-millimetriche costituiscono uno degli strumenti principali per la comprensione della nascita e dell' evoluzione del nostro Universo. Il ruolo della materia oscura e la natura dell'energia oscura possono essere analizzati tramite lo studio delle fasi iniziali dell'evoluzione delle galassie e della formazione stellare, mentre lo studio di asteroidi, dischi protoplanetari e della polvere interstellare porta a una maggiore comprensione della nascita dei sistemi stellari.
In particolare gli ammassi di galassie costituiscono un laboratorio esclusivo, essendo il punto d'incontro per eccellenza tra la cosmologia e l'astrofisica: la loro abbondanza, così come la loro distribuzione spaziale, sono il risultato delle fluttuazioni di densità primordiali. Allo stesso tempo la termodinamica del gas di elettroni contenuto al loro interno fornisce un'opportunità unica per lo studio della fisica dei plasmi. Sebbene storicamente gli ammassi di galassie siano stati osservati principalmente a lunghezze d'onda del visibile e X, negli ultimi decenni è stato possibile osservarli anche in banda millimetrica grazie all'effetto Sunyaev-Zel'dovich, ovvero la distorsione spettrale subita dai fotoni del fondo cosmico a microonde (CMB) ad opera degli elettroni altamente energetici intrappolati al loro interno. Di recente sono stati resi pubblici i primi cataloghi di ammassi di galassie scoperti tramite effetto Sunyaev-Zel'dovich da esperimenti cosmologici che operano da terra (South Pole Telescope, Atacama Cosmology Telescope) e da satellite (Planck). Nonostante le osservazioni astrofisiche in banda millimetrica realizzate da terra siano fortemente perturbate dalla presenza dell'atmosfera terrestre, i telescopi operanti da satellite presentano inevitabilmente limiti stringenti relativi alle loro dimensioni. Tali limiti determinano valori di risoluzione angolare non sempre sufficienti alla determinazione di quelle caratteristiche spaziali tipiche di oggetti così compatti, apprezzabili esclusivamente a piccole scale angolari. Per questa ragione le osservazioni da terra rappresentano, allo stato attuale, l'unica via percorribile per la realizzazione di mappe del cielo ad alta risoluzione. Tutto ciò giustifica lo sforzo compiuto negli ultimi decenni volto all'esplorazione dei siti più stabili e a basso contenuto di vapore acqueo, in particolare ad alta quota o in zone secche, quali ad esempio deserti e/o regioni polari, ideali per ospitare strumenti operanti a lunghezze d'onda millimetriche e sub-millimetriche.
Nel Capitolo 1 verrà presentata la trattazione teorica dell'effetto Sunyaev-Zel'dovich (SZ), che comprende sia la distorsione spettrale dell'intensità della CMB dovuta all'effetto SZ termico, sia il contributo cinematico. Il primo è dovuto allo scattering Compton inverso subito dai fotoni CMB ad opera degli elettroni altamente energetici contenuti all'interno del gas caldo presente negli ammassi di galassie. Il secondo

è invece frutto dell'effetto Doppler causato dalla velocità peculiare dell'ammasso rispetto ai fotoni CMB. Una trattazione relativistica dell'effetto SZ si rende necessaria quando le velocità degli elettroni coinvolti nello scattering diventano prossime alla velocità della luce.
Misure spettroscopiche dell'effetto SZ in prossimità della frequenza di *crossover*, dove l'effetto SZ termico si annulla, permettono di rompere la degenerazione che coinvolge il contributo termico, il termine cinematico e le correzioni relativistiche, disaccoppiando così la degenerazione tra i paramatri caratteristici dell'ammasso, in particolare la temperatura elettronica, la velocità peculiare e lo spessore ottico.
In questo contesto ho sviluppato un interferometro Fabry-Perot allo scopo di rafforzare le potenzialità di MAD (Multi Array of Detectors) un fotometro a 4 canali ottimizzato per osservazioni multi-frequenza dell'effetto SZ che opererà presso l'osservatorio MITO (Millimetre and Infrared Testagrigia Observatory), in Val d'Aosta a 3480 m di quota. Il sistema MAD+FP costituisce una soluzione innovativa in grado di effettuare misure spettroscopiche in prossimità della frequenza di *crossover* dell'effetto SZ.
Come anticipato in precedenza le osservazioni cosmologiche realizzate da terra a lunghezze d'onda millimetriche e sub-millimetriche sono fortemente affette dall'assorbimento dell'atmosfera terrestre e conseguente ri-emissione. Numerose sono le strategie osservative messe a punto per realizzare opportune procedure di calibrazione delle misure astrofisiche e altrettante le soluzioni strumentali tramite cui effettuare statistiche di *site testing*, necessarie per determinare la bontà del sito d'interesse. Spettri sintetici di emissione atmosferica possono essere derivati anche tramite modelli sintetici, in grado di fornire previsioni relative all'emissione atmosferica a partire dai parametri termodinamici caratteristici del sito. La misura di spettri atmosferici diventa comunque necessaria nel momento in cui si voglia validare un modello sintetico per il sito d'interesse.
Uno dei migliori siti al mondo per realizzare misure cosmologiche e astrofisiche in un ampio intervallo spettrale è Dome C, nel plateau Antartico, in cui ha sede la base italo-francese Concordia. Ad oggi non si dispone ancora di un monitoraggio continuo e in un ampio intervallo di lunghezze d'onda dell'emissione atmosferica a Dome C. Proprio per questo nel Capitolo 2 verrà presentato un approccio semi-empirico che consente di calcolare spettri sintetici di emissione atmosferica tramite il modello ATM (Atmospheric Transmission at Microwaves) nell'intervallo spettrale da 100 GHz a 2 THz, a partire dai dati dei radiosondaggi acquisiti nel biennio 2005-2007 dal Routine Meteorological Observations (RMO) Research Project presso la stazione Concordia.
Nel Capitolo 3 descriverò lo spettrometro atmosferico CASPER2 (Concordia Atmospheric SPectroscopy of Emitted Radiation - MITO version), sviluppato appositamente per affiancare le osservazioni cosmologiche realizzate con il telescopio Cassegrain da 2.6 m presso MITO. Verranno presentate le caratteristiche strumentali, le procedure di calibrazione e le prestazioni preliminari verificate durante la campagna osservativa a MITO tenutasi nel mese di Luglio 2010.
La teoria classica e le limitazioni pratiche dell'interferometro Fabry-Perot saranno invece discusse nel Capitolo 4. Tali limitazioni sono principalmente dovute a effetti reali che la teoria classica non tiene in considerazione. In particolare verrà preso in considerazione il fatto che l'intervallo di angoli di incidenza del fascio incidente non

è infinito ma limitato dall'apertura dello strumento, la mancanza di parallelismo tra le lamine e i loro difetti superficiali. Dal punto di vista strumentale, le due lamine riflettenti costituenti l'interferometro Fabry-Perot devono assicuare alta riflettività e allo stesso tempo basso assorbimento. Queste caratteristiche sono ben soddisfatte dalle *mesh*, ovvero griglie metalliche adottate in gran parte degli esperimenti millimetrici come filtri ottici.
Nel Capitolo 5 verranno infine mostrati i risultati sperimentali relativi alle misure di trasmissione del sistema costituito da due *mesh* risonanti in configurazione Fabry-Perot. Essendo le *mesh* caratterizzate da una riflettività e da uno sfasamento in riflessione dipendenti dalla frequenza, la frequenza di risonanza dell'interferometro Fabry-Perot non coincide con quella prevista dalla teoria classica. Tre diversi setup sperimentali saranno sviluppati al fine di fornire una attenta caratterizzazione della risposta in frequenza di un sistema ottico così innovativo. I risultati sperimentali saranno inoltre messi a confronto con le previsioni ottenute tramite il *software* HFSS (High Frequency Structure Simulator) della Ansoft Corporation, uno strumento molto utile per esplorare la risposta in frequenza di sistemi ottici complessi. Una volta verificato l'accordo tra le due strategie, si potrà sfruttare HFSS per mettere a punto la geometria della *mesh* definitiva, in funzione della risposta in frequenza desiderata.

Introduction

Astrophysical observations at millimeter and sub-millimeter wavelengths are one of the most useful tools to understand the history of the Universe. The role of dark matter and the nature of dark energy can be evaluated probing the early stages of galaxies evolution and star-formation while the study of asteroids, protoplanetary disks and interstellar dust leads to a better understanding of star systems formation. In particular galaxy clusters represent an exclusive physics laboratory being a crossroads of cosmology and astrophysics: their abundance and spatial distribution are the result of the primordial density fluctuations while the thermodynamics of the intergalactic medium is an opportunity for testing plasma physics. Even if they have been observed mainly in optical and X-rays, in the last decades they have been observed also at millimeter wavelengths by means of the Sunyaev-Zel'dovich effect, due to the distortion of the Cosmic Microwave Background (CMB) photons passing through the hot intra cluster gas on its way. Ongoing ground based millimeter surveys like South Pole Telescope or Atacama Cosmology Telescope and space missions like Planck have recently released the first high redshift and massive clusters catalogs discovered by the Sunyaev-Zel'dovich effect. Although ground-based observations are affected by the presence of the Earth atmosphere, space telescopes remain limited in size offering only modest angular resolution not suitable to detect small spatial features of so compact objects. To date the ground-based solution seems to be the only feasible way to perform high angular resolution deep sky surveys. As a consequence an effort is required for the exploration of the driest and most stable sites on Earth, suitable to host mm and sub-mm astronomical instrumentation.

In Chapter 1 the theoretical treatment of the Sunyaev-Zel'dovich effect is provided, considering both the spectral distortion of the CMB intensity due to thermal Sunyaev-Zel'dovich (tSZ) effect and the kinematic SZ (kSZ) effect. The first is due to the scattering of CMB photons by the free electrons of the hot ionized gas in galaxy clusters, while the second is due to the Doppler shift of the CMB spectrum due to the peculiar velocity of the hot gas with respect to the CMB. A relativistic treatment of SZ effect (rSZ) has also to be included due to the high velocities of scattering electrons of the hot intracluster gas. Measurements spanning the crossover frequency, *i.e.* the null of the thermal effect, are needed to break the degeneracies among tSZ spectrum and rSZ or kSZ spectra, allowing the disentangle of the degeneracies among cluster parameters like electrons temperature, peculiar velocity or optical depth and foregrounds (mainly atmospheric emission for ground-based instruments and also galactic synchrotron, bremsstrahlung and IR emission of galactic dust from space). In this context a Fabry-Perot Interferometer (FPI) has been de-

veloped in order to improve the capabilities of MAD (Multi Array of Detectors), a 4-channel photometer optimized for multi-frequency observation of SZ effect that will operate at Millimetre and Infrared Testagrigia Observatory (MITO), a 2.6-m in diameter telescope located in the Alps in Val d'Aosta (3480 m a.s.l.). The FPI, reducing the instantaneous bandwidth, limits the photon background on the detectors and the photon noise mainly due to atmospheric emission at mm wavelengths adding an hybrid solution with spectroscopic capabilities operating in correspondence to the crossover frequency.
As discussed before, cosmological observations from ground at mm and sub-mm wavelengths are affected by atmospheric absorption and consequent emission. Carefully observational strategies and instrumental solutions are needed for accurate calibration procedures as well as for site testing statistics. Atmospheric synthetic spectra, derived by models, are an useful tool to predict atmosphere emission starting from thermodynamic parameter values. The validation of the model for a specific site is mandatory and this is possible only when on-site recorded spectra are available. Dome C, on the Antarctic plateau, is considered one of the best sites in the world to perform observations in a wide spectral range. Anyway a continuous and spectrally wide atmospheric monitoring at Dome C has not yet been performed. In the absence of such measurements, in Chapter 2 we suggest a semi-empirical approach to perform an analysis of atmospheric transmission and emission at Dome C. Radiosoundings data provided by the 2005-2007 dataset of the Routine Meteorological Observations (RMO) Research Project at Concordia station are employed to feed ATM (Atmospheric Transmission at Microwaves) code to generate synthetic spectra in the wide spectral range from 100 GHz to 2 THz.
The spectrometer CASPER2 (Concordia Atmospheric SPectroscopy of Emitted Radiation - MITO version) has been developed specifically to record atmospheric spectra assisting cosmological observations with the 2.6-m in diameter Cassegrain telescope at MITO. The design, the procedure to calibrate the instrument and preliminary performance of the instrument checked during the summer observational campaign at MITO in July 2010 are presented in Chapter 3.
The theory and the practical limitations of the FPI will be discussed in Chapter 4. This limitations are mainly related to the finite range of angles of incidence passing through the instrument, the lack of parallelism of the plates as well as the lack of flatness of the plate surfaces and surface defects of the plates. From the instrumentation standpoint, the two reflective elements of the FPI requires high reflectivity coupled with low absorption loss. These requirements are satisfied by metal meshes, currently adopted in the mm and sub-mm ranges as optical filters in many ground, balloon and space-based instruments.
In Chapter 5 the transmission response of an innovative system composed of two resonant metal grids in a FPI configuration is explored. Since the arrays have a frequency dependent reflectivity and phase, they produce a shift of the frequency of the Fabry-Perot modes from that predicted by the classical model that needs to be characterized. On the other hand, the comparison among experimental results and the Ansoft Corporation software HFSS (High Frequency Structure Simulator) modeling allows to predict and tune the response of metal meshes, reducing the financial costs that the production of several grids geometries would requires.

Chapter 1

Measurements of CMB comptonization towards galaxy clusters

Many key topics in modern astronomy and cosmology, such as galaxy formation and evolution, the amount and role of dark matter and dark energy in the universe, star formation, protoplanetary disks, or the properties of cold debris at the outskirts of the solar system, are related to radiative phenomena in the millimeter and sub-millimeter bands.
The development of sensitive detectors, large cameras, polarization sensitive devices and spectroscopically capable instrumentation have notably improved observations in this fields during the last two decades.
One only needs to think of the measurement of the intensity and polarization power spectra of the Cosmic Microwave Background (CMB) at millimeter (mm) wavelengths, the discovery and the characterization of the optically elusive sub-millimeter (sub-mm) galaxy population or the recent galaxy cluster surveys through sub-arcminute resolution observations of the Sunyaev-Zel'dovich (SZ) effect, *i. e.* the inverse Compton scattering between CMB photons and free electrons.
The SZ effect is undoubtedly one of the best known cosmological probe, useful to study the evolution of structures in the Universe, the nature of dark energy and the physics that drives galaxies formation. The CMB photons detected today have traveled across the universe from the last scattering surface to us, interacting with matter along their path. While the primary CMB anisotropies are due to the gravitational redshift at large angular scales, the secondary anisotropies are generated by the interactions between CMB photons and matter. In particular SZ effect is a secondary anisotropy caused by the interaction between the CMB photons and the free electrons of the hot intra-cluster medium (ICM) of galaxy clusters.
With 10-meter and 6-meter primary reflectors, the South Pole Telescope (SPT) and the Atacama Cosmology Telescope (ACT) are currently the largest CMB survey telescopes providing the highest resolutions.
Both of them performed deep surveys covering hundreds of square degrees searching for massive galaxy clusters to high redshift and capable of detecting many tens to hundreds of SZ clusters data [120], [45].

Figure 1.1. The galaxy cluster Abell 1835 is visible both in the X-ray band via thermal bremsstrahlung (left panel) and from its distortion of the CMB (tSZ effect in the right panel). The three images have the same spatial scale (5.2 arcmin or 1.2 Mpc).

Unfortunately ground-based observations in the mm and sub-mm band are usually affected by the transparency of the atmosphere and its stability over time, mainly because of the presence of large, time-dependent features both in the emission and absorption spectrum of the water vapor (see Sec. 1.4). Of course, this issue can be strongly reduced when operating on stratospheric balloon-borne or airborne detectors, and fully prevented when moving detectors on spacecrafts. BOOMERANG, BLAST, SOFIA, *Planck* and *Herschel* have proven the strength of mm and sub-mm observations from the stratosphere and from space, providing ground breaking advancements in their respective fields at the time of their operation [79], [66], [128], [109], [86]. Anyway the practical limitations on the telescope size, the weight and the accessibility of instrumentation still make substantially unfeasible the deployment of large telescopes on balloons, aircrafts or satellites.
As a matter of fact, the ground-based solution appears presently the only viable way to routinely perform high angular resolution observations of compact objects and small spatial and spectral features at mm and sub-mm wavelengths [42].
The theoretical treatment of the SZ effect are provided in Sections 1.1.1 and 1.1.2 while the current status and future prospects of SZ science are discussed in Sec.1.2. The description of the instrumental strategy developed in this thesis is presented in Sec. 1.3. Finally the strategies adopted to perform a careful monitoring of atmospheric performance are discussed in Sec. 1.4.

1.1 The Sunyaev Zel'dovich effect

The Sunyaev Zel'dovich effect takes place when CMB photons interact with high energy electrons of the ICM of galaxy clusters [9], [15]. The spectrum of the SZ effect is an important source of information. It can be approximated by the sum of two components with the strongest being the thermal SZ effect (tSZ), caused by the scattering of photons by the random motion of free electrons of a hot ionized gas along the line of sight (Sec. 1.1.1). The kinematic SZ effect (kSZ), due to the peculiar velocity of the ICM with respect to the CMB rest frame, is expected to be

much weaker if peculiar velocities are less than 1000 km s^{-1}.
In the former case, the resultant CMB photons have a unique spectral dependence. In the case of kSZ effect the final spectrum remains Planckian since it only Doppler shifts the incident spectrum. It appears as a decrement at all frequencies for a cluster that is receding with respect to the Hubble flow, and an increment at all frequencies for a cluster that is approaching.
Measurements that span the null of the thermal effect would be in principle able to separate the two effects, allowing the determination of the cluster peculiar velocity along the line of sight.

1.1.1 The thermal SZ component

Clusters of galaxies are the largest objects that have had time to collapse under the influence of their own gravity in the Universe. They have masses of about 10^{14} solar masses and a gravitational radius of about 1 Mpc. The electron temperature T_e of the gas in hydrostatic equilibrium within the cluster gravitational potential is $k_B T_e \approx$10 keV ($T_e = 10^{\ 7}$ K) providing the well-known strong X-ray thermal emission, composed of thermal bremsstrahlung and line radiation.
The inverse Compton-scattering of CMB photons when they interact with the hot electrons of the intra-cluster medium in a cluster of galaxies boosts the energy of the CMB photons providing a temperature anisotropy due to the tSZ effect of about 10^{-4}. The tSZ effect leads to a decrease in the intensity of the CMB in the Rayleigh Jeans region and an increase at higher microwave frequencies (see Fig. 1.3 [90]). Thus the modified spectrum cuts the original CMB Planck spectrum at the crossover frequency ν_0 which is typically 217 GHz but this value depends on the temperature of the ICM.
In Fig. 1.1 a comparison among X-rays luminosity measured by Chandra X-ray Observatory and SZ signal measured by the Sunyaev Zel'dovich Array for Abell 1835 (z = 0.25) is shown [3] [22].
The spectral distortion of the CMB intensity due to the SZ effect along the line of sight is given by:

$$\Delta I_T(x) = I_0 \frac{x^3}{e^x - 1} \left[\phi(x, T_e) - 1\right] \tau \tag{1.1}$$

where $x = \frac{h\nu}{k_B T_{CMB}}$, $I_0 = 2\frac{(k_B T_{CMB})^3}{(hc)^2}$, n_e is the electron number density and $\tau = \int n_e \sigma_T dl$ is the optical depth of the cluster to the Thomson scattering.
In the non relativistic limit the term $[\phi(x, T_e) - 1]$ is given by:

$$\phi(x, T_e) - 1 = \frac{x e^x}{e^x - 1} \left[x \frac{e^x + 1}{e^x - 1} - 4\right] \frac{k T_e}{m_e c^2} \tag{1.2}$$

The thermal SZ spectral feature for a typical galaxy cluster is the black solid line in Fig. 1.2. The Compton y-parameter is defined as the integral of the pressure along the line of sight:

$$y = \int n_e \frac{k_B T_e}{m_e c^2} \sigma_T dl \tag{1.3}$$

It represents a useful quantity because it is a frequency independent measure of the magnitude of the SZ signal in a cluster that, unlike ΔI, allows direct comparisons with other experiments.
The exact treatment of SZ effect in clusters needs a relativistic calculation because of the high velocities of ICM electrons. The intensity change can be written as follows [94]:

$$\Delta I = \frac{2k^3T^3}{h^2c^2}\frac{x^4e^x}{(e^x-1)^2}\int d\tau[\theta f_1(x) - \beta + R(x,\theta,\beta)] \tag{1.4}$$

where $\theta = \frac{k_B T_e}{m_e c^2}$ and $\beta = \frac{v_P}{c}$. The first term of the sum in square brakets is due to tSZ effect (see Eq. 1.1) while the second term is due to kSZ (see Eq. 1.5). The function $R(x,\theta,\beta)$ includes the additional dependence on frequency, temperature and velocity obtained in the relativistic treatment. In the more general case, the first term in Eq. 1.4 still dominates over the other two, except near the crossover frequency, whose value generally depends on T_e. In Fig. 1.2 the relativistic corrections to SZ spectrum are shown: they become large near the SZ effect peaks and near the crossover frequency. The percent variation of the SZ flux for a galaxy cluster with T_e=15 keV turns out to be 18% at the maximum of SZ spectrum while the shift in the position of the null for such a cluster is not negligible (about 5%) [130].
In principle, by performing SZ measurements it is possible to explore the thermodynamical history of the hot gas in clusters, with comparable sensitivity and smaller observational bias with respect to the best available X-ray measurements. This is due to the fact that the pressure profile of a galaxy cluster, directly proportional to the electron number density rather than to its square power (like in the bremsstrahlung process which determines X-ray emission), exhibits a slower decline towards the cluster outskirts; moreover, the amplitude of the SZ signal is not affected by cosmological extinction like all the emission processes; in addition, the thermal SZ is observable at the characteristic frequencies of the CMB (i.e. from the radio to the submm region), where it is quite easily disentangled from local and astrophysical contamination thanks to its unique spectral features. Thanks to these properties, CMB measurements from large telescopes are a powerful tool to identify galaxy clusters even at high redshifts, beating the sensitivity and field of view limitations of X-ray surveys. In other words, while for X-Ray galaxy clusters surveys the mass threshold increases continuously with redshift, SZ surveys have a mass threshold which has very little dependence on redshift. This means that at higher redshift a cluster is easier to find using SZ than X-Rays.
Since the integrated Compton parameter over the cluster solid angle is a direct measure of the ICM pressure, simple thermodynamical considerations (under the assumption of self similar structure formation) allow to establish a direct correlation between the total thermal SZ effect from a cluster and the object total mass [24]. Deep SZ cluster surveys, complemented by independent mass estimates, can be used to calibrate the mass-comptonization scaling law allowing to measure cluster masses up to high redshifts and setting tight constraints on the cosmological parameters affecting the cluster mass function [122].
Additionally, SZ spectral measurements can be used to determine the cluster gas

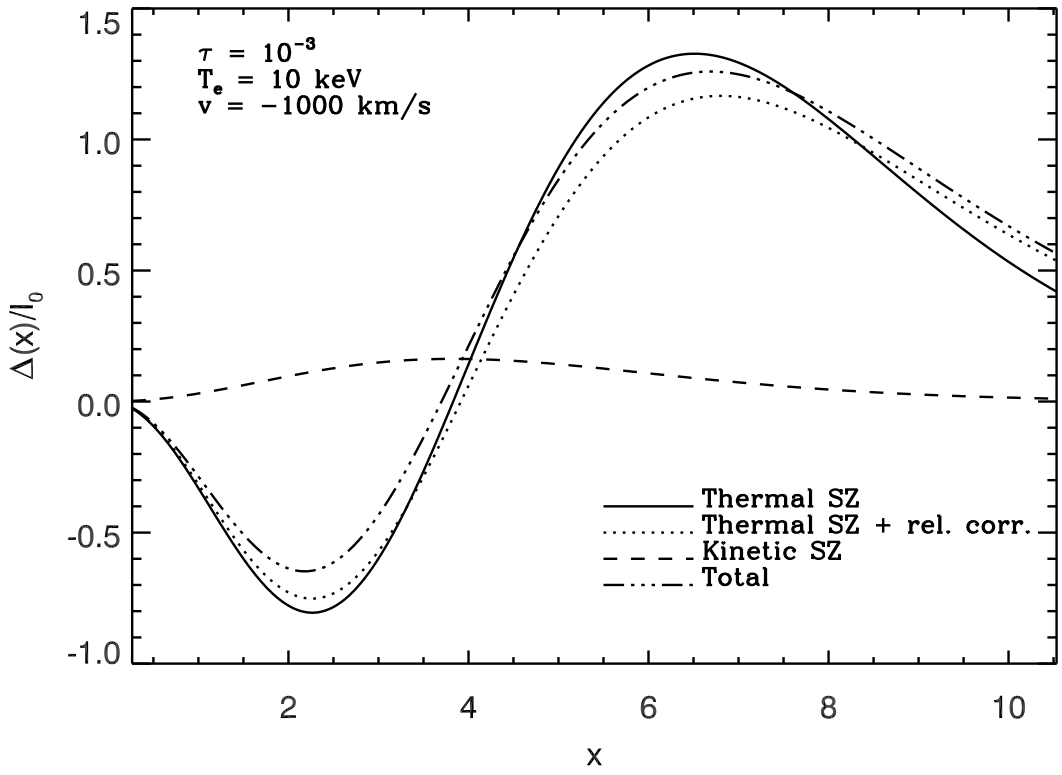

Figure 1.2. The thermal SZ effect is shown as a solid line, the thermal effect including relativistic corrections as a dotted line, the kinetic effect for a cluster velocity equal to -1000 km/s as a dashed line. Finally the sum of all these effects, corresponding to the spectrum which would be observed through the cluster, is marked as *Total*.

temperature independently of X-ray measurements [51], the CMB temperature as a function of redshift [6], [63] and also to search for populations of non-thermal electrons [101].

1.1.2 The kinematic SZ component

The kinematic SZ effect (kSZ) is the Doppler shift of the CMB spectrum, due to the line-of-sight peculiar velocity v_P of the electrons with respect to the CMB rest frame. The change in intensity due to the non-relativistic kinematic SZ effect is:

$$\Delta I_K(x) = -I_0 \frac{x^4 e^x}{(e^x - 1)^2} \int n_e \sigma_T \frac{v_P}{c} \cdot dl \tag{1.5}$$

The spectral shape is the same of the primary CMB anisotropy, and this fact represent a source of confusion to measurements of kSZ effect (see Fig. 1.2).
The thermal and kinematic effects may be separated using their different spectra, indeed the kinematic effect produces its maximum intensity change at the frequency at which the thermal effect is zero [28]. Observations near 217 GHz are sensitive mostly to the kinematic effect, but the temperature-dependence of the shape of the tSZ effect spectrum and the corresponding null frequency position have to be taken

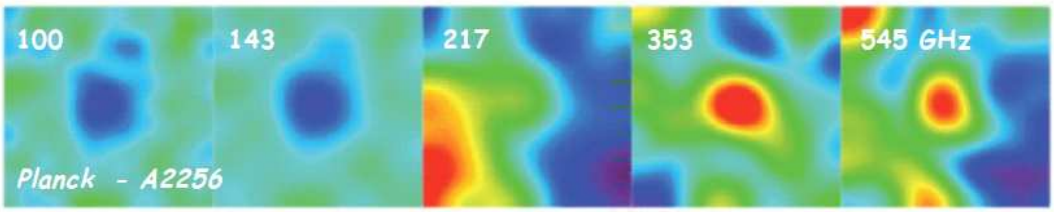

Figure 1.3. Planck observation of the cluster Abell 2256, seen as a dark spot in the CMB at frequencies below 217 GHz (left panels), and as a bright spot at frequencies above 217 GHz (right panels).

carefully in account.
Moreover there are other noise sources which make a measurement of kSZ difficult: instrumental noise, foreground emission (mainly atmospheric emission for ground-based instruments but also galactic synchrotron, bremsstrahlung and IR emission of galactic dust from space), discrete radio source and bulk motions within the cluster (rotation) are the most important. Modeling of noise components with different spectral signature should allow a discrimination, but a multi-band measurement is absolutely essential to this purpose.
To date, the kSZ effect is not have been measured in individual galaxy clusters. Nevertheless, if many galaxy clusters are moving in the same direction, their velocity field creates a dipolar pattern in the CMB radiation at large scale. If a bulk flow is present, the dipole component of the kSZ effect may dominate over the statistical dipole component of the tSZ effect even if for a single cluster.
Using public X-ray data, Kashlinsky *et al.* demonstrated the existence of a statistically significant dipole associated exclusively with clusters [50]. In the absence of alternative explanations they adopted the large-scale bulk flow interpretation but Keisler [52] found that this detection was not statistically significant.
Other studies using similar data sets [80] have found larger uncertainties than those claimed by Kashlinsky *et al.*. Mak *et al.* predicted the Planck satellite performance in determining the bulk flow through kSZ measurements, estimating that the significance of the signal may increase by a factor 5 [64]. Recently a clear statistical evidence of the motions of galaxy clusters through their kSZ signal has been detected in ACT arcminute-resolution microwave maps [43].

1.2 SZ science: current status and future prospects

The first formal description of the effect was presented by Sunyaev and Zel'dovich who describe the interaction of a photon population with a distribution of high energy electrons [106]. Clusters of galaxies, due to the discovery of the strong X-ray emission of the hot intracluster plasma, appeared as ideal laboratories to test the effect in an astrophysical context. Two decades after the effect prediction there where only a few marginal detections from single-dish radio receivers, anyway in the following decade several radio and millimetric SZ observations have been per-

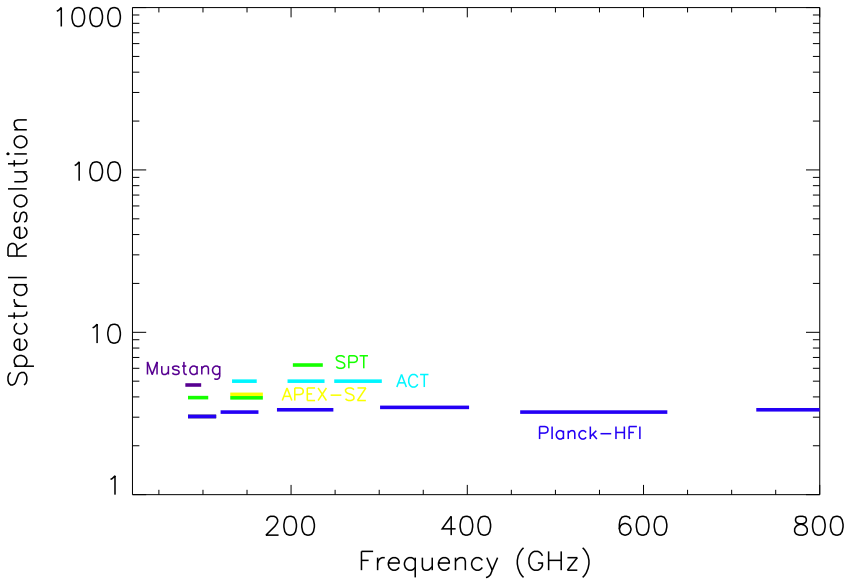

Figure 1.4. Spectral coverage of the main photometric instruments presently operating from ground-based large telescopes (Mustang, SPT, ACT, APEX-SZ) and from space (Planck-HFI). The y-axis upper limit is intentionally overestimated in order to highlight the lack of high spectral resolution instruments (to be compared with Fig.1.5) (credits M. De Petris).

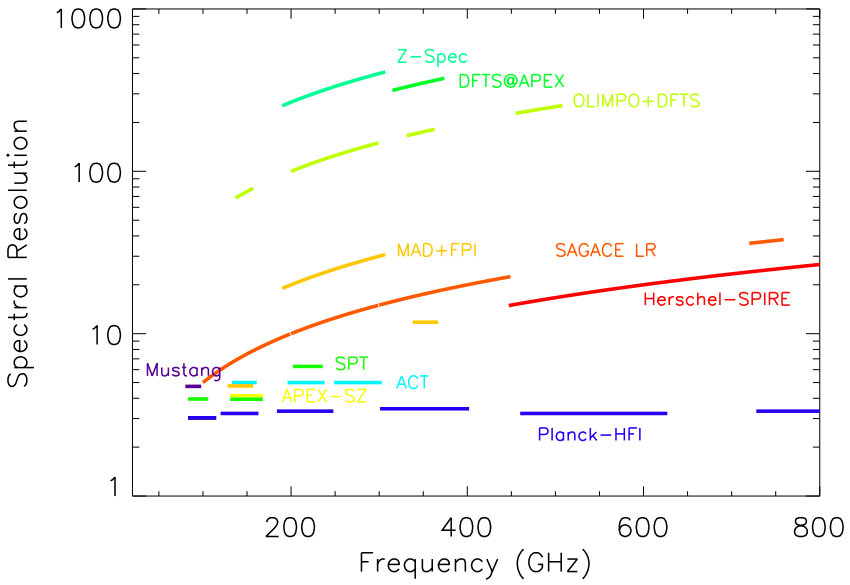

Figure 1.5. Spectral coverage of the present (Z-Spec) and future spectrometers that will operate from ground-based large telescopes (DFTS@APEX, MAD+FPI), balloon (OLIMPO+DFTS) and satellite (SAGAGE) (credits M. De Petris).

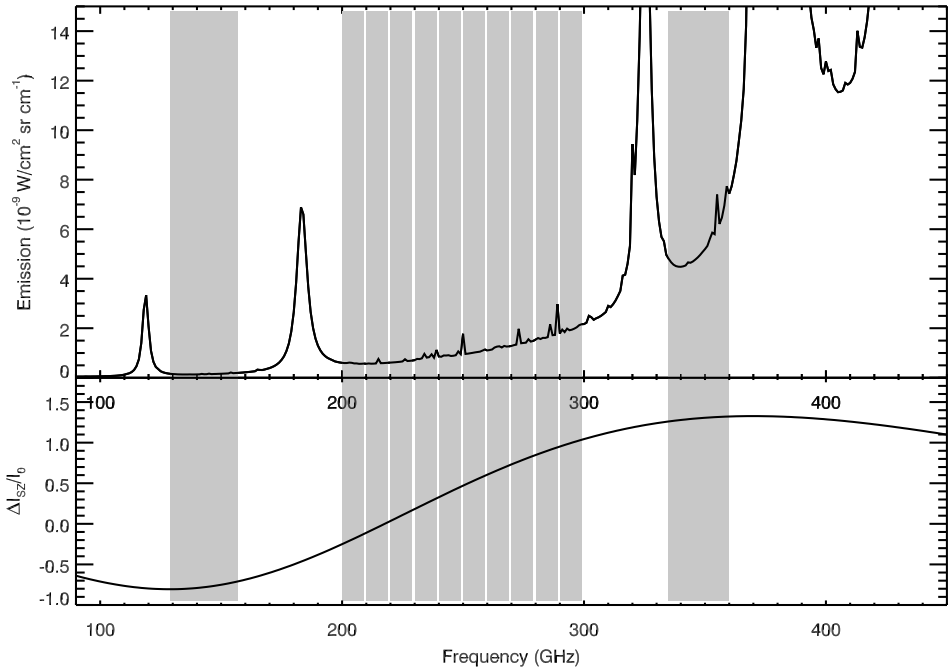

Figure 1.6. The bands of MAD experiment match the atmospheric windows as well the spectral signature of the SZ effect.

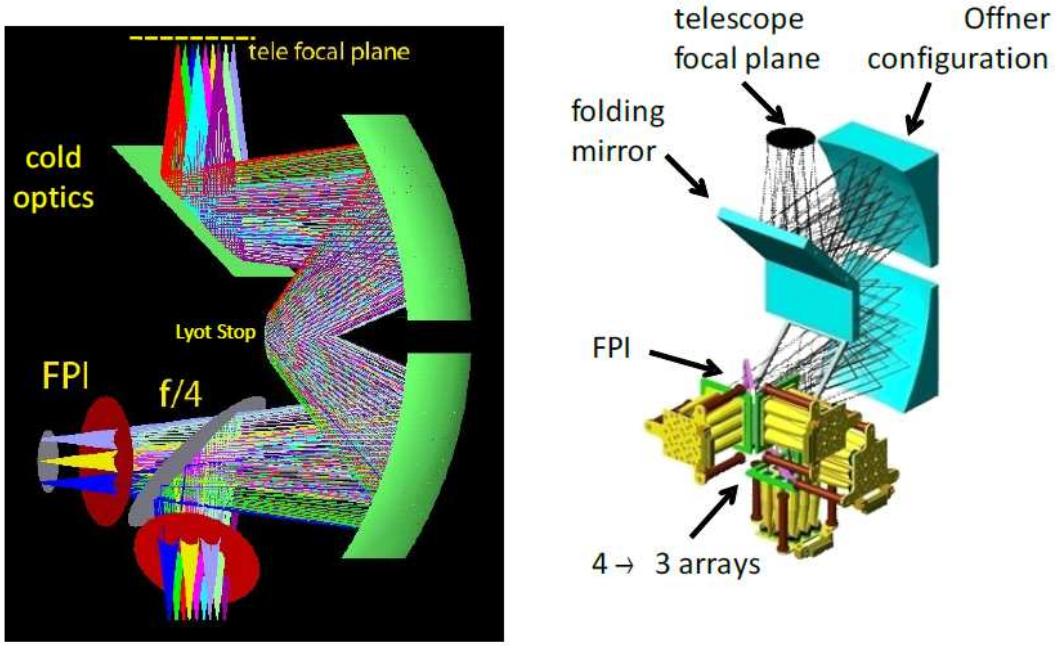

Figure 1.7. ZEMAX layout (left panel) and CAD (right panel) of MAD cold optics (credits L. Lamagna). The position of the FPI is pointed out.

Table 1.1. Instrumental features of the main photometric cameras operating from ground-based telescopes.

	Spectral Bands	beam FWHM	Telescope	Ref.
Mustang	90 GHz	8 arcsec	GBT (100 m)	[33]
Bolocam	140, 270 GHz	58 arcsec (140 GHz)	CSO (10.4 m)	[39]
APEX-SZ	150 , 220 GHz	1 arcmin (150 GHz)	APEX (12 m)	[34]
NIKA	150 , 220 GHz	16.7 and 12.4 arcsec	IRAM (30 m)	[76]
SPT	95, 150, 220 GHz	1.1 arcmin (150 GHz)	SPT (10 m)	[17]
ACT	148, 218, 277 GHz	1.4, 1.0 and 0.9 arcmin	ACT (6 m)	[108]
LABOCA	350 GHz	19 arcsec	APEX (12 m)	[103]

formed on individual clusters with bolometers and radio interferometers [47], [55] [28], [16]. A whole generation of projects devoted to demonstrate the feasibility of such measurements and the astrophysical and cosmological potential of SZ surveys by dedicated instruments has been developed. Many bolometer-based photometric cameras are presently operating from large telescopes with angular resolution comparable to or better than 1 arcminute, matching the typical angular scales of galaxy clusters. A partial list is presented in Table 1.1.

In particular ACT and SPT have recently allowed the detections of many tens of previously undiscovered clusters even at redshift above unity [45], [65], [102], [70], [120], [92], [12], [36], [105]. Moreover in the last few years the space-based instrument Planck-HFI (100, 143, 217, 353, 545 and 857 GHz with angular resolution of about 30 arcmin at the lowest frequencies) [89] has been observing hundreds of galaxy clusters combining full sky coverage and wide spectral range at the price of a more limited angular resolution. Herschel-SPIRE (250, 360 and 520 μm, combined to a FTS covering the 200-670 μm range) [41] has also been used to observe the short wavelength tail of the SZ effect on a few galaxy clusters [129]. The spectral coverage of the photometric instruments listed previously is highlighted in Fig. 1.4. The next generation of instruments, like the CCAT telescope[1], will routinely achieve the sensitivity of the deepest targeted observations of present-day SZ measurements, with the added feature of a better than 75 arcseconds beam FWHM over the whole band of interest for the SZ effect [77]. This will allow to systematically observe the substructure of hot gas in galaxy clusters at redshifts well above unity, investigating the details of formation and evolution of thousands of clusters through integrated pressure maps of the ICM.

In order to be able to fully exploit the potential of SZ surveys for cosmology, a lot of effort is being put into the understanding of the complex baryon physics that determines the breaking of self-similarity in the clusters population. Many recent results, based both on numerical simulations and observations, have recently pointed out that a substantial fraction of clusters deviates from dynamical equilibrium and that many morphologically disturbed clusters cannot be simply modeled through the assumption of spherical symmetry and local thermal equilibrium. ICM in such objects exhibits strong features due to merging events, AGN feedback, cold fronts

[1] http:/www.submm.org

and other nonthermal processes. Moreover the community is currently debating the possibility that the fraction of unrelaxed clusters will be evolving with redshift, increasing while approaching the formation epoch. The deepest surveys of next generation will then have to be able to resolve these features both spectrally (through the impact of nonthermal electron populations on the shape of the tSZ signature) and spatially (through accurate mapping) at high redshift. Early examples of this new approach are, for instance, Z-Spec, OLIMPO+DFTS, SAGACE, MAD+FPI and DTFS@APEX [130], [67], [25], [54] (see Fig. 1.5). From this scenario two conclusions may be drawn:

- Detailed informations about ICM may be inferred by high resolution observations of SZ effect, rendering practically unfeasible this kind of measurements from platforms other than large ground-based telescopes. Therefore future SZ instruments will require a careful characterization of atmospheric performance at their site of operation. This topic will be introduced in Sec. 1.4 and fully explored in Chapters 2 and 3.

- Many current and upcoming SZ observations rely on photometric information over a limited number of bands. This is due to several reasons, mainly connected to the presence of the atmosphere, that allows to perform observations only in some well-defined spectral windows. A new observational strategy, based on an imaging spectrometer operating in the mm spectral region, will be presented in the next section.

1.3 Observational strategy

As remarked in the previous sections SZ spectrum is continuous, without peculiar high resolution spectral features. A spectral sampling combined to a wide spectral coverage in proximity of the crossover frequency could allow the disentangle of the degeneracies among cluster parameters and foregrounds.
To this purpose three mm-spectrometer configurations have been taken in consideration: Diffraction Grating (DG), Fourier Transform Spectrometer (FTS) and Fabry-Perot Interferometer (FPI). The first solution is characterized by the absence of movable parts and this make it well suitable for cryogenic systems. Anyway it needs large size even for moderate spectral resolution, with the possibility to perform imaging only in one spatial dimension because one focal plane dimension is required for spectral information.
On the other hand FPI can obtain a two-dimensional image at each spacing of the FPI etalon, yielding a data-cube (2D spatial and 1D spectral). Therefore, it can be significantly faster than a grating for mapping extended objects. Note that FPI must stop to integrate individual bands at several different plate separations, while gratings obtain an instantaneous spectrum by integrating just once at a given grating position.
Even the FTS solution is well suitable for 2-dimensional imaging, mainly due to the multiplex (Felget) advantage in performing the spectral sampling measuring simultaneously all the spectral elements over the range of frequencies. Anyway this advantage may turn out to be a limiting factor because the averaged total

Table 1.2. The main features of Diffraction Grating (DG), Fourier Transform Spectrometer (FTS) and Fabry-Perot Interferometer (FPI) mm-spectrometers configurations.

	FPI	FTS	DG
Multiplex advantage	No	Yes	No
Throughput	High	High	Low
Movable parts	Yes	Yes	No
Size to spectral resolution ratio	Low	High	High
Background photon noise	Low	High	Low
2-D imaging capability	Yes	Yes	No

power falling onto the detectors may create an unacceptable photon noise level in the presence of high emission foregrounds, especially due to the atmosphere. The most important advantage for our interest is that in a differential configuration, a FTS can extract very small signals from a common background, as shown in the SAGACE (Spectroscopic Active Galaxies And Clusters Explorer) design [25]. In Table 1.2 the main features of the three solutions are summarized. The choice of the optical system is driven by efficiency, resolution and technical constraints. Among the three observational approaches described above I have explored the FPI solution, mainly for its simplicity and compactness. It would improve the capabilities of MAD (Multi Array of Detectors), a 4-channel photometer optimized for multi-frequency observation of SZ effect [54] that will operate at Millimetre and Infrared Testagrigia Observatory (MITO), a 2.6-m in diameter telescope located in the Alps in Val d'Aosta (3480 m a.s.l.) [32]. MITO station is famous for the good atmospheric conditions and low water vapour content (less than 1 mm during Winter months), ensuring ideal observing conditions for millimeter experiments.

MAD is a 3 x 3 pixel photometer with 4.5 arcmin/pixel angular resolution. The cold optics is based on a revised version of an Offner configuration to reduce instrumental spurious emission. The image of the subreflector is formed on the Lyot Stop cooled down to 4.2 K (see Fig. 1.7). A double stage ^{3}He - ^{4}He fridge is able to maintain the detectors for 80 h at 300 mK.

MAD is designed to operate in the bands 140, 220, 270 and 350 GHz, chosen to match the best atmospheric transparency spectral windows and, at the same time, to explore the SZ effect spectral signature (see Fig. 1.6). The highest frequency channel has been implemented to monitor the foreground contribution of galactic dust emission, which becomes more significant with increasing frequencies and decreasing galactic latitudes.

A FPI can be adopted to improve MAD potential, adding an hybrid solution with spectroscopic capabilities too: 3 photometric bands (140, 270 and 350 GHz, with 20 per cent and 10 per cent of bandwidth respectively) combined with a FPI operating in correspondence to the 220 GHz channel. The interferometer could be easily placed before the bolometer array, in a f/4 converging beam configuration, as shown in Fig. 1.8. This optical configuration limits the spectral resolution. In fact, if the incident beam is tipped relative to the etalon normal, a FPI resonates at a shorter wavelength and the spectral profile is both shifted and broadened. On the other hand SZ spectrum is continuous and an high resolution spectral sampling is

not required.
The total bandwidth of the spectrometer is close to 100 GHz (see the central band in Fig. 1.6). An etalon with a power resolution of 10 needs only to be less then one centimeter thick, providing a substantial benefit in a cryogenic environment. Moreover FPI systems are also fully tunable and the resolving power is continuously variable by a change in the cavity spacing. The theory and the practical limitations of the FPI will be discussed in Chapter 4. From the instrumentation standpoint, the two reflective elements of the FPI can be made of two metallic meshes face to face, one fixed and one moving (see Chapter 5 for more details). Spectroscopy with a FPI lends itself naturally to a spatial imaging system, allowing multiple detectors to be configured in a two-dimensional array on the sky. Furthermore, off-source pixels can be used to subtract much of the sky noise that is due to fluctuating atmospheric emission characterizing ground-based millimeter observations. The FPI, reducing the instantaneous bandwidth, limits the photon background on the detectors and the photon noise.
By means of the Poisson statistic one can evaluate the amplitude of power (W) fluctuations due to photon noise, as a function of the photon energy emitted by a black-body at temperature T:

$$\sqrt{\langle \Delta W^2 \rangle \, df} = \sqrt{\frac{4k_B^5}{h^3c^2}} \sqrt{A\Omega} \sqrt{T^5 \int_{x_1}^{x_2} \frac{x^4 e^x}{(e^x-1)^2} dx df} \tag{1.6}$$

where $x = \frac{h\nu}{k_B T}$ is the a-dimensional frequency, while $A\Omega$ is the system throughput (0.042 cm^{2}sr for a single pixel of MAD). If the photons are emitted by a gray-body with emissivity ϵ the previous expression becomes:

$$\sqrt{\langle \Delta W^2 \rangle \, df} = \sqrt{\frac{4k_B^5}{h^3c^2}} \sqrt{A\Omega} \sqrt{T^5 \int_{x_1}^{x_2} \frac{x^4 e^x - 1 + \epsilon}{(e^x-1)^2} dx df} \tag{1.7}$$

In Fig. 1.9 the density photon noise of the radiation emitted by the atmosphere, by the telescope mirrors and by the CMB are shown. The atmospheric brightness temperature has been evaluated by means of ATM model (see Sec. 1.4) for $pwv = 0.1$ mm. Both the mirrors are assumed as room temperature gray-bodies with $\epsilon = 1$ per cent. The atmospheric contribution turns out to be two order of magnitude larger then CMB and mirrors.
The photon noise associated to the radiation emitted by the atmosphere has been evaluated both for FPI and for FTS. The integral in Eq. 1.6 has been performed changing the integration extremes in the two cases: while the FPI has ten values, corresponding to the ten spectral elements highlighted in Fig. 1.6, FTS photon noise has one value, corresponding to the whole spectral range (200-300 GHz). The result is shown in Fig. 1.10, where the atmospheric emission has been evaluated for 1 mm and 0.1 mm of *pwv*.
Background total power of the atmospheric emission corresponding to FPI and FTS configurations is plotted in Fig. 1.11. Figs. 1.10 and 1.11 show that for ground-based observations the FTS solution is not the best choice in terms of background radiation and photon noise on the detectors. In Table 1.3 the instrumental performance of the system MAD+FP with 10 spectral elements in the 200-300 GHz are summarized.

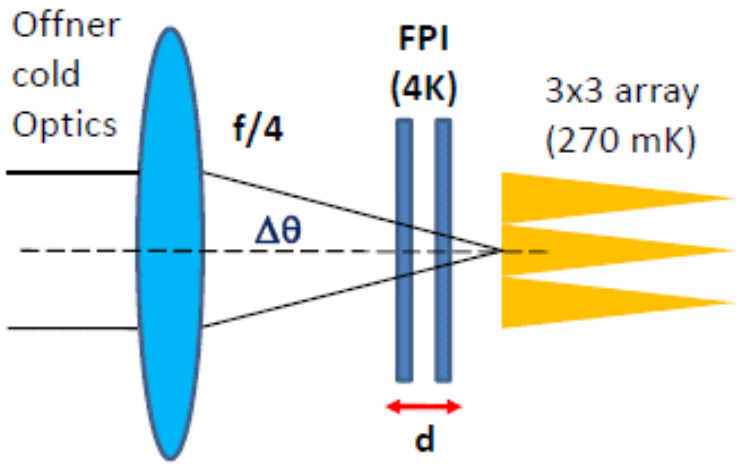

Figure 1.8. FPI placed before the bolometer array, in a f/4 converging beam configuration.

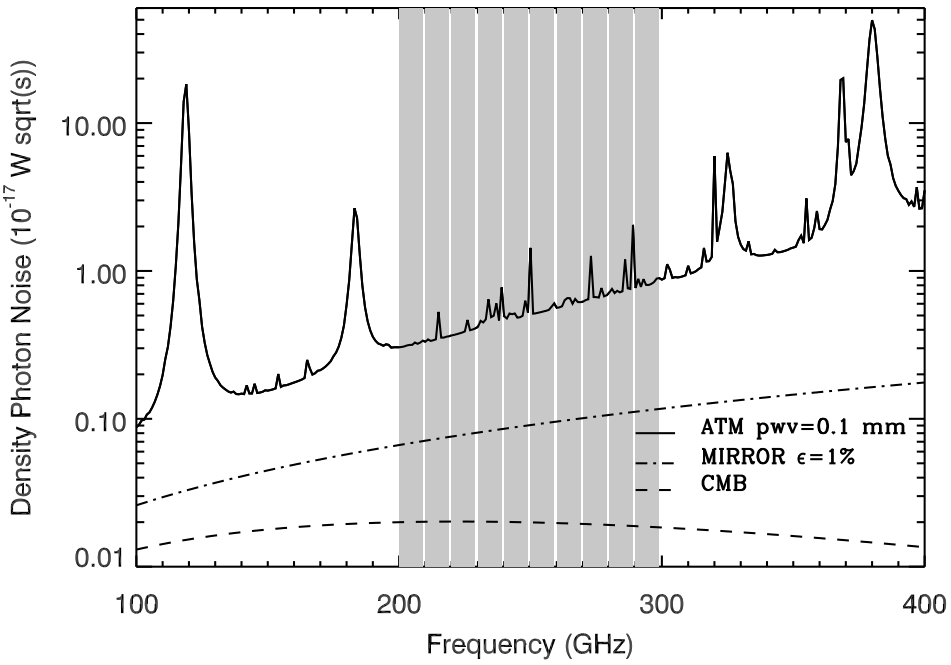

Figure 1.9. Density photon noise of the radiation emitted by the atmosphere, the CMB and the telescope mirror, assumed to be a gray body at room temperature.

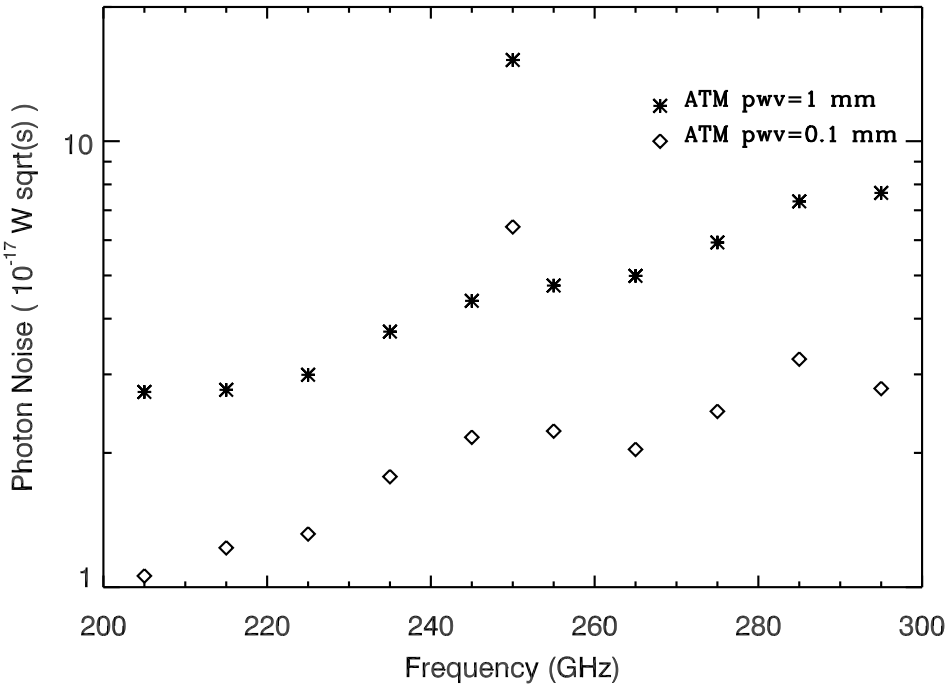

Figure 1.10. Atmospheric photon noise on the detectors evaluated for two values of *pwv* (in the legend) concerning FPI in the ten spectral elements and FTS in the whole 200-300 GHz band.

Table 1.3. MAD + FP instrument performances evaluated considering emission from CMB, mirror (300 K with 1 per cent emissivity) and atmosphere (0.2 mm *pwv*).

MAD + FP	Band1	Band2	Band3
Frequency (GHz)	143	200-300	345
Bandwith (GHz)	30	10	30
FWHM (arcmin)	4.5	4.5	4.5
FoV (arcmin)	15 x 15	15 x 15	15 x 15
number of detectors	9	9	9
Photon bckg overband	5.3	3.7	84.4
Photon noise overband (10^{-17} $W_{rms}\sqrt{s}$)	4.1	4.0	28.9

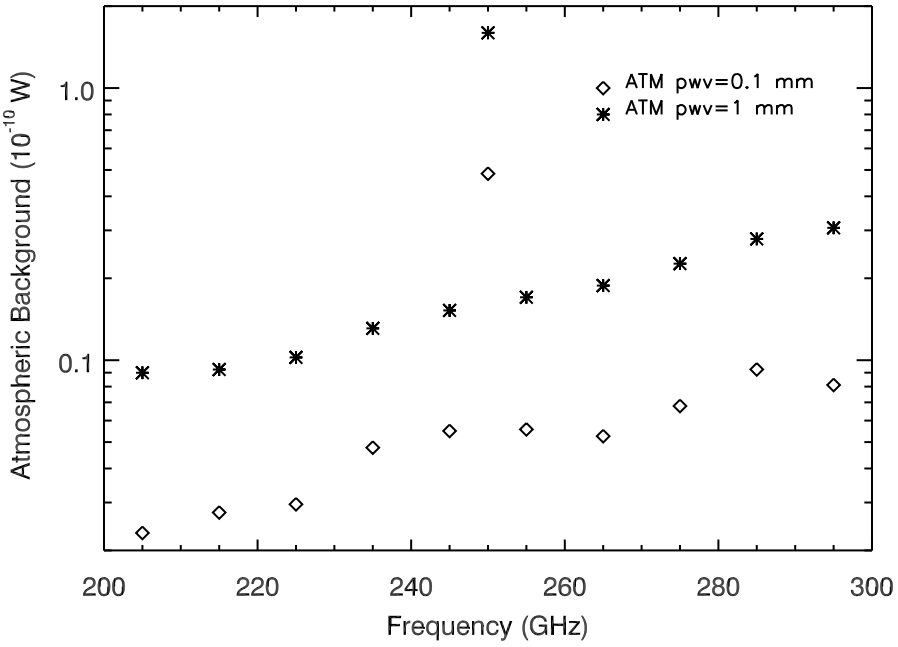

Figure 1.11. Atmospheric background on the detectors evaluated for two values of *pwv* (in the legend) concerning the FPI in the ten spectral elements and FTS in the whole 200-300 GHz band.

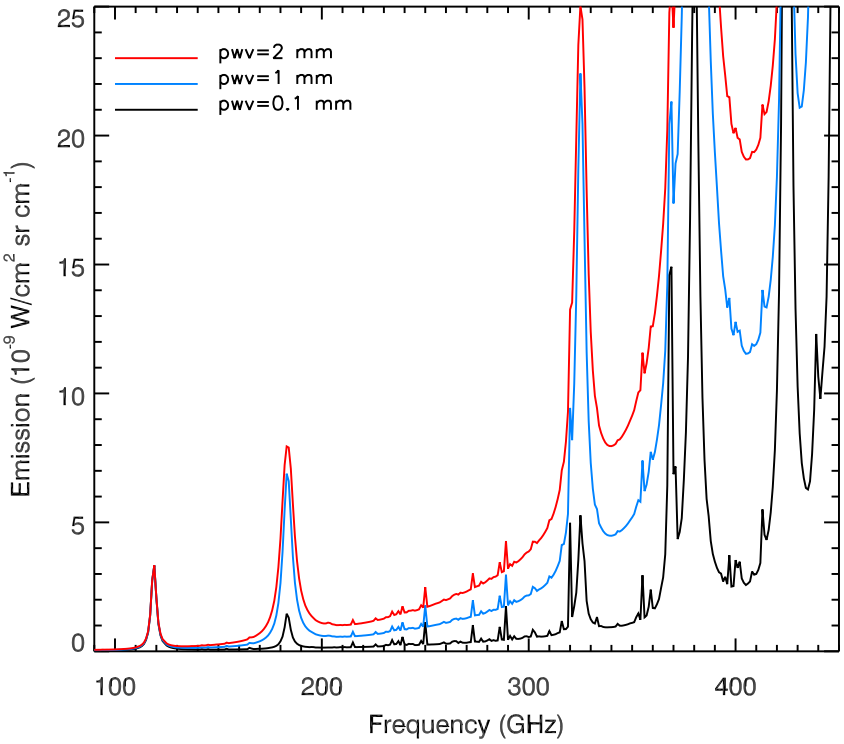

Figure 1.12. MITO atmospheric emission spectra as modeled by ATM, corresponding to three values of *pwv*.

1.4 Atmospheric monitoring

The last few years have witnessed increasing efforts in the design and construction of large telescopes in places of the planet which provide the potentially most attractive atmospheric features for mm and sub-mm astronomy. At a time where bolometric detectors can easily approach the photon noise limit, and large cameras with hundreds or thousands of such detectors already allow to break this limitation, it is straightforward to realize that an improper characterization of the atmospheric properties may become the strongest restriction to the effective science return from ground-based instruments of the next generation.
The atmospheric spectrum in the mm/sub-mm region is mainly dominated by the precipitable water vapor (*pwv*) modeled by a continuum-like term and by a series of absorption lines peaked at 183, 325, 380, 448, 557 GHz (see Fig. 1.12). Oxygen is also present as absorber at 118, 368 and 425 GHz but, differently from H_2O fluctuations, it is well-mixed in the atmosphere and so it mainly contributes only as a constant radiation background, still dependent on the elevation, with consequent photon noise on the detectors.
A commonly used approach for atmosphere monitoring consists in dealing with atmosphere by an isothermal slab model where opacity follows a zenithal secant-law. Under this assumption large telescopes periodically perform altitude scans in the sky, *i.e.* skydips, to derive the zenith optical depth, integrated in the operating photometric band.
Due to the fact that this procedure subtracts time to the astronomical observations, the opacity is alternatively derived by employing ancillary instruments like tippers, GPS or water vapor radiometers (see for instance [91], [23] and [126]). All these usually feature wide fields of view and limited spectral capabilities, unmatched to those of scientific instruments. Although they allow a continuous data recording by simple instruments, their single frequency observations needs a synthetic atmospheric model to infer transmission at other frequencies.
There are several simulation codes able to provide synthetic atmospheric spectra, starting from the knowledge of climatic and geographic properties of the site of interest. Among them ATM (Atmospheric Transmission at Microwaves) is one of the best known [83]. Assuming the thermodynamic local equilibrium hypothesis, ATM evaluates the black body temperature approximating atmospheric transmission at each frequency. Once the altitude, the profiles of pressure and temperature and *pwv* have been fixed, the code determines the corresponding atmospheric spectrum from 0 to 2 THz, considering the H_2O contribution until 10 THz. The validation of the model for a specific site is mandatory and this is possible only when on-site recorded spectra are available.
I will describe a semi-empirical approach to perform an analysis of atmospheric transmission and emission at the italian-french station in Antarctica (Dome C), one of the best sites in the world to perform observations in a wide spectral range. A wide frequency coverage transmission measurements campaign at Dome C, employing the direct spectroscopic information derived by an interferometric experiment, was never carried out. Radiosoundings data provided by the Routine Meteorological Observations (RMO) Research Project at Concordia station have been corrected by temperature and humidity errors and dry biases and then employed to feed ATM

code to generate synthetic spectra in the wide spectral range from 100 GHz to 2 THz (see Sec. 2.1) [26].
Anyway only direct and frequent measurements of atmospheric transmission in a wide spectral range can provide a perfect knowledge of atmospheric influence on astronomical observations. To this purpose an atmospheric emission spectrometer has been developed: CASPER2, the MITO version of CASPER (Concordia Atmospheric SPectroscopy of Emitted Radiation), the spectrometer for absolute measurements of low resolution atmospheric emission spectra in the FIR/mm range proposed in 2003 to PNRA for Dome C [29]. The instrument is devoted to recording real time atmospheric spectra along MITO telescope pointing direction.
Such an instrument allows to avoid specific telescope procedures, with consequent loss of observational time and to infer atmosphere opacity in a wide spectral range. Full details of the instrument characterization will be provided in Sec. 3.1.
Preliminary measurements of atmospheric spectra performed during the summer campaign at MITO from 11 July to 19 July 2010 will be presented and discussed in Sec. 3.6.

Chapter 2

Atmospheric effects on mm and sub-mm observations

The reliability of astronomical observations at millimeter and sub-millimeter wavelengths closely depends on a low vertical content of water vapor as well as on high atmospheric emission stability. Short term variation of the atmospheric emission on different spatial scales contributes as sky noise while slow fluctuations of the attenuation can affect the quality of sky calibrations.
For this reason mm and sub-mm astronomical observations can be made only at the driest and most stable sites, like the desert mountain summits. Among the locations chosen for large telescopes, there are Mauna Kea in Hawaii (4100 m a.s.l.), the high Andes in northern Chile (5000 m a.s.l.), and the Antarctic plateau (3000 m a.s.l.).
It is important to remark that the high quality of ground-based cosmological and astrophysical observations can be reached only by a continuous monitoring of atmospheric performance. A spectrometer is the natural solution for sky monitoring over a wide spectral band and furthermore if the spectrometer is optically matched to an its own medium size telescope it is possible to observe the sky towards a specific direction and at an angular scale closer to that of the main telescope. Spectrometers designed only with this goal are, for instance, the FTS interferometer employed at Pampa la Bola, 4800 m above sea level in northern Chile [68], [69] or the one employed both in Mauna Kea (Hawaii) and near Cerro Chajnantor (northern Chile) [81].
CASPER (Concordia Atmospheric SPectroscopy of Emitted Radiation) is the atmospheric spectrometer proposed to the P.N.R.A. (Programma Nazionale Ricerche in Antartide) devoted to the correction by atmospheric absorption of the astrophysical measurements realized by the Concordia Italian-French station at Dome C, on the Antarctic plateau [29].
Dome C is considered one of the best sites in the world to perform observations in a wide range of the electromagnetic spectrum allowing also to explore Terahertz windows [75], [115]. Anyway a wide frequency coverage transmission measurements campaign at Dome C, employing the direct spectroscopic information derived by an interferometric experiment, was never carried out. CASPER will be able to provide atmospheric spectra from 90 to 1650 GHz with 1 per cent of accuracy and

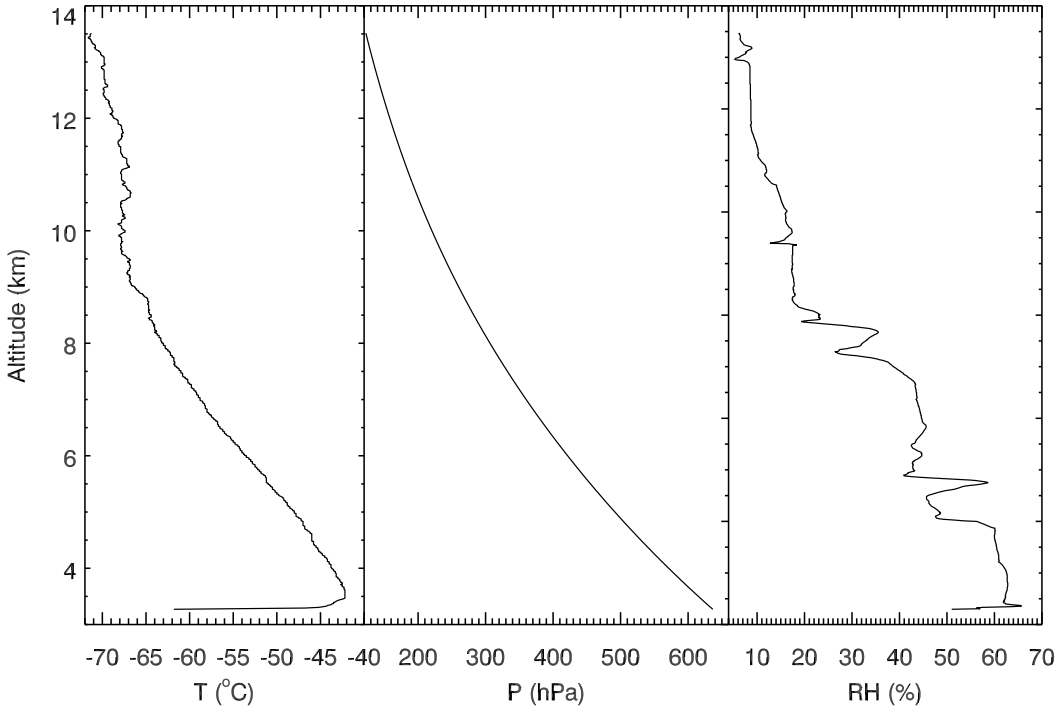

Figure 2.1. Vertical profiles of air temperature, pressure and relative humidity obtained from the June 22nd 2006 radiosounding data.

1 degree of angular scale. In order to compensate for the lack of a continuous and spectrally wide atmospheric monitoring at Dome C, the performance in the mm/sub-mm bands have been predicted by means of the semi-empirical approach described in the next Sections.

2.1 Dome C synthetic spectra production

At present, for the site of Dome C we can rely only on the atmospheric monitoring performed at a few individual frequencies, with no simultaneous measurements in different regions of the spectrum. In order to compensate for the lack of a continuous and spectrally wide atmospheric monitoring at Dome C, the performance in the mm/sub-mm bands in the period from May 2005 to January 2007 has been predicted by means of a semi-empirical approach.
A set of raw radiosounding data was recorded for the present study, consisting of an overall number of 469 radiosounding measurements taken routinely at Dome C, at 12:00 UTC from May 2, 2005 to January 31, 2007 ranging from a minimum of 15 in May 2005 to a maximum of 30 in November 2006.
As example the radiosounding data profiles recorded on June 22nd 2006 are shown in Fig. 2.1). In general, each radiosonde measurement consists of values of air pressure P, air temperature T and relative humidity RH, taken at more than 800 standard and additional levels in the altitude range from surface to 10 km above mean sea level (amsl). The time-patterns of the daily *pwv* values are shown in Fig. 2.2. Two main features are evident in Fig. 2.2, showing that the majority of *pwv*

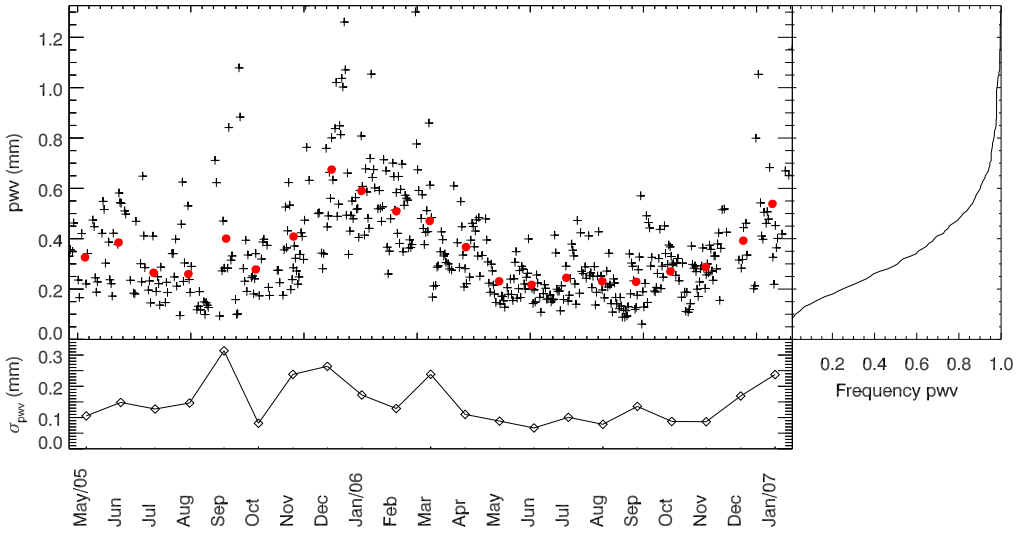

Figure 2.2. Daily values of precipitable water vapor (*pwv*) estimated from the 12:00 UTC radiosounding measurements performed at Dome C over the period from May 2005 to January 2007 are shown in the upper left panel. Monthly averages of *pwv* are overplotted as red dots. In the right panel the corresponding *pwv* vs. cumulative frequency is plotted. The bottom panel shows the monthly *pwv* fluctuations quantified as the daily values standard deviation, σ_{pwv}.

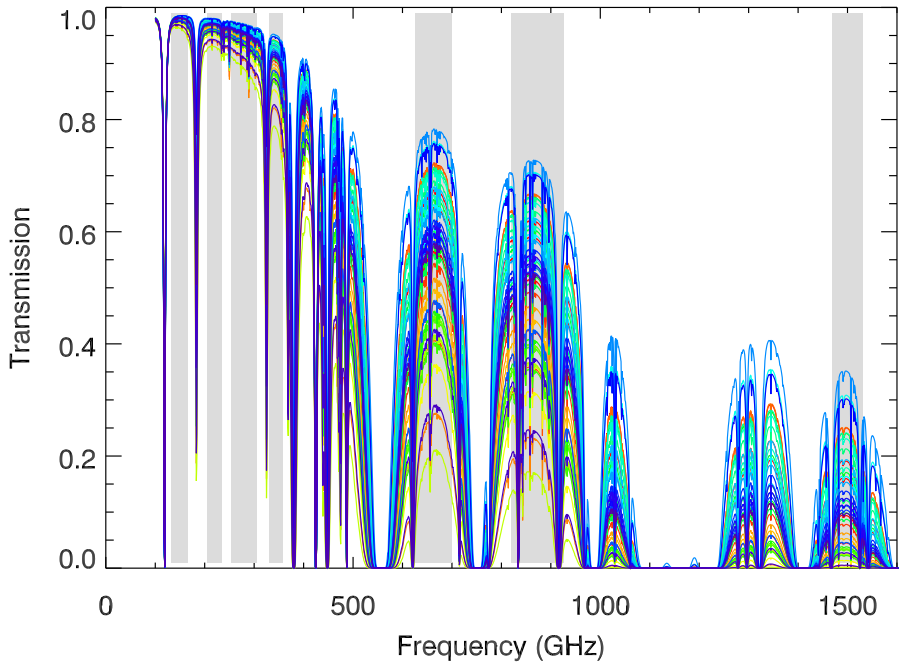

Figure 2.3. Atmospheric transmission spectra as modeled by ATM program for each radiosounding. Photometric bands in Table 2.1 (gray) match the main transmission windows.

Table 2.1. Characteristic spectral bands assumed in this work.

	ν_0 (GHz)	λ_0 (μm)	FWHM(%)	References
LF	150	2000	22	1, 2, 3, 4
	220	1400	13	1, 2, 3
	270	1100	18	1, 2, 3
	350	860	8	1, 2, 5, 6
HF	660	450	11	5, 6
	870	350	13	5
	1500	200	5	7

References: (1) SPT, [96]; (2) MITO, [28]; (3) ACT, [108]; (4) BRAIN, [7]; (5) SCUBA, [46]; (6) SCUBA-2, [31]; (7) THUMPER, [124];

values are lower than 0.3 mm during the austral autumn months, although presenting largely dispersed patterns (of 50 per cent or more), and, hence, low stability.
As shown by [111], a limited contribution is given to the overall value of atmospheric *pwv* by the amount of water vapor present in the Upper Troposphere and Low Stratosphere (UTLS) region from 8 to 12 km amsl, while negligible fractions of *pwv* ranging mainly between 0.003 and 0.005 mm throughout the year are present in the stratosphere from 12 to 50 km above Dome C [112].
Synthetic spectra in emission and in opacity have been estimated by means of the ATM code in the wide spectral range from 100 GHz to 2 THz. The transmission corresponding to each radiosounding dataset, estimated from optical depth spectra as $T = e^{-\tau}$, is shown in Fig. 2.3.
In the period under consideration, the inferred *pwv* values show an average close to 0.3 mm with a mean dispersion of about 150 μm (see Fig. 2.2). The same amount of *pwv* variation can contribute with a different weight to the total optical depth. As example in Fig. 2.4 we represent the optical depth fluctuations derived by ATM, quantified as the maximum dispersion, due to fluctuations of *pwv* of the order of 150 μm around three different *pwv* values (0.15, 0.5 and 1.0 mm). It is worthy of note that for low *pwv* content, $\Delta\tau$ can be as high as 60 per cent in the high frequency windows.
In Sec. 2.2 estimates of atmospheric transmission and emission corresponding to largely explored ground based telescope bands between 150 and 1500 GHz are analyzed. A parameter to rank the observational conditions for each of the selected spectral bands is introduced as the ratio between average transmission and the corresponding fluctuations (see Sec. 2.4). The effect of the filter bandwidths on the estimate of opacity has been included in the τ-*pwv* relation, showing a contribution up to a 30 per cent over-estimate on the opacity in the case of the highest frequency band (see Sec. 2.5). Because data provided by the radiosonde sensors are affected by lag and instrumental errors as well as by various dry biases, they were all corrected following the procedure described in Sec. 2.6.

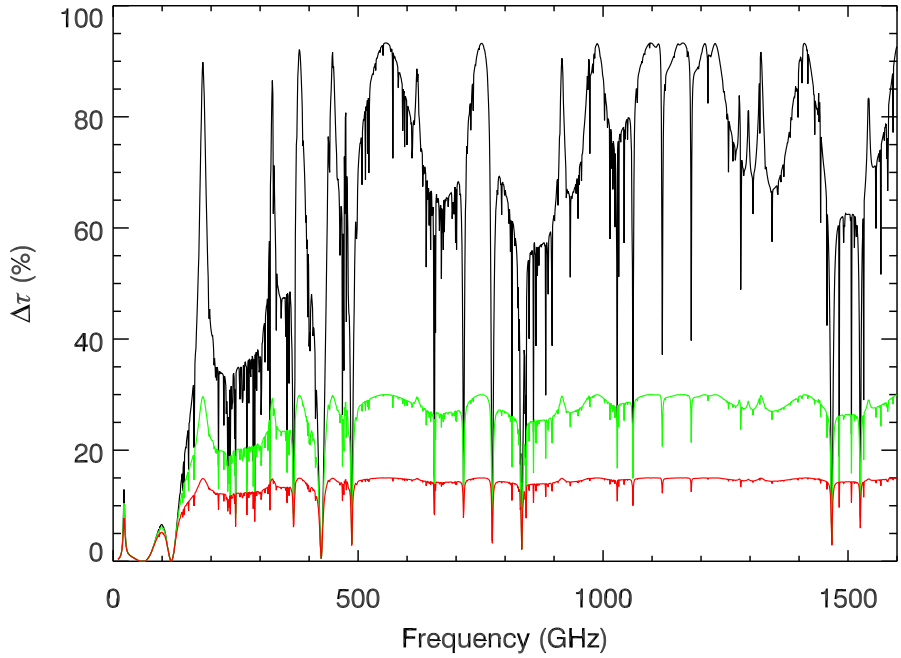

Figure 2.4. Optical depth fluctuations corresponding to a 150 μm variation around three selected *pwv* values: 1 mm (red line), 500 μm (green line), 150 μm (black line).

2.2 Multi-band analysis

A quantitative analysis has been performed considering 7 photometric bands centered at the frequencies of several astrophysical and cosmological experiments: South Pole Telescope (SPT), Atacama Cosmology Telescope (ACT), Millimetre and Infrared Testagrigia Observatory (MITO) and BRAIN (B-mode RAdiation INterferometer) for Low Frequency (LF) atmospheric windows; Submillimetre Common-User Bolometer Array (SCUBA and SCUBA-2) and Two HUndred Micron PhotometER (THUMPER) for sub-mm bands (High Frequency, HF). The central frequency of each band, as well as the bandwidth, quantified with the FWHM (Full Width Half Maximum), are listed in Table 2.1 (see also Fig. 2.3). The band profiles are assumed to be top-hat assuming in this way the maximum rejection to off-band contributions.

To assess the constraints on astronomical observations arising from the atmosphere emission above Dome C, an estimate of the NEP (Noise Equivalent Power) and the $NEFD$ (Noise Equivalent Flux Density) for all the seven bands is provided. In fact in such a wide spectral region both the quantities are normally employed: the power density, mainly for the low frequency bands, while the flux density, for the high frequency region. The quoted NEP is the root of the sum of NEP^2_{atm}, the term considering the atmospheric emission fluctuations, and NEP^2_{tele}, i.e. the instrumental contribution to the photon noise. The atmospheric emissivity spectra have been generated by ATM. The telescope is assumed a 10-m in diameter Al-mirror with a surface emissivity of the order 3 per cent at 150 GHz and depending on the frequency as $\sqrt{\nu}$. The throughput of the telescope is assumed diffraction

Table 2.2. Transmission quartiles matching cumulative distributions in Fig. 2.6.

	ν_0 (GHz)	λ_0 (μm)	25%	50%	75%
LF	150	2000	0.97	0.97	0.96
	220	1400	0.95	0.94	0.94
	270	1100	0.94	0.93	0.92
	350	860	0.91	0.89	0.87
HF	660	450	0.64	0.56	0.46
	870	350	0.58	0.50	0.40
	1500	200	0.15	0.08	0.03

Table 2.3. Pwv quartiles comparison.

Period	25%	50%	75%	References
01/1997	0.38	0.52	0.68	1
05/2005-01/2007	0.20	0.30	0.45	2
2008	0.15	0.24	...	3
2008-2010	0.21	0.27	0.35	4
12/2009-01/2010	0.49	0.75	1.1	5

References: (1) [119]; (2) our results; (3) [127]; (4) [115]; (5) [7].

limited at each band. Focal plane optical efficiencies are taken as unitary for all the bands as well as telescope main beam efficiency. The dominant sky sources (CMB and dust) are not included, the instrument detector noise is assumed lower than the background noise and the spillover emission is neglected. In order to quantify the maximum variation of these quantities NEP and $NEFD$ values for all the bands are shown in Fig. 2.5, for the extreme conditions occurred during the austral summers and winters at Dome C in the 2005-2007 period.

2.3 Dome C statistics comparison

To validate the proposed semi-empirical approach, the derived atmospheric performance are compared with the results available in literature.
Fig. 2.6 shows Dome C atmospheric transmission as a function of the cumulative time frequency derived by radiosounding data and ATM model for the bands listed in Table 2.1 (the corresponding quartiles are reported in Table 2.2). Transmission statistics at Dome C performed by [119], [75], [127], [115] and [7] are compared with our analysis.
Low frequency atmospheric windows show high transparency during the whole period confirming that high quality mm observations can be performed from this site for most of the time. For instance the 150 GHz 50 per cent quartile transmission is about 97 per cent (see the green line in Fig. 2.6). This is consistent with the 95 per cent value recently measured by [7] during the summer campaign in December 2009/January 2010, even considering their integrated in-band result.
Median transparency for the 220 GHz atmospheric window is about 95 per cent (see the cyan line in Fig. 2.6) as already derived by [119] by *pwv* measurements

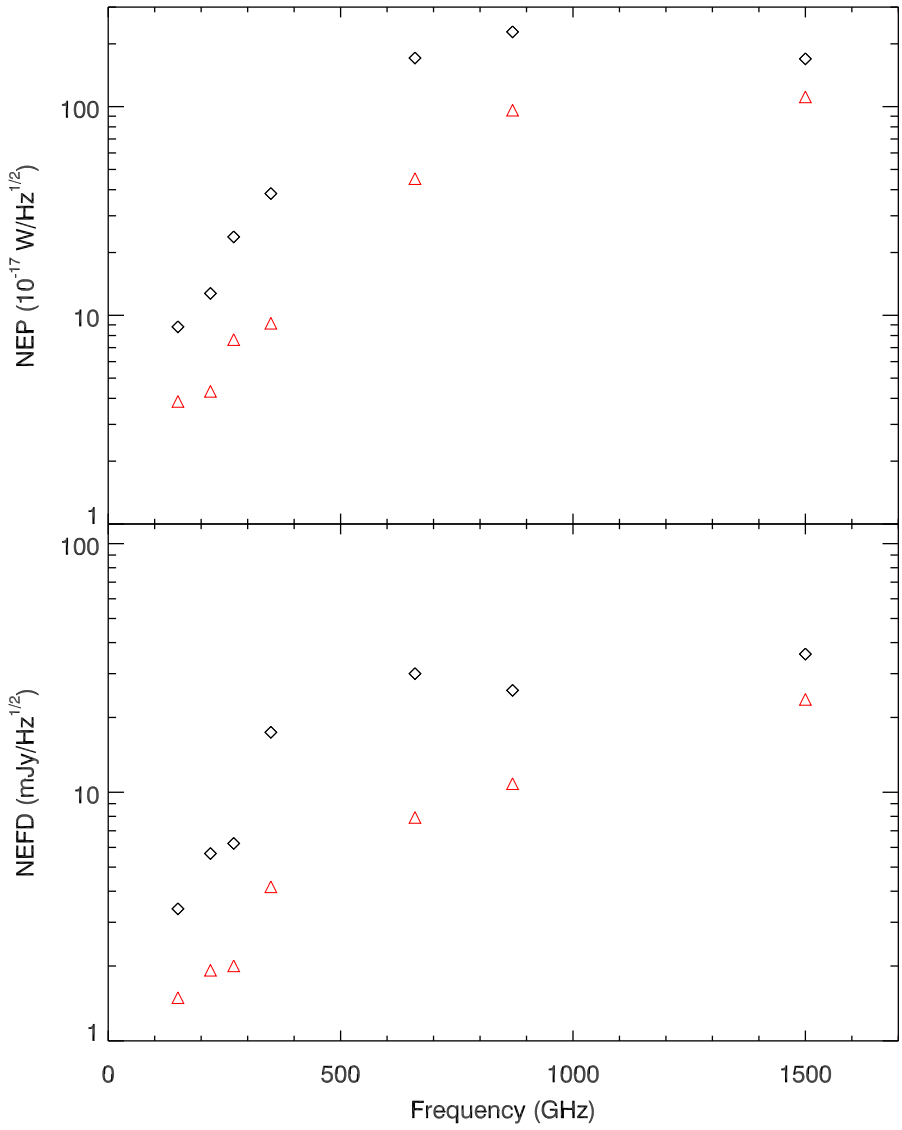

Figure 2.5. Noise Equivalent Power (upper panel) for the seven bands in two extreme atmospheric conditions in the austral winter (red triangles) and summer (black diamonds). In the lower panel, the same for the Noise Equivalent Flux Density.

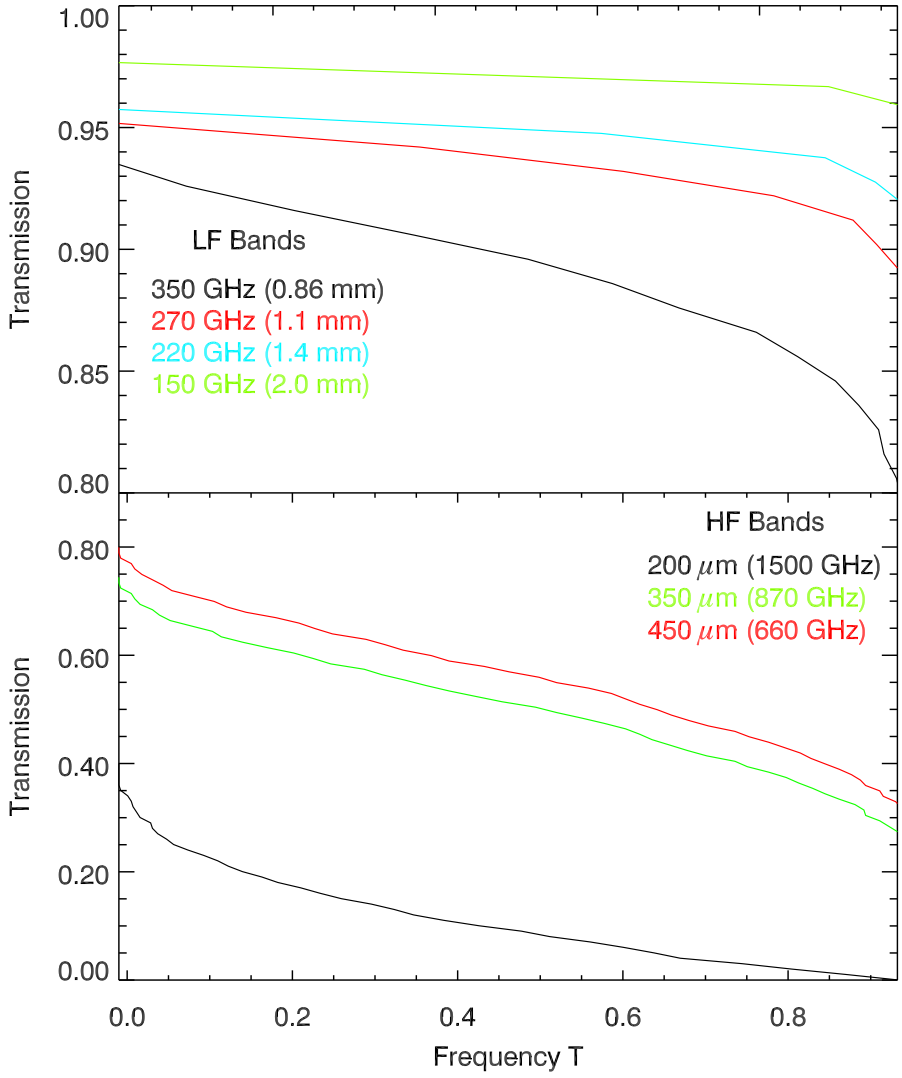

Figure 2.6. Atmospheric transmission vs. cumulative time frequency for Dome C corresponding to the atmospheric windows listed in Table 2.1.

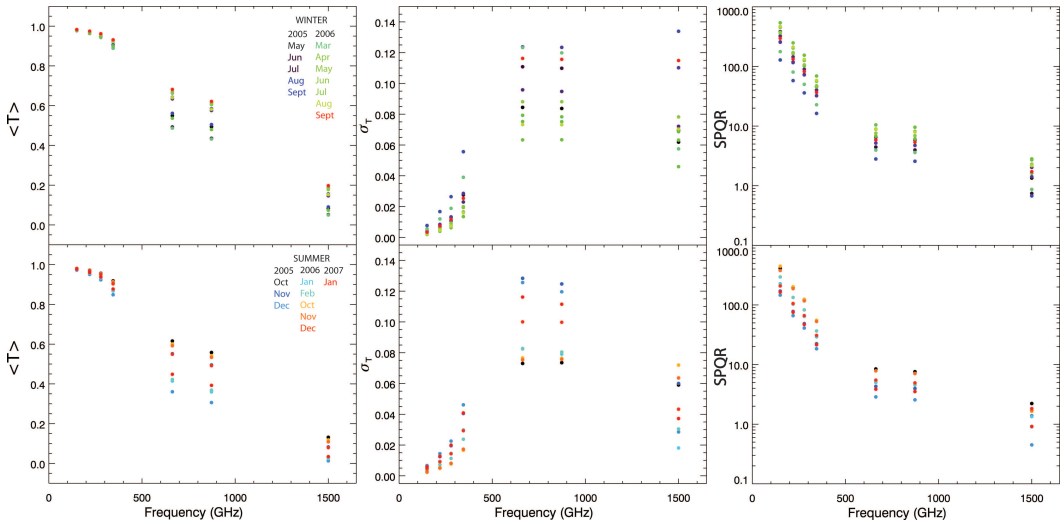

Figure 2.7. Monthly average values of transmission $\langle T \rangle$ and the relative monthly fluctuations σ_T, plotted as rms values, shown in different colors: austral winter months in the upper panel and summer months in the bottom panel. Monthly Site Photometric Quality Ratio (SPQR) values are shown in the right panel.

performed with a portable photometer in January 1997.
Dome C 450 μm window remains above a transmission of 60 per cent for 50 per cent of the time. In [75] the atmospheric transmission at Dome C has been calculated through the 5-years *pwv* data from the South Pole available in [85] and extrapolating the corresponding atmospheric transmission at Dome C using the model in [57]. They found that 450 μm median transmission at Dome C is about 70 per cent. Recently [127] measured a 450 μm median winter transmission at Dome C of about 60 per cent estimating *pwv* with the Microwave Humidity Sounder (MHS) sounding on the National Oceanic and Atmospheric Administration (NOAA) ozonesondeas in 2008.
Dome C median transmission for the 350 μm atmospheric window is about 50 per cent (see the bottom panel in Fig. 2.6), as derived by [115] using the MOLIERE model and 200 μm optical depth measurements.
They found also that the Dome C 200 μm window opens with a transmission of 10 per cent for less then 25 per cent of the time while [127] found that the transmission at 200 μm is about 13 per cent for 25 per cent of the time in 2008.
The 200 μm transmission as a function of the cumulative frequency is the black solid line in the bottom panel of Fig. 2.6: the 25 per cent quartile transmission value is above 10 per cent.
Pwv quartiles since May 2005 until January 2007 (see the right panel in Fig. 2.2) have been compared with Dome C water vapor estimates performed in previous works in Table 2.3.

Table 2.4. Seasonal averages of the SPQR.

	ν_0 (GHz)	Summer	Winter
	150	272	335
LF	220	127	152
	270	79	94
	350	36	42
	660	6	7
HF	870	5	6
	1500	1	2

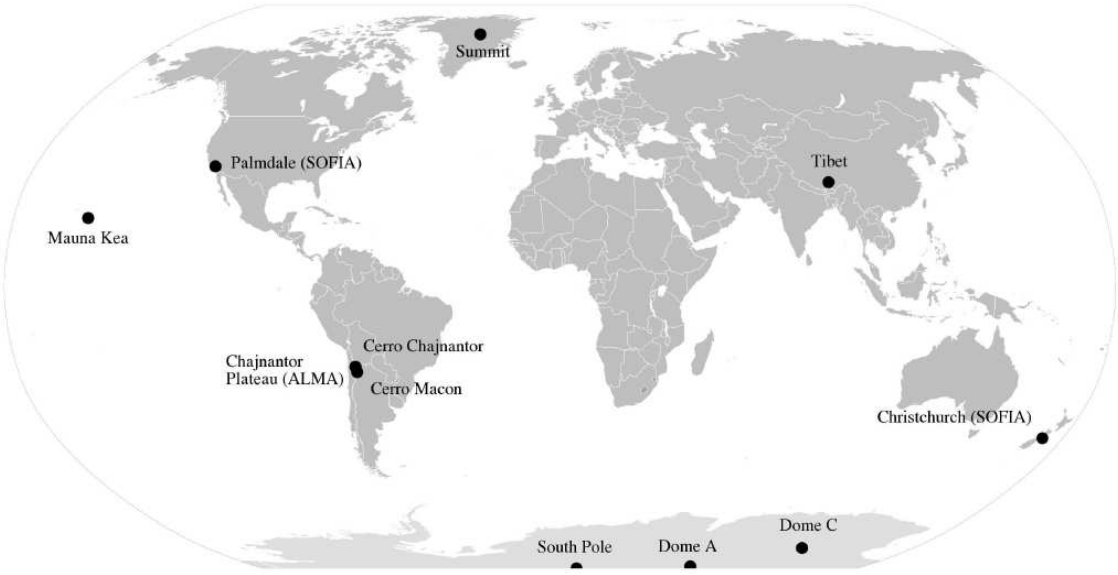

Figure 2.8. Location of the eleven representative sites around the world analyzed by Tremblin et al. (2012).

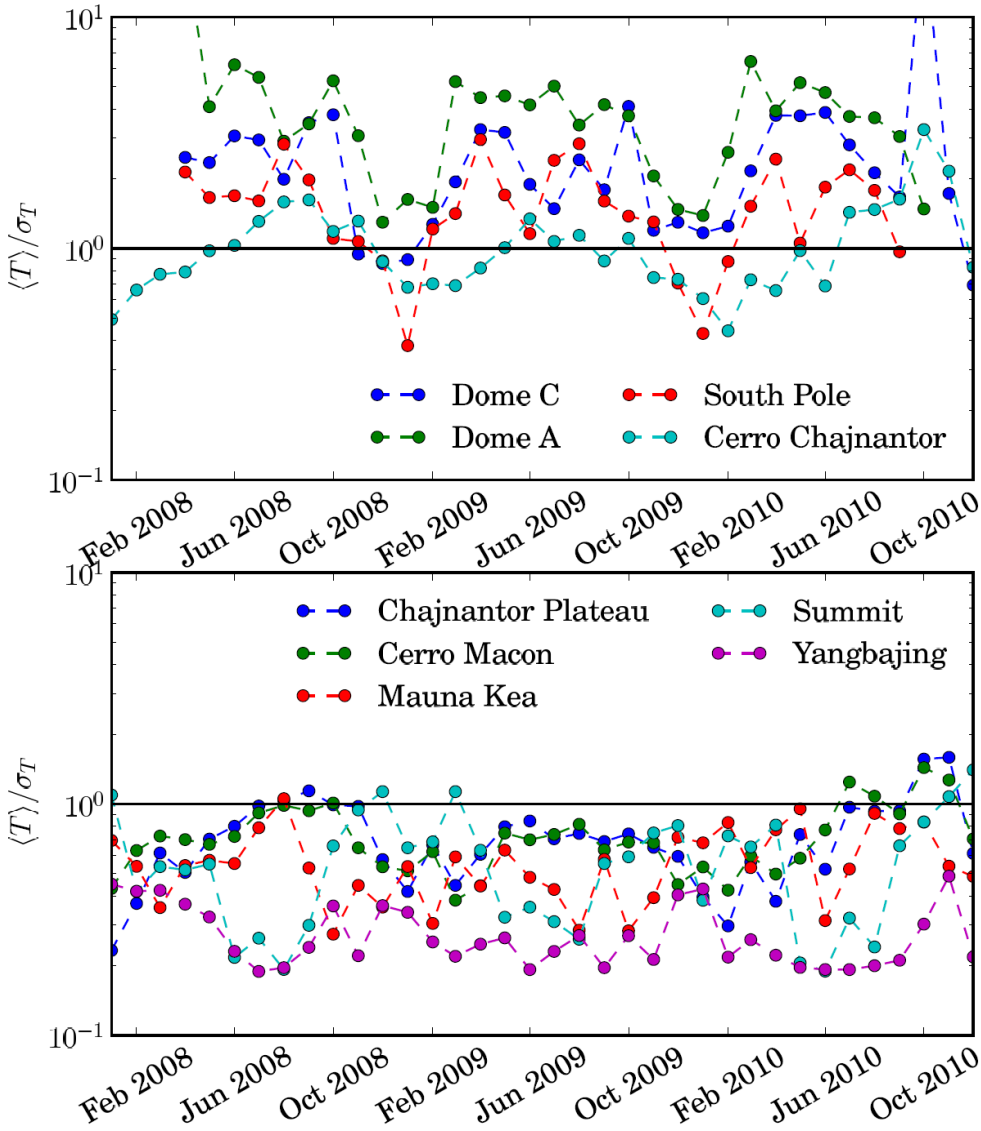

Figure 2.9. SPQR for the 200 μm transmission for all the sites analyzed by Tremblin et al. (2012) between 2008 and 2010.

2.4 High transmission and emission stability

Following an observational approach, the statistics of integrated in-band quantities, like emission and transmission are reported. Both monthly averages $\langle T \rangle$ and relative dispersions σ_T (*rms* values) of in-band transmissions, ranging from May 2005 until January 2007 and splitting between austral summer (from October to February) and winter months (from March to September) are shown in Fig. 2.7.
Monthly averaged transmission fluctuation is a good proxy of emission stability due to the fact that transmission and emission fluctuations are linearly correlated. In addition we assume that the estimated monthly averaged fluctuations, quantified in terms of the standard deviation, could be an underestimate of atmospheric stability because they derive from a daily data sampling, the time interval between two consecutive radiosoundings.
Note that during the austral winter the atmospheric transmission in all the considered bands is generally higher, as expected. $\langle T \rangle$ shows values close to the unity in mm bands and decreases towards THz windows, while relative dispersions σ_T have the opposite trend. As an example, the best atmospheric conditions (in term of high transmission) occur when the atmospheric fluctuations σ_T are larger than others months (red dots in Fig. 2.7). Referring to the atmospheric window centered at 200 μm, when the transmission has the maximum value, the large fluctuations at short time scales are likely to degrade the quality of a scientific observation.
In addition it is not possible to identify the month with the best atmospheric performance as one can see from the gap between two consecutive years atmospheric transmission and fluctuations (red and blue dots in Fig. 2.7).
450μm and 350μm bands transmission show a reduction of few percent ranging from winter to summer months, while fluctuations are not sensitive to seasonal effects.
All the considered bands are characterized by high stability in October (see the black or orange dots in the middle panel of Fig. 2.7) with the exception of the 200 μm window, showing high stability especially during summer months like January or February, when atmospheric transparency is not suitable to perform astrophysical observations.
To quantify the real capability of the observational site we need to study the atmospheric performance, mainly the stability, strongly affected by the weak reproducibility of weather conditions at long time scales. In order to highlight this issue we introduce a specific parameter, the Site Photometric Quality Ratio (SPQR):

$$SPQR = \frac{\langle T \rangle}{\sigma_T} \tag{2.1}$$

relating monthly averaged transmission to its fluctuations, sampled on a daily timescale, for all the considered atmospheric windows. SPQR amplitude provides information about atmospheric performance and it allows us to dermine if high transmission combined with high transmission (i.e. emission) stability conditions are both satisfied for each band. Even if we are not able to identify the desired SPQR threshold, this factor could represent a useful tool to compare several bands performance or sites. In the right panel of Fig. 2.7 monthly values of the Site Photometric Quality Ratio are shown in different colors. The differences between the two years are more evident in SPQR, anyway a decrement of the Site Photometric

Quality Ratio towards THz regime occurs in austral winter as well as in summer periods. Seasonal averaged values of the Photometric Site Quality Ratio in Table 2.4 suggest the good quality of atmospheric conditions in the low frequency bands, notably during the austral winter. Recently the SPQR has been used as indicator to quantify and compare the stability of eleven representative sites all over the world: Antarctic sites like Dome C, Dome A and South Pole, South-American sites like Chajnantor Plateau and Cerro Chajnantor in Chile and Mauna Kea in Hawaii, Summit in Greenland, Yangbajing in Tibet including also Stratospheric sites like SOFIA over Palmdale (USA) and Christchurch (New Zealand) [114] (see Fig. 2.8). In this work the amount of precipitable water vapour has been calculated as the integral of the tropospheric humidity vertical profiles measured by IASI (Infrared Atmospheric Sounding Interferometer). The determination of the transmission corresponding to the PWV for each site has been performed by the atmospheric model MOLIERE-5.7 (Microwave Observation and LIne Estimation and REtrieval) [118]. The estimated variations of the SPQR for the 200 μm window between 2008 and 2010 are shown in Fig. 2.9 and they indicate that all temperate sites have a SPQR ratio lower than 1 (transmission fluctuations greater than the averaged transmission) while Antarctic sites have a ratio greater than 1 (transmission fluctuations lower than the averaged transmission). In addition only Dome A and Dome C monthly-averaged transmission at 200 μm is lower than its fluctuations for at least 25 per cent of the year.

2.5 Effect of broadband filter on optical depth estimate

The average of the optical depth over a band, $\tau_{\nu_0}(\Delta\nu)$, is larger than its central value τ_{ν_0} so the opacity is overestimated by broadband instruments like tippers, as remarked as example by [14]. The determination of this effect is not unique because several *pwv* values could give the same in-band integrated opacity. Low-frequency instruments are less sensitive to this degeneracy even for large values of the bandwidth due to the flatness of the corresponding atmospheric windows. On the other hand a sub-mm broadband instrument overestimates the opacity (underestimates the transmission) and this difference depends on the filter shape as well as on the the atmospheric conditions. Little variations of atmospheric conditions give rise to a dispersion of this overestimate because of the relative shapes of the atmospheric window and the corresponding filter. For each band in Table 2.1 we have included the effect in the relation between the integrated zenith opacity $\tau_{\nu_0}(\Delta\nu)$ and *pwv* values the effect of the instrumental bandwidth $\Delta\nu$ (see Fig. 2.10 and Table 2.5):

$$\tau_{\nu_0}(\Delta\nu) = (a_0 + a_1\Delta\nu) + (b_0 + b_1\Delta\nu)pwv \tag{2.2}$$

a_0 and b_0 are the linear fit coefficients of the $\tau_{\nu 0}$ vs *pwv* relation referred to a narrow band filter matched to the central frequency and a_1 and b_1 take into account the dependency on the instrumental bandwidth $\Delta\nu$, linearly approximated at least in the range within the maximum bandwidths as reported in Table 2.1. Realistic band profiles could highlight the effect instead of our approximation with top-hat profiles. The net result is that the optical depth can be overestimated at most of 30 per cent at 200 μm, assuming the *pwv* best quartile from Table 2.3, while low

Table 2.5. Opacity-*pwv* relation best fit parameters evaluated for the bands of interest.

	ν_0 (GHz)	a_0	a_1	$b_0(\mathrm{mm}^{-1})$	b_1	c_0	c_1
LF	150	0.012	0.0077	0.024	0.0054	0.0016	0.0012
	220	0.015	0.052	0.053	0.030	0.0024	0.0012
	270	0.024	0.016	0.088	0.0070	0.0040	0.0016
	360	0.032	0.073	0.19	0.41	0.0093	0.014
HF	660	0.16	0.021	1.35	1.71	0.066	0.073
	870	0.18	0.68	1.51	1.96	0.074	0.070
	1500	0.53	10.13	5.82	12.69	0.29	0.35

frequency windows are less sensitive to this effect, as expected (10 per cent at 150 GHz).
The uncertainty related to the optical depth value due to the intrinsic scatter of the τ_0 vs *pwv* relation, can be approximated by a linear trend as a function of the instrumental bandwidth:

$$\sigma_{\tau_{\nu_0}}(\Delta\nu) = c_0 + c_1\Delta\nu \tag{2.3}$$

The optical depth uncertainty turns out to be 0.002 at 150 GHz and rise up to 0.3 at 200 μm, assuming the dispersion independent on *pwv* value (see Fig. 2.10). As a consequence the percentage uncertainty on optical depth estimate is about 15 per cent all over the considered atmospheric windows assuming the best *pwv* quartile and it remains above 10 per cent even assuming the 75 per cent quartile in Table 2.3.
The six parameters corresponding to the seven bands are listed in Table 2.5. The Eq. 2.2 is useful to infer the atmospheric opacity at the preferred frequency, with a specific bandwidth, when the *pwv* content is known, but it is important to remind that this relation is appropriate only in the environs of Dome C.
In [115] the opacity is related to the atmospheric *pwv* by means of the MOLIERE model. The resulting linear regression of the *pwv* as a function of the 200 μm opacity and the corresponding best fit parameters in Table 2.5, neglecting a_1 and b_1, gives less than 5 per cent difference in transmission for low *pwv* values. Such a gap could be easily included in the atmospheric performance variations observed at Dome C over the years. Also the difference in transmission evaluated for 220 GHz best fit parameters in Table 2.5 and $\tau_0(225GHz)$-*pwv* linear fit in [119] is lower then 4 per cent.

2.6 Correction of the radiosonde data

A detailed description of the correction procedure used to analyze the raw radiosounding data and determine the vertical profiles of the main thermodynamic parameters is reported. The meteorological data were obtained at Dome C using two Vaisala radiosonde models: (i) the RS92 model for 430 measurement days, i.e. for 94% of the overall days, and (ii) the RS80-A model for 29 radiosonde launches only. Each triplet of signals giving the measurements of P, T and RH at a certain

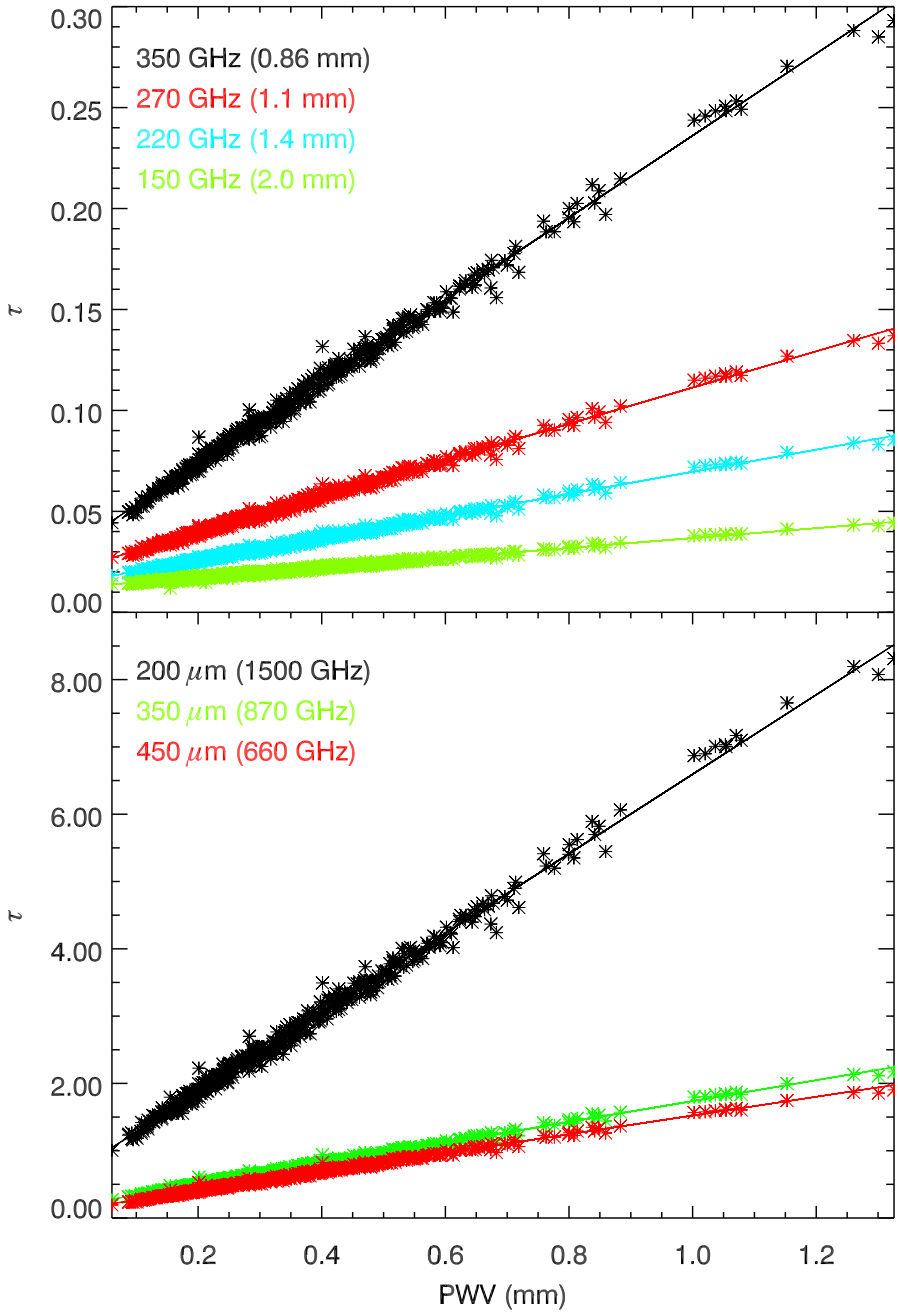

Figure 2.10. Best fit of the correlation between the narrow-band opacity data and atmospheric water vapor for mm windows (top panel) and for the sub-mm bands (bottom panel).

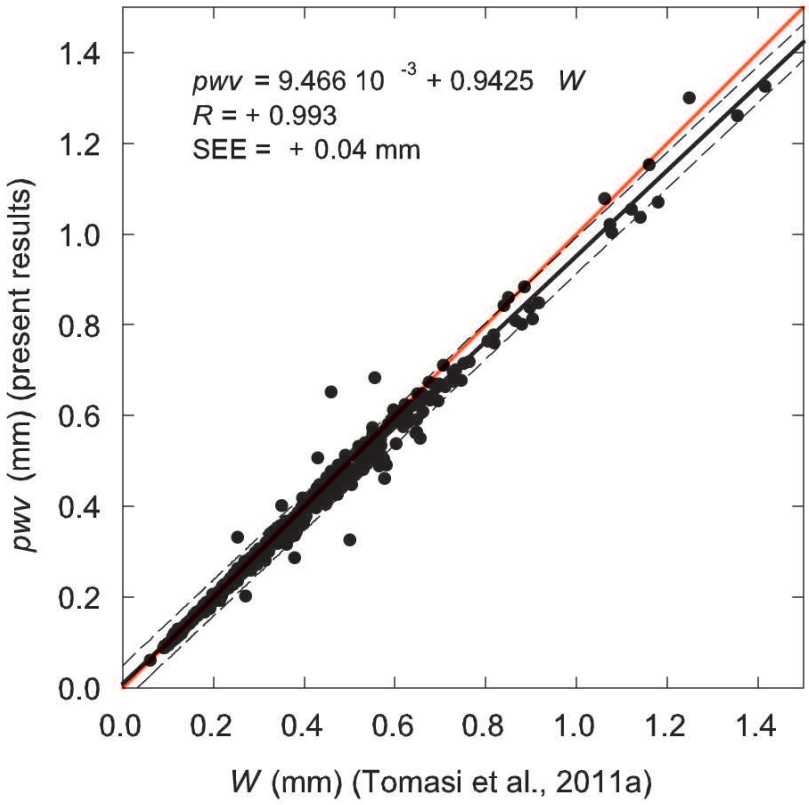

Figure 2.11. Daily values of precipitable water vapor (*pwv*) obtained through the present analysis from surface-level to 8 km amsl, and plotted versus W, the corresponding values of precipitable water derived by Tomasi *et al.* (2011a) over the altitude range from surface-level to 12 km amsl. The data are best-fitted by a regression line with intercept equal to 9.46610^{-3} and slope coefficient equal to 0.9425, which was obtained with regression coefficient R = +0.993, and provided a standard error of estimate SEE = 0.04 mm (credits C. Tomasi).

level was sent by the transmitter onboard the radiosonde to the ground station every 2 s. Considering that the radiosonde ascent rate was in general 5 - 6 m s^{-1}, the triplets of signals were recorded in altitude steps of 10 - 12 m.
The main characteristics of the three sensors (Barocap, Thermocap, and Humicap) mounted on the two radiosonde models are available in Table 1 of [111], where their measurement range, resolution, accuracy, repeatability in calibration, and reproducibility in sounding are given.
The measurements of P, T and RH provided by the radiosonde sensors are affected by a variety of lag and instrumental errors as well as by various dry biases. They were all corrected following the procedure defined by [113], which consists of the following numerous steps:

(1) Pressure: as stated by the manufacturer, the Barocap sensors mounted on the two Vaisala radiosonde models are affected by instrumental errors smaller than

1 hPa over the usual operation range from 630 to 3 hPa at Dome C. The surface-level values of pressure (P_0) measured by the radiosonde a few minutes before the launch were regularly checked through comparison with the simultaneous values of P_0 recorded at 12:00 UTC by the barometer of the Concordia meteorological station. The raw pressure data were analyzed by applying an exponential interpolation procedure in altitude to determine for each radiosounding the values of $P(z)$ at fixed levels, taken in regular steps of 25 m from 3.25 to 4 km, 50 m from 4 to 5 km, and 100 m from 5 to 12 km.

(2) Temperature: the Thermocap sensor mounted on the RS80-A radiosondes was estimated to reach its equilibrium with the ambient air within 30 s at the low temperatures observed at Dome C, which are similar to those of South Pole as shown by [49]. Considering that the radiosondes were routinely left at Dome C in the external ambient air for at least 5 minutes before launch, these thermal lag errors were all neglected. Thus, the temperature data given by the Thermocap sensors were corrected for the errors due to (i) incoming solar and infrared radiation heating, (ii) heat conduction from the other radiosonde components, and (iii) heat exchanges between the sensor and environment. For this purpose, the procedure of [62] was applied to the raw RS80-A Thermocap data. The errors of this kind affecting the RS92 F-Thermocap sensor data were instead neglected according to [61]. The RS80-A lag errors due to air density changes and ventilation effects were removed by using the algorithm of [110], and those of the RS92 data were neglected according to [61]. All the daily vertical profiles of $T(z)$ obtained after such corrections were then analyzed to calculate, through a linear interpolation in altitude, the temperature values at the same fixed levels established above for pressure.

(3) Relative humidity: the raw RH A-Humicap data were estimated by [72] (M04 hereafter) to have a time-constant increasing in a nearly exponential fashion from 0.2 s to about 200 s as air temperature T decreases from 25 °C to −80 °C. Considering that the atmospheric temperature observed at Dome C covers such a range, the lag errors of this kind affecting the RS80-A data were corrected following the M04 procedure. The RS92 time-constant was estimated to assume appreciably smaller values as a result of the improved quality of the H-Humicap sensor [74] (M06 hereafter), and therefore the lag errors of the RS92 data were neglected. The RH data provided by the two Humicap sensors were then corrected by following a complex procedure for the various instrumental and lag errors, based on the following 8 steps:

(a) Comparison of each radiosonde ground-level measurement of RH with that simultaneously recorded by the higrometer of the Concordia meteorological station, to minimize the ground-check errors evidenced by [123] (W02 hereafter) and M04.

(b) Construction of the "skeleton" profile, as recommended by M04, within all the altitude intervals containing sequences of constant data with height, to obtain more schematic and simplified vertical profiles of RH.

(c) Correction of the basic calibration model errors affecting the A-Humicap data using the W02 algorithm, and of those affecting the H-Humicap data of the RS92 radiosondes, taking into account the M06 evaluations of such calibration errors.

(d) No correction for the chemical contamination dry biases for either the A- or H-Humicap models, because the A-Humicap sensors mounted on the RS80-A sondes

were all relatively "young", and the H-Humicap sensors onboard the RS92 sondes were manufactured with improved polymer characteristics. Similarly, no corrections were made for the sensor arm heating errors, found to be negligible with respect to the W02 evaluations.
(e) Correction of the A-Humicap data for temperature dependence dry biases, made according to the [73] criteria and evaluations, and no correction of the dry biases of this kind relative to the H-Humicap data, as suggested by M06 for the radiosondes manufactured after June 25, 2001.
(f) Correction of the sensor aging dry biases, using the W02 algorithm for the A-Humicap data, and no correction of the H-Humicap data, considering the negligible evaluations made by M06 for such errors affecting the RS90 radiosondes, which are equipped with a Humicap sensor model very similar to that mounted on the RS92 sondes.
(g) Correction of the solar heating dry biases affecting the RH data in the presence of incoming solar radiation: (i) those of the A- Humicap sensors were corrected using the algorithm determined by [116] for mid-latitude atmospheric conditions as a function of solar zenith angle SZA, and (ii) those of the H-Humicap sensors using the average correction factors determined by M06 as a function of SZA for the RS90 Humicap sensors.
(h) A final correction of the RH data obtained after the above 7 steps for residual lag errors, following the M04 procedure, which substantially consists of the following three sub-steps: (i) a first smoothing procedure to minimize the small changes in RH with altitude, (ii) a lag correction procedure utilizing the most suitable time-constant values of the A- and H-Humicap sensors, and (iii) a further smoothing procedure to remove any slight discontinuity in each RH vertical profile.
Using the correction procedures described previously, the daily vertical profiles of pressure $P(z)$, temperature $T(z)$ and $RH(z)$ were determined at fixed levels above the surface-level, in regular steps of 25 m from 3.25 to 4 km, 50 m from 4 to 5 km, and 100 m from 5 to 8 km amsl.
In order to calculate the values of absolute humidity $q(z)$ at the same fixed levels, the following procedure was adopted, consisting of the three steps: (i) calculation at each level of the saturation vapor pressure $E(T)$ in the pure phase over a plane surface of pure water, using the well-known [10] formula; (ii) calculation at each level of the water vapor partial pressure $e(z)$ as the product $E(T) \times RH(z)$; (iii) calculation at each level of absolute humidity $q(z)$ (measured in $g\ m^{-3}$) in terms of the well-known equation of state of water vapor, and, hence, as the ratio between $e(z)$ (in hPa) and the product $R_w \times T(z)$ (in K), in which the water vapor gas constant $R_w = 0.4615\ J\ g^{-1}\ K^{-1}$ is put in place of the constant $R_a = 0.287\ J\ g^{-1}\ K^{-1}$ used in the equation of state for dry air.
For all the 469 daily vertical profiles of $q(z)$ obtained using the above procedure, the values of *pwv* were then calculated by integrating each vertical profile of $q(z)$ from the surface-level to 8 km amsl (i.e. up to 4.767 km above the ground level (agl)). The time-patterns of the daily *pwv* values are shown in Fig. 2.11. Two main features are evident in Fig. 2.11, showing that the majority of *pwv* values are lower than 0.3 mm during the austral autumn months, although presenting largely dispersed patterns (of 50% or more), and, hence, low stability. As shown by [111], a limited contribution is given to the overall value of atmospheric *pwv* by the amount of water

vapor present in the Upper Troposphere and Low Stratosphere (UTLS) region from 8 to 12 km amsl, while negligible fractions of *pwv* ranging mainly between 0.003 and 0.005 mm throughout the year are present in the stratosphere from 12 to 50 km above Dome C [112].

To verify the reliability of the present estimates of *pwv*, a comparison is made in Fig. 2.4 between the present daily values of *pwv* and those correspondingly determined by [111] (indicated as W) using a more advanced correction procedure from surface-level to 12 km amsl. The comparison showed that a close relationship exists between the present results and those of [111], defined by a regression line with nearly null intercept and slope coefficient of + 0.9425, having regression coefficient better than + 0.99, and providing a standard error of estimate equal to 0.04 mm. These findings clearly indicate that the present evaluations of *pwv*, as obtained over the altitude range from surface-level to 8 km amsl, are fully suitable for the purposes of our study, especially considering the intrinsic uncertainty of the simulation model.

Chapter 3

Monitoring of atmospheric performance

Ground-based cosmological observations need a detailed knowledge about atmospheric transmission. A continuous monitoring of the transmission in the mm/submm wavelength range is needed mainly due to H_2O high frequency variations along the line of sight of a telescope.
CASPER2 (Concordia Atmospheric Spectroscopy of Emitted Radiation) is a spectrometer devoted to measurements of atmospheric emission in the 90 ÷ 450 GHz (3÷15 cm^{-1}) spectral region [27]. The instrument allows a continuous monitoring of the atmospheric transmission of the same sky region explored with MITO telescope, during cosmological observation. The site guarantees the ideal conditions for measurements in mm wavelength band: cold and dry atmosphere together with a low content of *pwv*.
The instrument concept and its major characteristics are described in Sec. 3.1. A discussion about the Martin-Puplett interferometer (MPI) and the options adopted for signal sampling are presented in Sec. 3.2. Preliminary atmospheric spectra as recorded at MITO in July 2010 are finally shown in Sec. 3.6.

3.1 The spectrometer CASPER 2

CASPER2 is composed by a two-mirrors telescope, an interferometer, a wet cryostat and an altazimuthal mount. The atmospheric emission spectra are acquired by a MPI that can be easily converted into a spectropolarimeter with many consequent scientific applications. The detectors, two Ge-bolometers with a NEP $\sim 10^{-15}$ W $Hz^{1/2}$, are cooled down to 290 mK by a wet cryostat, using liquid nitrogen and helium in combination with a He^3 fridge. The cryostat (Infrared Labs, HDL-8) is identical to the one described in [18]. In Fig. 3.2 a schematic CAD drawing of CASPER2 is shown. The optical design satisfies the expected measurements requirements: a low resolution spectrometer in the range of 90 - 450 GHz (R $\sim$ 50) and a small field of view (less than 1 degree). To fulfill these goals we have matched a two-mirrors telescope with a MPI. The optical layout with the main components is shown in Figure 3.3. A f/3.5 Pressman-Camichel telescope collects sky radiation and feeds one of the two input ports of the MPI. With this optical solution the wavefront

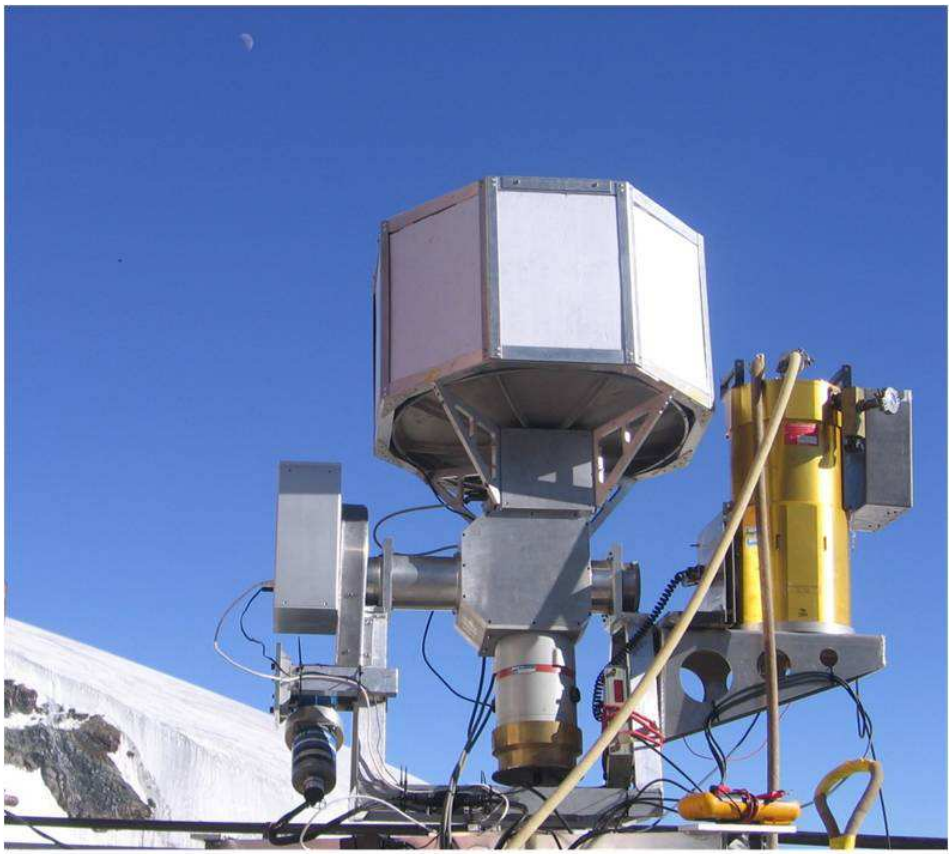

Figure 3.1. CASPER2 in operation at Testa Grigia station (3480 m a.s.l.) close to MITO telescope during the July 2010 observational campaign.

Table 3.1. CASPER2 instrumental main features.

Telescope	f/3.5 Pressman-Camichel
Telescope effective focal lenght	1621 mm
Primary mirror diameter	620 mm
Primary mirror conic constant	0
Primary curvature radius	978.4 mm
Secondary mirror diameter	120 m
Secondary mirror conic constant	8.86
Secondary curvature radius	354.9 mm
Entrance pupil diameter	460 mm
Field of view (FWHM)	26 arcmin
$A\Omega$	0.05 cm^2 sr
Interferometer	Martin-Puplett
Spectral range	Channel 1: 90 ÷ 360 GHz
	Channel 2: 90 ÷ 450 GHz
Mechanical path difference	30 mm
Spectral resolution	5 GHz
Detectors	2 composite NTD bolometers @ 0.3 K
Calibrator	Eccosorb AN72
Mount	altazimuthal
Pointing error	1 arcmin
CCD field of view	(14.4 x 13.6) arcmin

aberrations introduced by the 62-cm concave spherical primary mirror ($M1$) are compensated by a 12-cm convex ellipsoidal subreflector ($M2$). The primary mirror is underilluminated by the secondary mirror, which operates as an aperture stop of the telescope alone resulting in a 46-cm in diameter entrance pupil. Both the mirrors have been manufactured in an aluminum alloy, ensuring a fast and an homogeneous thermalization of the surfaces. The mirrors have been carefully polished to reflect visible light: the final rms surface roughness is lower than 0.1 μm. The primary mirror has been manufactured by Officine Ottico Meccaniche Marcon di San Doná di Piave (Italy) while the ellipsoidal subreflector by the INFN machine shop at the Department of Physics in Rome. The secondary mirror is maintained in the right position along the telescope axis by a 2 cm thick polystyrene foam plate (ST) (BASF, Styrodur 3035N), allowing a null obscuration due to the subreflector support also avoiding the possible consequent diffracted radiation. Laboratory measurements show high transmission value ($> 97\%$) and low polarization ($< 1\%$) of this material in the whole band. The telescope is shielded from off-axis unwanted radiation (*i.e.* Sun during daytime measurements) by 8 panels with inner reflective surfaces, 0.5 mm thick Peraluman sheets, shaped as vanes to operate like roof mirrors [38].

3.1.1 Optics

A 45 degrees tilted wire-grid ($WG1$) linearly polarizes the transmitted sky radiation focused by the telescope (in_1) (see Fig. 3.3). The radiation emitted by a reference source at ambient temperature (in_2), realized by a disc of Eccosorb AN72, enters, as

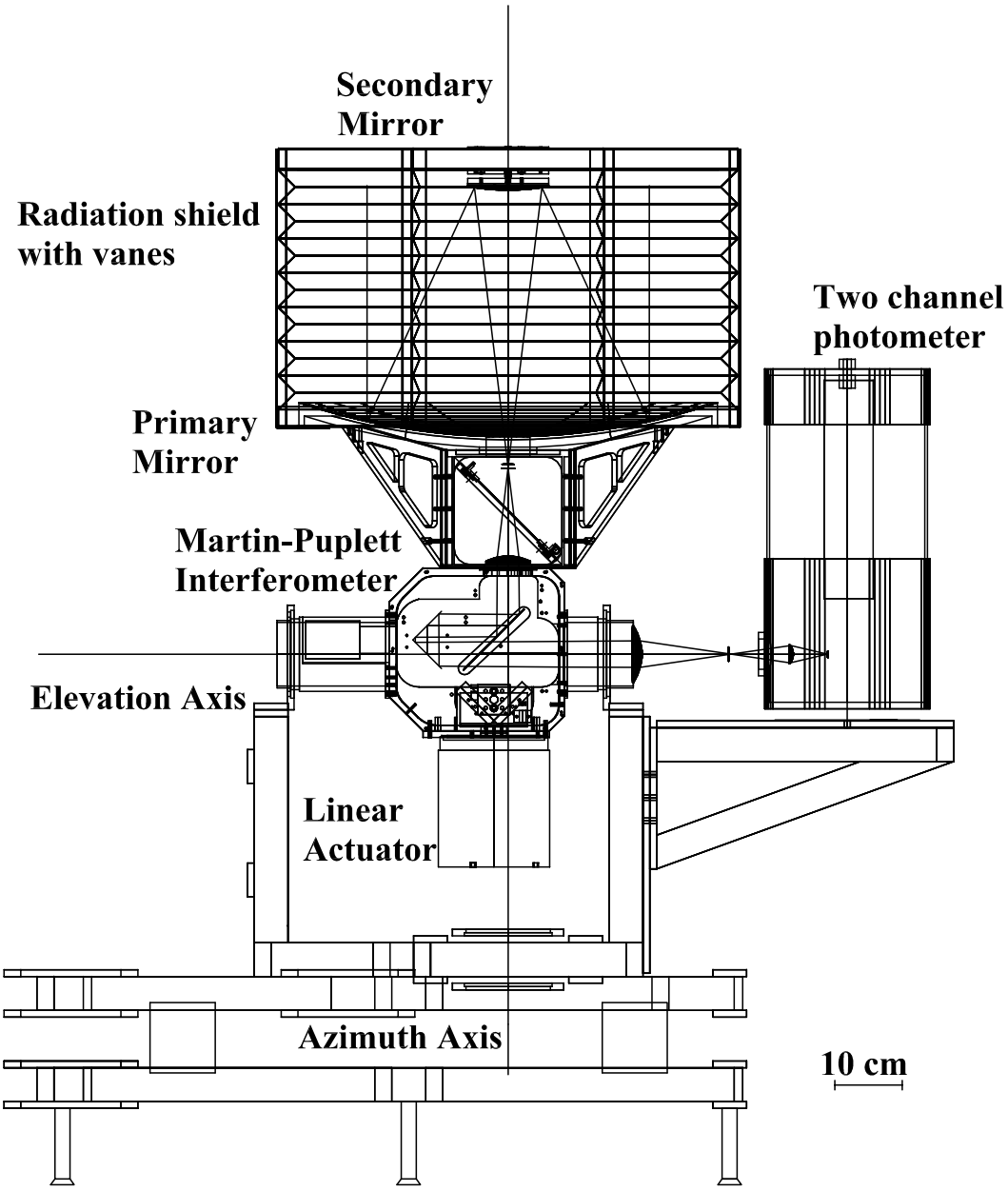

Figure 3.2. CAD drawing of CASPER2 (credits S. De Gregori).

the second input port of the MPI, reflected by $WG1$ with a perpendicular polarization. An alternative colder reference source, more close to atmospheric emission, is under consideration. The two inputs are combined in planar waves, at the entrance of the MPI, by a HDPE (High Density PolyEthylene) plano-convex lens ($L1$). A second wire-grid ($WG2$), still tilted at 45 degrees inside the MPI, is rotated around the optical axis of 35.26 degree to correctly split the two polarization axes. It acts as beam splitter separating the linearly polarized incoming radiations in two orthogonal components. Two 90 degree roof-mirrors ($RM1$ and $RM2$), diamond-turned stainless steel, can move along the two split optical beams changing the Optical Path Difference (OPD). $RM1$ is mounted on a linear stage (AICOM S.P.A., Model SMP-123) to perform a ± 15 mm mechanical path difference, corresponding to a 5 GHz spectral resolution, while $RM2$ is sinusoidally wobbled by a shaker (Lynge Dynamic System, Model 409) on a linear stage with an amplitude of 1 mm around (see Sec. 3.3.3).
The radiation undergoes a polarization rotation of 90 degrees when reflected back on the roof mirrors. A second HDPE plano-convex lens ($L2$) focuses the beam, exiting from the MPI, in front of the cryostat window. The last HDPE plano-convex lens ($L3$) is mounted inside the cryostat, on the radiation shield of the helium liquid tank, cooled down to 1.6 K. This lens refocuses the radiation towards two detectors, i.e. the two output ports, after the splitting of the two polarization states by the third wire-grid ($WG3$), cooled down to 300 mK. Channel 1 is the port corresponding to the transmitted radiation, and Channel 2 the other. All the wire-grid polarizers have 10-μm in diameter tungsten wires spaced by 25-μm and show an efficiency in the reflected and transmitted polarizations better than 10^{-3} in our spectral range.
The first two lenses, L1 and L2, have been carefully shaped to image the subreflector on $L3$, at least for the Zero Path Difference (ZPD) $RM1$ position, defining it as the cold aperture stop of the full optical system, *i.e.* the Lyot stop. We have the possibility to select the last optical element as aperture stop only because a single pixel is present at the focal plane. Incidentally $L3$ is the exit pupil too. The optical design has been developed with ZEMAX[1] ensuring diffraction limited performances in the whole $90 \div 450$ GHz spectral range.
The two bolometers are illuminated by f/3.5 Winston cones with a 10.5 mm in diameter aperture entailing a throughput of 0.05 cm^2 sr.
The optical axis, from the MPI exit to the cryostat entrance window, overlaps the elevation axis, ensuring a vertical position for the cryostat for all the telescope pointing positions. The optical consequences of this choice, as derived by the variable orientation between the wire grids with the elevation angle, are discussed in Sec. 3.2.1.
After fixing the telescope configuration and assuming a fov equal to 28 arcminutes (FWHM) we have limited the lower value for the focal length of the lens $L1$, f_{L1}, to satisfy the Jacquinot condition. The minimum spectral resolution can be related to telescope-MPI optical matching in the following way:

$$\delta\nu \geq \frac{\nu_{max}}{8}\left(\frac{d_{tfs}}{f_{L1}}\right)^2 = \frac{\nu_{max}}{8}\left(\frac{fov f_{tele}}{f_{L1}}\right)^2 \tag{3.1}$$

[1] ZEMAX Development Corporation; www.zemax.com

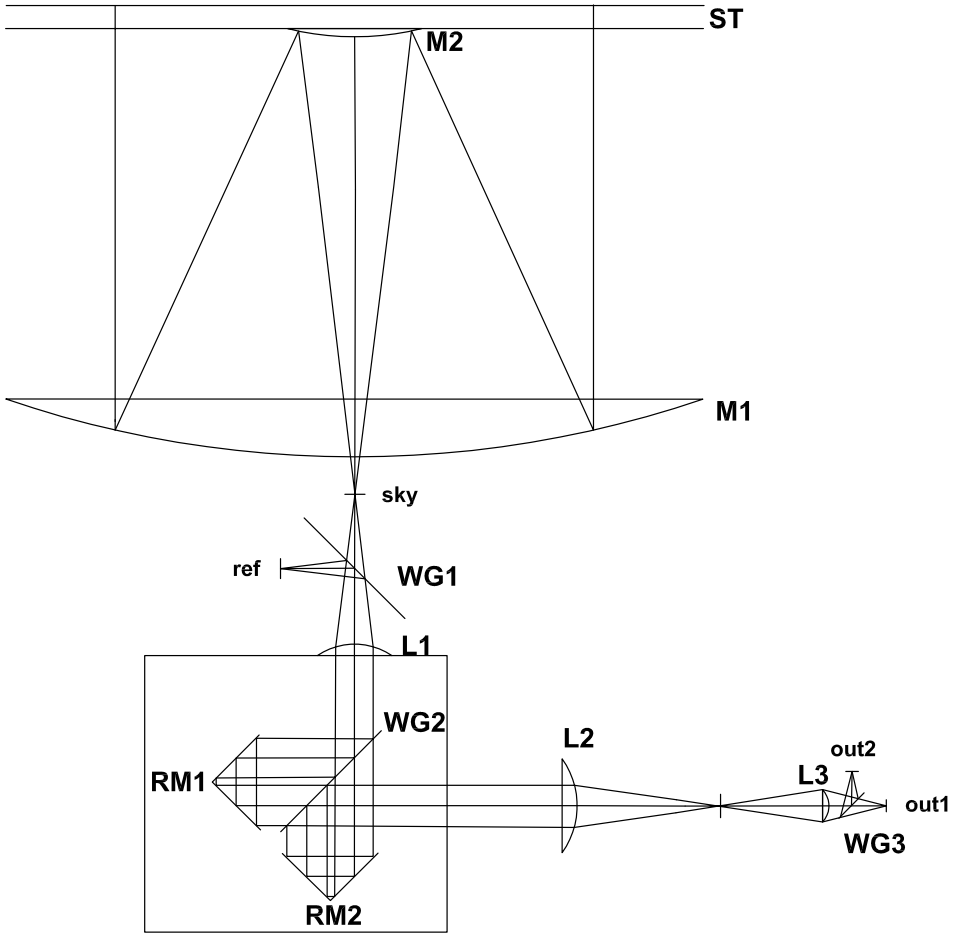

Figure 3.3. CASPER2 optical layout: all the labelled components are described in the text (credits M. De Petris).

where ν_{max} is the maximum frequency (450 GHz), d_{tfs} the telescope field stop diameter (13.2 mm) and f_{tele} the telescope effective focal length (1621 mm). In our case f_{L1} has been chosen equal to 145 mm satisfying the Jacquinot condition up to R$\sim$1000 at ν_{max}.

3.1.2 Filters chain

Blocking filters are employed in our system in order to reduce radiative input on the different cryogenic stages in the cryostat (and consequently on the bolometers) while mesh filters to select the frequency bandwidth of interest. In Table 3.2 all the components in the filters chain are listed. Measurements are performed inside two similar bandwidths: 90$\div$360 GHz for Channel 1 and 90$\div$450 GHz for Channel 2. Channel 2 has been spectrally enlarged to explore high frequency atmosphere emission more prone, and so more sensitive, to *pwv* fluctuations at the expense of a larger background emission with consequent photon noise: 0.5 nW and 1 nW respectively, under the assumption of a $pwv = 1$ mm.

Table 3.2. Filters chain characteristics

type	cut (GHz)	Temperature (K)
Quartz window	off (> 3000)	300
ARC quartz + black polyethylene	off (> 1200)	77
Yoshinaga	off (> 1650)	1.6
Mesh	off (> 450)	1.6
Yoshinaga	off (> 1500)	0.3
Mesh channel 1	off (> 360)	0.3
Mesh channel 2	off (> 450)	0.3
Winston cones	on (< 90)	0.3

The vacuum window of the cryostat is a 4 mm thick quartz window. The 77 K quartz filter is 3.3 mm thick with a diamond powder ARC. A black polyethylene filter, 0.1 mm thick, is employed to reduce visible and NIR background. At 1.6 K a Yoshinaga filter blocks IR radiation while an interference mesh filter limits the high frequencies at 450 GHz. On the entrance apertures of the two Winston cones at 300 mK, two Yoshinaga filters work as last IR blockers. Two final mesh filters perform the effective band selection. All the filters have been supplied by QMWC Instruments, Ltd. The lower limit band in frequency is dictated by the output aperture of the Winston cones operating like high-pass filter.

3.1.3 Electronics and data acquisition

The first stage for the read out of the bolometer signals are JFETs (model IFN146) in a common-drain configuration. Those unitary gain amplifiers are mounted on the He^4 tank inside an aluminum shielded box, close to the detectors, but at a temperature of 120 K by self-heating. The measured noise is ~ 3 nV/$\sqrt{Hz}$. The expected total incident power on the detectors is 0.5 nW and 1 nW respectively, implying a sensor thermal conductivity of the order of 10^9 W/K (Haller-Beeman). The low impedance signals from the JFETs feed an ambient temperature differential preamplifier with a gain equal to 250 for both the channels and an output noise $\sim$ 10 nV/$\sqrt{Hz}$ for frequency higher than 20 Hz. Rechargeable batteries inside the preamplifier box supply the bias voltage, as well as all the read out electronics boards and cryogenics maintenance. All the electrical connections are ensured by twisted pairs of NbTi wires (0.1 mm diameter) shielded within CuNi (0.03 mm thick). Depending on the signal modulation (see Section 3.3) the data acquisition is carried out, depending on the chosen modulation technique, by a low frequency (<1 Hz) data sampling of two synchronous demodulation amplifiers (Stanford Research Instruments, SR850) or a high frequency (5 kHz) data sampling by a DAC (Digital to Analog Converter, National Instruments).

3.1.4 Pointing System

The pointing system has been developed with a twofold aim. The first is to track in the sky the field of view of MITO telescope during its observations, exploring in this way an identical optical path through the atmosphere, while the second goal is

to be able to point specific directions to perform skydips for every azimuth angle. The telescope control is realized with Magellano ST7, supplied by ATEC Robotics (Advanced Technologies for Research and Industry). The movement of the two axes is performed by hybrid stepper motors (MAE, HS200) while the position is transduced by two incremental encoders (Baumer Electric, BHK 16OSA400). Both encoders ensure an accuracy of 400 steps/turn and they have a zero position to record and to reset the sky coordinates every observational run. This reference position also corresponds with the telescope rest position.
The gear ratio for altitude (and azimuth) axis is equal to 5.1 employing two gear wheels with 112 and 22 teeth each. In order to have stable and accurate movements, this low value has been increased by a right angle gear (TLS, Sf40/PB3) with a 100:1 gear ratio. Finally the total gear ratio is 510. The transmission is ensured by two gear belts (Trasmecam, HTD 1040-8M-20 for altitude axis and 1200-8M-20 for azimuth axis).
A CCD camera (SBIG, ST-402ME) is used to check the pointing system, as star tracker. It is provided with a 135 mm focal length lens to have a total field of view of 14.4' x 13.6', with a field of view per pixel of about 14". The limit magnitude is 15 [30].
The co-alignment between visible and millimeter axes has been checked in laboratory with a fixed artificial source, considering its finite distance, and than verified *in situ* by pointing planets. The final error in pointing is lower than 1 arcminute, more than enough for atmospheric emission measurements.
The whole instrument is accommodated inside a 1.6x2.9x1.4 m (WxDxH) deployable dome in PVC Prećontraint ® 502 (AMA, series 8000).

3.2 The Martin-Puplett interferometer

Stokes and Mueller matrix formalism can be used to describe any state of polarization and superposition of beams when no phase relation has to be taken into account. Alternatively, as for example in the analysis of an interferometer, one needs to perform a Jones matrix calculation, reverting to the Mueller matrix formalism afterwards [18].
Unpolarized radiation at the entrance of the two input ports can be assumed and we describe it with the Stokes formalism as:

$$S_{in} = B_{in} \begin{pmatrix} 1 \\ 0 \\ 0 \\ 0 \end{pmatrix} \tag{3.2}$$

where in stands for in_1 and in_2, the two input sources.

The two signals pass through $WG1$ and are linearly polarized in the following way:

$$S'_{in} = M_{WG1} \cdot S_{in} = B_{in} \begin{pmatrix} 1 \\ \cos 2\vartheta_{in} \\ \sin 2\vartheta_{in} \\ 0 \end{pmatrix} \tag{3.3}$$

where ϑ_{in} is the projected angle of the $WG1$ principal axis on the plane orthogonal to the optical axis. The angles for the two inputs are linked as: $\vartheta_{in_2} = \vartheta_{in_1} + \pi/2$. $\vartheta_{in_1} = 0$ degrees corresponds to the vertical position. The Muller matrix used for a wire grid is

$$M_{WG} = \begin{pmatrix} 1 & \cos 2\vartheta_{in} & \sin 2\vartheta_{in} & 0 \\ \cos 2\vartheta_{in} & \cos^2 2\vartheta_{in} & \cos 2\vartheta_{in} \sin 2\vartheta_{in} & 0 \\ \sin 2\vartheta_{in} & \cos 2\vartheta_{in} \sin 2\vartheta_{in} & \sin^2 2\vartheta_{in} & 0 \\ 0 & 0 & 0 & 0 \end{pmatrix} \tag{3.4}$$

After the MPI, each exiting beam can be described as:

$$S''_{in} = M_{MPI} \cdot S'_{in} = B_{in} \begin{pmatrix} 1 \\ \cos 2\vartheta_{in} \cos\delta \\ -\sin 2\vartheta_{in} \\ \cos 2\vartheta_{in} \sin\delta \end{pmatrix} \tag{3.5}$$

where we used the Muller matrix for an ideal MPI

$$M_{MPI} = \begin{pmatrix} 1 & 0 & 0 & 0 \\ 0 & \cos\delta & 0 & \sin\delta \\ 0 & 0 & -1 & 0 \\ 0 & \sin\delta & 0 & -\cos\delta \end{pmatrix} \tag{3.6}$$

The mechanical path difference between the two split beams is Δx_{mec}. The OPD, Δx_{opt}, equal to $2\Delta x_{mec}$, is related to the phase shift, δ, for each wavelength, λ, as well known: $\delta = 2\pi\Delta x_{opt}/\lambda$.

$WG3$ splits each beam in the output ports in the following way:

$$\begin{gathered} S'''_o = \\ M_{WG3} \cdot S''_{in} = \\ B_{in} \begin{pmatrix} 1 + \cos 2\vartheta_{in} \cos 2\varphi_o \cos\delta - \sin 2\vartheta_{in} \sin 2\varphi_o \\ \cos 2\varphi_o + \cos 2\vartheta_{in} \cos^2 2\varphi_o \cos\delta - \sin 2\vartheta_{in} \sin 2\varphi_o \cos 2\varphi_o \\ \sin 2\varphi_o + \cos 2\vartheta_{in} \sin 2\varphi_o \cos 2\varphi_o \cos\delta - \sin 2\vartheta_{in} \sin^2 2\varphi_o \\ 0 \end{pmatrix} \end{gathered} \tag{3.7}$$

where o stands for out_1 or out_2, corresponding to the two output ports optically matched to Channel 1 and Channel 2, respectively.

Due to the fact that our detectors are only sensitive to signal intensity, *i.e.* the first element of Stokes vector, we can express the signals of the two output ports as:

$$I_{out_1} = \Delta^+ + \Delta^- \cos 2\vartheta_{in_1} \cos 2\varphi_{out_1} \cos\delta - \Delta^- \sin 2\vartheta_{in_1} \sin 2\varphi_{out_1} \tag{3.8}$$

$$I_{out_2} = \Delta^+ - \Delta^- \cos 2\vartheta_{in_1} \cos 2\varphi_{out_1} \cos\delta + \Delta^- \sin 2\vartheta_{in_1} \sin 2\varphi_{out_1} \tag{3.9}$$

where $\Delta^+ = B_{in_1} + B_{in_2}$ and $\Delta^- = B_{in_1} - B_{in_2}$ and rewriting $\varphi_{out_2} = \varphi_{out_1} + \pi/2$.

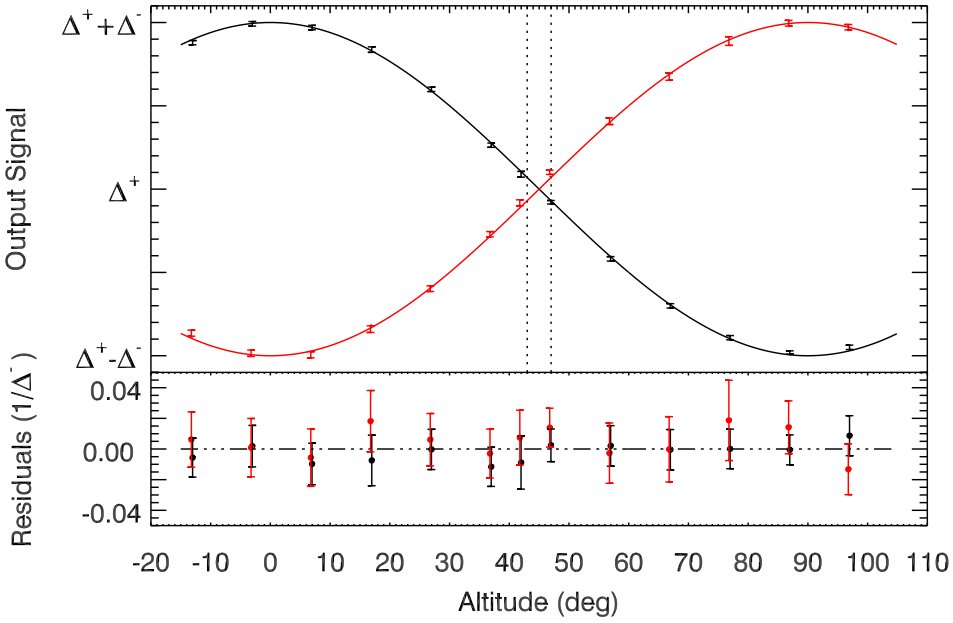

Figure 3.4. Dependence between ZPD output signals (black points for Channel 1 and red points for Channel 2) and altitude angle. The two vertical dashed lines limit the "*blind*" observational range where the signal to noise ratio is lower than 3. In the bottom panel the normalized signals with the instrument function removed are shown.

Under the assumption that $\vartheta_{in_1} = \varphi_{out_1}$, *i.e.* the polarization axis of $WG1$ is aligned with the $WG3$ one, we can rewrite Eqs. 3.8 and 3.9 in the following way:

$$I_{out_1} = \Delta^+ + \Delta^- \cos\delta \tag{3.10}$$

$$I_{out_2} = \Delta^+ - \Delta^- \cos\delta \tag{3.11}$$

The spectra of the two input sources are linked to the Eqs. 3.8 and 3.9 in Sect. 3.4.

3.2.1 MPI efficiency *versus* telescope altitude

The cold $WG3$, inside the cryostat, is at rest during telescope altitude movements. Its wires change orientation by an angle φ_{out_1} with respect the input polarizer $WG1$, linked to the altitude angle α as $\phi_{out} = \theta_{in_1} + \alpha - \frac{\pi}{2}$. For this reason we refer to the function $f(\alpha)$, as an instrumental efficiency, the signal dependence with the altitude. This has to be carefully taken into account to characterize the pointing performance. The two outputs at ZPD, see Eqs. 3.8 and 3.9, can be expressed as:

$$I_{out_{1,2}} = \Delta^+ \pm \Delta^- f(\alpha) \tag{3.12}$$

where $f(\alpha) = cos2\alpha$.
When $\alpha = 45$ degree the signals, even modulated by $\cos\delta$ along the interferogram, are null. To check this expected instrument efficiency we have filled the sky input

with a blackbody source at ambient temperature (an Eccosorb AN72 sheet in front of the telescope) and, in order to get a high signal-to-noise ratio, we employed a Hg-lamp as reference source instead of the disc of Eccosorb AN72. Spectra have been acquired at altitude angles ranging from -10 degrees to 100 degrees. Altitude angles lower than 0 degrees and higher than 90 degrees have been explored to check the consistency and the repeatability of the performance. Interferograms have been recorded in fast scan mode (see Sect. 3.3.2) with a 5 kHz scan rate, performing the time average over an acquisition time of about 7 minutes for altitude values ranging from 30 degrees to 60 degrees (lower instrumental efficiency), and of 5 minutes for the others (higher instrumental efficiency). In Figure 3.4 the two ZPD output signals are plotted versus the altitude angle, with error bars given by the standard deviation. At zenith, Channel 1 is proportional to $\Delta^+ + \Delta^-$, after an intensity decreases down to a null signal ($\Delta^- = 0$), the rotation of polarization axis inverts the signal at horizontal position. The red points represent the polarized signal detected by Channel 2, as expected the trend is symmetric to the other. Data points are well-fitted by the $\pm cos2\alpha$ function predicted by the Eq. 3.12 (see the residuals in the bottom panel of Fig.3.4). The loss of efficiency, due to the change of WGs orientations along different zenithal angles, entails an altitude range where the signals are negligible. In order to determine the width of this altitude range where the instrument has low efficiency, what we call the "*blind*" observational range, we have estimated α_{min} and α_{max} corresponding to a signal-to-noise ratio ≤ 3. An emission atmospheric spectra, as derived by ATM with a $pwv = 1$ mm, has been assumed as source. The vertical dot-dashed lines in Figure 3.4 limit this "*blind*" orientation directions: 43 degrees $< \alpha <$ 47 degrees.

This is a restriction on CASPER2 performance but it has little consequences for our purposes because the minimum altitude explored by MITO telescope is 42 degrees. This operational limit for MITO telescope is dictated by low atmospheric contamination requirements and by dome constraints. Anyway CASPER2 can point lower altitudes, where the signal-to-noise ratio increases, allowing a complete angular range skydips.

The expected variation in the atmospheric emission during skydips, due to the decreasing opacity with the altitude, has to be added to the instrumental efficiency. Each detector records a signal that can be expressed as:

$$I_{out_{1,2}} = \Delta^+(\alpha) \pm \Delta^- a(\alpha) f(\alpha) \tag{3.13}$$

where $a(\alpha)$ is the atmospheric dependence and Δ^- is the input signals difference at zenith position. Due to the different spectral bands, Δ^+ and Δ^- have to be distinguished between the two channels. In a simple atmospheric layer model we can assume

$$a(\alpha) = exp(-\csc(\alpha)) \tag{3.14}$$

normalized at zenith position.

3.2.2 The sub-interferometer: Mickey

A Michelson sub-interferometer, named Mickey, ensures the monitoring of the movements (position and velocity) of $RM1$ during fast scan measurements. The movable mirror is mounted on the back side of $RM1$. The source is a laser (Imatronic, Sigma 650/3) centered at λ=650 nm. Interference maxima are detected by a photodiode (Osram, SFH203) and then processed by a peak-counter circuit. Accuracy on the mirror position depends on the distance between the peaks generated by Mickey, equal to λ=325 nm.
The Fourier Transform of the signal detected by Mickey along a return double-sided interferogram shows two maxima, corresponding to a backward and forward scan velocities difference of about 70 μm/s. The peak-counter circuit is employed to produce a trigger signal for data collection. In this way all fast scan interferogram points are acquired at the same distance between each other, independently of velocity changes due to the step motor [30].

3.2.3 Thermal monitoring

An AD590 temperature sensor is employed to monitor the absolute temperature of the reference load. The reference source passively follows the ambient temperature as well as the whole instrument. The MPI box and the primary mirror are also monitored for estimating possible differential emission in the instrument due to temperature gradients. The AD590 is a temperature transducer producing an output current proportional to absolute temperature, suitable for our purposes: wide temperature range (-55 C ÷ 150 C), high calibration accuracy (±0.5 C) and excellent linearity (±0.3 C over full range).

3.3 Signal modulation techniques

The peculiarity of CASPER2 is the ability to perform, with the same interferometer, 3 different signal modulations: Amplitude Modulation (AM), Fast-Scan (FS) and Phase Modulation (PM). The OPD variation along the time for the three options is shown in Fig 3.5. Many fast-scanning FTSs are built so that the ZPD position lies close to one edge of the moving stage path, in order to maximize the dynamic range of OPD and consequently the spectral resolution. Anyway, since one-sided interferograms transform to real spectra, no information on the phase is available, although phase problems do show up as baseline anomalies. Two-sided interferograms, on the contrary, transform to complex spectra (they have two pieces of information per frequency), allowing phase errors to be directly measured as a function of frequency. This allows to check for optical mis-alignments and other potential instrumental problems through the level of asymmetry in the two sides of the interferograms. Since a high spectral resolution is not compelling when measuring the continuum level of the atmospheric emission, CASPER2 adopts a two-sided interferogram sampling, with the ZPD located half-way along the moving mirror path. To reduce the effect of measuring the interferograms with a limited mechanical path difference, the interferogram lobes are weighted with a triangular apodization function, at the expense of decreasing the spectral resolution to about 8.6 GHz [44].

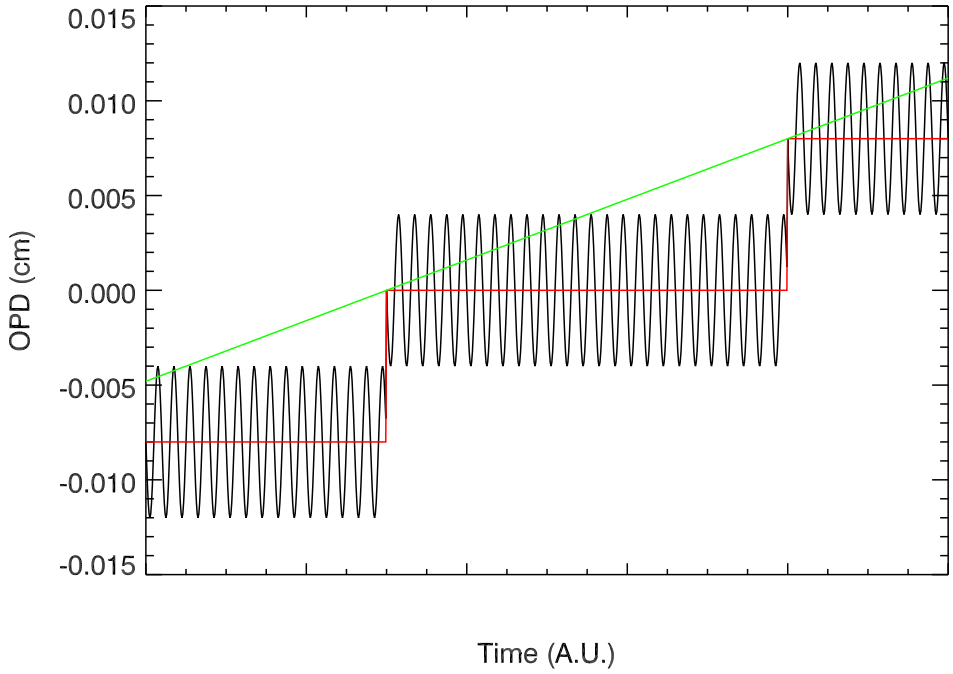

Figure 3.5. Comparison of variation of OPD along the time for FS (green line), AM (red line) and PM (black line) modulation techniques.

3.3.1 Amplitude Modulation

The amplitude modulation (AM) technique is fulfilled by a chopper wheel modulator placed in front of the cryostat, performing a synchronous demodulation of the signal, and a step-by-step movement of $RM1$. The signal from the detector is sent to a referenced to the same modulation frequency. The lock-in amplifier returns only the component of the detectors signal whose frequency is exactly equal to the reference one. In this way the noise fraction outside of the modulation frequency range is removed and the Signal to Noise Ratio (SNR) is optimized. In the stepped-scan interferometers, the movable mirror is held stationary at each sampling and then moved rapidly to the next sampling position. The interferogram signal is produced by integrating the detector output signal during the time interval that the mirror is held stationary. The lock-in time constant, during which the temporal average of the input signal and the reference wave is performed, has to be greater then the detectors time constant and at the same time shorter then the source variations time-scale, cause the lock- in needs some time constants to reproduce these variations to the output. The time interval during which the mirror is stepped from one sampling position to the next is lost time that does not contribute to the observation and therefore should be kept short relative to the integration period.
The step length is equal to $100\mu m$ ensuring a Nyquist frequency, $\nu_N = 750$ GHz, higher than 450 GHz, see Table 3.2. Even though the choice of shorter steps doesn't cause the lost of spectral data, it brings anyway to a longer measurement time. The chopper blades, covered by Eccosorb AN72, act as reference source at ambient

temperature. The two modulated signals feed the two lock-in amplifiers. Since the chopper is kept at room temperature, the large brightness temperature gradient between the 2 sources implies that the faint signal fluctuations are difficult to detect. In addition the *AM* procedure has the disadvantage that half observation time is spent on the reference source. The *AM* procedure represents a reliable tool useful to characterize the performance of the whole instrument, working both with stable sources in laboratory tests and instrument calibration over bright sky signals.

3.3.2 Fast-Scan

The fast-scan technique consists in sweeping the range of available OPDs through a rapid movement of the translating stage at constant velocity. The recorded time-domain signal is therefore trivially related to the interference pattern thanks to a simple time/position conversion through the stage velocity, and the Fourier analysis yields directly the needed information about the spectrum of the incoming radiation beam. A properly set velocity may shift the electrical frequencies of interest away from potentially troublesome low-frequency components or line features in system noise, allowing for a cleaner reconstruction of the optical power in the passband. Moreover, since the scan can be repeated an arbitrary number of times, the short integration time per unit OPD can be increased to hit the photon noise limit with almost no additional effort in the instrument setup. On the other hand, apart from mechanical limitations, an intrinsic upper limit to the value of the translation velocity is determined by the time constant of the detectors and by the highest frequency in the instrument bandwidth: in order to be able to discriminate two consecutive fringes in the interference pattern generated by radiation at frequency ν_{max}, they must be scanned in a time interval longer than the detector time constant τ_d, thus determining the limit velocity

$$v_{lim} \leq \frac{1}{\tau_d \nu_{max}} \tag{3.15}$$

Fast scanning interferometers are usually operated well below this limit, and signals are de-convolved from the detector time-response before further data-processing to avoid residual artifacts. This is the case also for CASPER2, where the time-constant of the detectors is τ_d=10 ms and the translation velocity of the moving roof mirror is set to 0.86 cm s^{-1} (*i.e.* 1.72 cm-1 lag velocity). Under these conditions, a time of 3.8 s is needed to perform one scan. An average of several scans on the same source is needed to improve the signal to noise ratio of the observation (see Sec. 3.5).
A critical source of systematics in fast-scanning FTSs is the non-uniformity of the scan velocity: since interferograms need to be uniformly sampled in space-domain, rather than in time-domain, any fluctuation in velocity at a fixed scan rate converts into a local "stretch" of the OPD scale, resulting into artifacts in the frequency domain, both in line and continuum interferometry. In CASPER2, this issue is solved by monitoring the stage position through the optical sub-interferometer (see Sec. 3.2.2), whose fringes provide a position reference for each data-point. The interferograms are highly oversampled (5 kSamples s^{-1}), with an electrical Nyquist frequency of 2.5 kHz (or an equivalent optical bandwidth of 43.6 THz). After Fourier transfor-

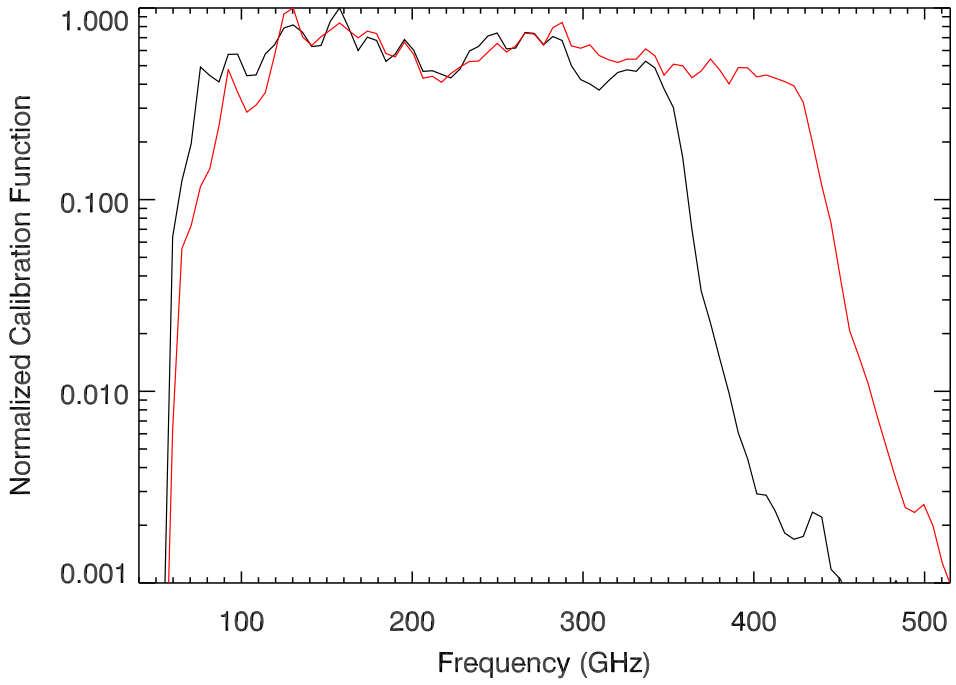

Figure 3.6. The normalized calibration function for CH1 (black line) and for CH2 (red line).

mation, the high frequency components of instrument noise are discarded and the signal in the optically meaningful band is processed to extract the sky brightness and *pwv* information. One of the advantages of fast scan interferometry over step by step interferometry (or slow scan) is that no chopper is used to modulate the radiation (see Sec. 3.3.1). A disadvantage in FS interferograms is that slow drifts in the intensity of the source can result in variations of the baseline of the interferogram which can be of the same frequency as modulations from the longest wavelength being measured. This affects the performance at low optical frequencies.

3.3.3 Phase Modulation

A third signal modulation technique, available with CASPER2, is the Phase Modulation (PM). This technique allows to replace AM and FS implying a modulation of the OPD when recording the interferogram [19]. The insensitivity to slow fluctuations in the intensity of the source plus the full time on source observations, make PM very attractive to atmospheric measurements.
Operatively the modulation is performed by periodically wobbling $RM2$ while the detector signals are lock-in demodulated. The Muller matrix for the MPI can be rewrote, as in Eq.3.6 :

$$M_{MPI} = \begin{pmatrix} 1 & 0 & 0 & 0 \\ 0 & \cos\delta^{'} & 0 & \sin\delta^{'} \\ 0 & 0 & -1 & 0 \\ 0 & \sin\delta^{'} & 0 & -\cos\delta^{'} \end{pmatrix} \tag{3.16}$$

where $\delta^{'} = \delta + \delta_M$ with $\delta_M = 2\pi M(t)/\lambda$, the modulation of the OPD obtained by periodically oscillating $RM2$ with an amplitude A and a frequency ν_0. In Figure 3.5 the OPD along the time is plotted for all the three observation modes. The resulting interferogram is proportional to the derivative of the original one multiplied for the modulation amplitude. The Fourier transform of the "classic" interferogram yields frequency spectrum of the incident radiation. It can be shown, [19, 20], that the Fourier transform of the PM interferogram, $f(x)$, is linked with the original one by means of the following relation:

$$F[f^{'}(x)](k) = C_0|2J_1(2\pi\sigma A/2)|F[f(x)](k) \tag{3.17}$$

where J_1 is the Bessel function of the first kind with σ the wavenumber [CHECK] and A the modulation amplitude and C_0 is the first term of Fourier series dependent on the wobbling function $M(t)$.
The amplitude modulation has to be carefully chosen to fit the spectral band of the instrument. In our case, with a sinusoidal modulation function, $A = 0.58c/\nu_{max}$ that for $\nu_{max} = 450$ GHz, the highest frequency in the two bands, corresponds to 840 μm.
The wobbling frequency is chosen equal to 12 Hz so the effect of low frequency source variations is essentially eliminated using PM techniques. At the same time, avoiding a *dc* component the acquisition dynamic range is well fitted to the interferogram range. $RM2$ is wobbled by a linear actuator driven by a waveform generator using a feedback loop based on a position transducer and a Proportional-Integral-Derivative circuit. A linear variable differential transformer *(LVDT)* (Solartron Metrology, model SM/1) is used as position transducer for the mirror. The accuracy in oscillation amplitude and frequency has been checked and resulted to be 2% in amplitude and 1% in frequency.
The requirements on stability of the oscillation amplitude have been estimated by simulated observations. Changes in the amplitude result in a different weighting along the spectrum affecting the inferred *pwv*, as derived by fit of ATM synthetic spectra. The constraint on *pwv* respecting the uncertainty on the $RM2$ oscillation amplitude turns out to be 2%, estimated assuming several *pwv* average values in the range 0.1 mm to 6 mm.

3.4 Calibration procedures

Calibrated spectra are derived employing several considerations. The two inputs of CASPER2 differ as follows:

$$B_{in_1}(\nu) = \epsilon_{atm}(\nu)BB(T_{atm},\nu) + \epsilon_{tele}(\nu)BB(T_{tele},\nu) \tag{3.18}$$

$$B_{in_2}(\nu) = BB(T_{ref}, \nu) \tag{3.19}$$

where ϵ_{atm} and ϵ_{tele} are the atmospheric and telescope emissivities respectively while BB stands for the specific brightness of the atmosphere, the telescope and the reference load (the only one having an emissivity equal to 1), each of them at the equivalent temperatures T_{atm}, T_{tele} and T_{ref}. While ϵ_{atm} is related to the atmospheric opacity, we assume ϵ_{tele} equal to 0.03 at the frequency of 150 GHz, for an aluminum mirror, and changing with the frequency as $\sqrt{\nu}$.
The spectra derived from Eqs. 3.8 and 3.9, after baselines removal, are related to the spectra of the incoming sources as:

$$\begin{aligned} \tilde{I}_{out_1}(\nu) &= R_1(\nu)\varepsilon_1(\nu)A\Omega(\nu)\left[B_{in_1}(\nu) - B_{in_2}(\nu)\right] = \\ &= F_1(\nu)\left[B_{in_1}(\nu) - B_{in_2}(\nu)\right] \end{aligned} \tag{3.20}$$

$$\begin{aligned} \tilde{I}_{out_2}(\nu) &= R_2(\nu)\varepsilon_2(\nu)A\Omega(\nu)\left[B_{in_2}(\nu) - B_{in_1}(\nu)\right] = \\ &= F_2(\nu)\left[B_{in_2}(\nu) - B_{in_1}(\nu)\right] \end{aligned} \tag{3.21}$$

The calibration function, $F_i(\nu)$, for the i-channel includes the responsivity $R_i(\nu)$, the spectral efficiency $\varepsilon_i(\nu)$ and the throughput $A\Omega(\nu)$. In Fig. 3.6 the normalized calibration functions are shown for both channels.
The throughput $A\Omega(\nu)$ is assumed equal for the two inputs, being only dictated by the optical matching between the cones and the last cold lens operating as aperture stop. A frequency dependence of it can be considered for both patterns: starting from a single mode propagation, at the cone exit apertures at the lowest frequency, and moving to a multi mode approach at 450 GHz. For CASPER2's application this anisotropic response of the two ports is not a technical hitch due to the presence of diffuse sources, the atmosphere and the sheet of Eccosorb, totally filling both the inputs. The telescope efficiency can be easily assumed unitary along the whole spectral range [95] counting on a $r.m.s.$ surfaces error of $\sim 0.1\mu m$, while the wire grids behave like ideal polarizers in our bands.
The optical matching between the MPI and the two sources shows differences due to the distinct optical paths. Specifically in the case of in_1, the input port is further transformed by the primary beam telescope.
The calibration functions are estimated by filling the in_1 port with a second well modeled source, a cold black body, realized by an Eccosorb AN72 sheet thermalized inside a liquid nitrogen bath (77 K). Thereby the atmospheric spectra is deduced by:

$$I_{atm_i}(\nu) = \frac{I_{out_i}(\nu)}{F_i(\nu)} + BB(T_{ref}, \nu) - \epsilon_{tele}(\nu)BB(T_{tele}, \nu) \tag{3.22}$$

Possible optical mismatch between the two input ports has to be known and taken into account to avoid the consequent contamination on inferring the atmospheric spectra. The correct balancing between the two inputs is checked by filling also the sky port with a room temperature blackbody inserting an Eccosorb AN72

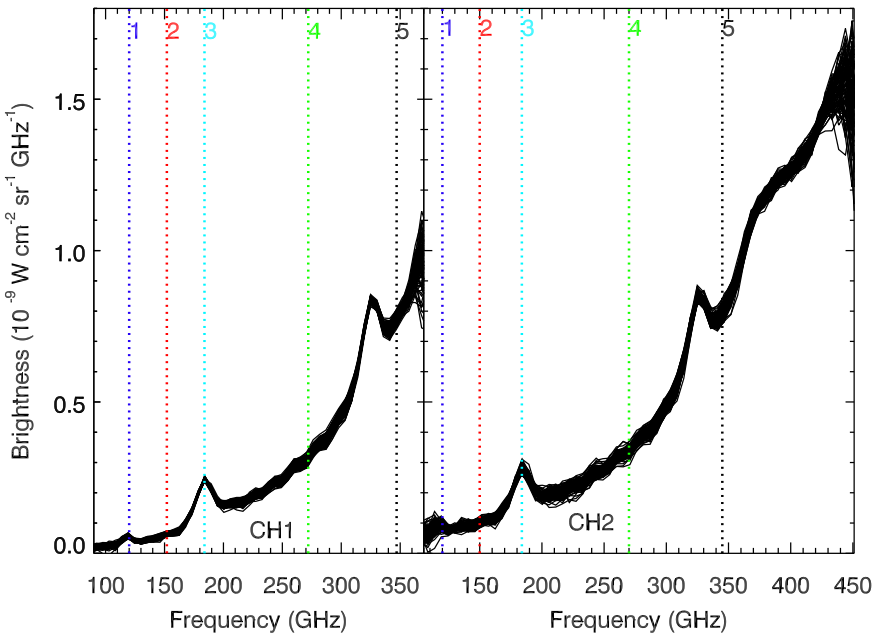

Figure 3.7. Overplotted atmospheric zenithal spectra recorded at MITO on July 16th 2010, started at 04:03 AM and stopped at 04:12 AM. The vertical dotted lines denote the fiducial frequencies, defined in the text, where the Allan variance has been estimated.

sheet in front of the telescope to record a *null* interferogram. Only in this case a residual signal could arise in the acquired spectrum when an unideal source coupling of the two input ports is present. A potential temperature gap between the two blackbodies could also produce a non-*null* interferogram but this instead has been monitored.
The knowledge of the *null* interferogram, or at least the upper limit of the ZPD value when the signal-to-noise ratio is less then one, allows us to put a constraint on the minimum detectable contribution on the *pwv* content. Long acquisition of *null* interferograms let us to discriminate spectra having a difference of only 0.01 mm of *pwv* irrespective of the *pwv* content, at least for $pwv < 1$ mm.

3.5 The Allan Variance

The instability of the atmosphere emission in the mm/sub-mm spectral region has to be carefully taken into account when the observational goal is to achieve frequent and independent high signal-to-noise ratio spectra. The time dedicated to perform a single interferogram is mainly dictated by the detector time response while the timescale to average several interferograms is affected by the atmospheric drifts. In the specific case of FS technique, to avoid loss of observational time, the minimum number of spectra that can be averaged to achieve an high signal-to-noise ratio and allowing a sampling of atmosphere status while it changes, has to be constrained.

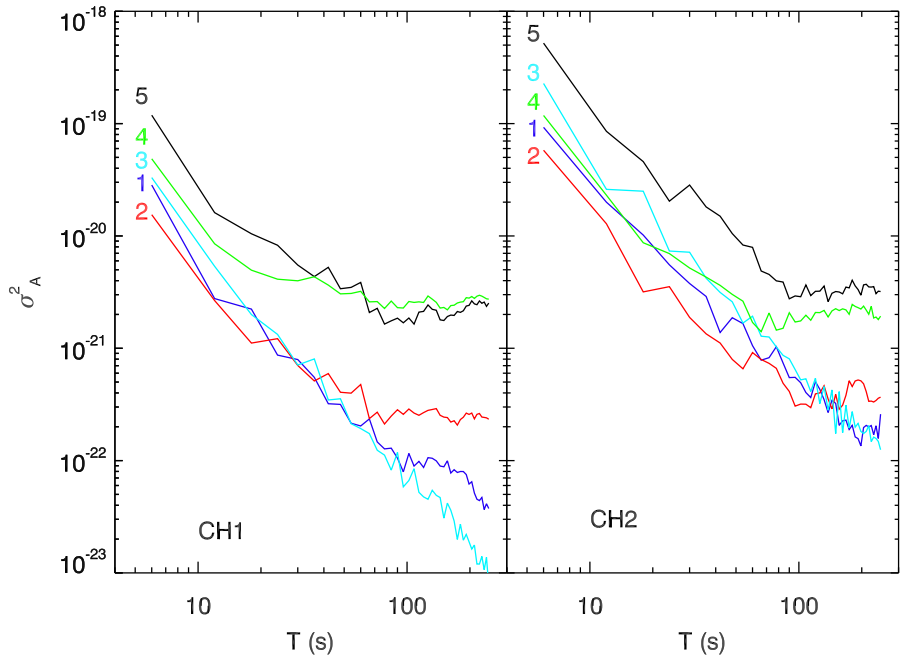

Figure 3.8. Allan variance estimated at the 4 fiducial frequencies labeled and colored as in Fig. 2.18

It is fundamental to determine a characteristic time to discriminate when an instrument is dominated only by thermal noise from an atmosphere fluctuations regime. An appropriate approach to infer this timescale is to estimate the Allan variance [2]. In a wide band spectrometer, like CASPER2, it is important to check also the timescale similarity for all the frequencies by investigating the noise performance in the measured spectra [97].
Large fluctuations of atmosphere emission are expected in correspondence with the 3 "windows" centered at the frequencies of 150, 270 and 350 GHz; hereafter we refer to these lines with **2**, **4** and **5**, respectively. On the contrary the oxygen band at 118 GHz and the high absorption H_2O band at 183 GHz, quoted as **1** and **3**, should appear more stable in time. In Fig. 3.7, as example, 87 spectra of the zenithal atmospheric brightness recorded by FS technique are shown for the 2 bands of CASPER2. Each spectra is the average of a couple of back-and-forth spectra acquired in 6 seconds. The vertical dotted lines are referring to the examined frequencies.
The Allan variance is calculated, for the previous 5 reference lines, in the following way. The signal, $s_f(t_i)$, related to the atmosphere emission at the frequency f extracted by the FS spectra at time t_i, is averaged over variable timescales, T, generating the new dataset:

$$S_f(T, t_j) = \frac{1}{T} \sum_{i=j+1}^{j+T} s_f(t_i) \tag{3.23}$$

The Allan variance, or the two-sample variance, is estimated for the frequency f as in [125]:

$$\sigma_A^2(T) = \frac{1}{N-2}\sum_{j=2}^{N-1}\left(\frac{S_f(T,t_{j-1}) + S_f(T,t_{j+1})}{2} - S_f(T,t_j)\right)^2 \tag{3.24}$$

In Fig. 3.8 the Allan variance corresponding to the 5 frequencies is plotted in the cases of the two CASPER2 bands. It is worthy to note the expected $1/T$ dependence for short average times, corresponding to dominant thermal noise, and the slope change when atmospheric drifts overcome. This behavior is not satisfied in the case of **1** and **3**, where a strong and stable emission is present.
We can estimate, at least for this specific dataset of spectra, $T \simeq 100$ s as the more suitable average time. Even if the values of the Allan variance increase for all the frequencies in the high-background Channel 2, affected by a larger instrumental noise, the best average time is almost the same. This timescale has been employed to generate the spectra reported in the next Section.

3.6 Preliminary atmospheric spectra measurements at MITO

In this section preliminary measurements of atmospheric spectra performed during the summer campaign at MITO from 11 July to 19 July 2010 will be presented [27]. According to Eq. 3.10 and Eq. 3.11 the intensity on the detectors is made of two components: an offset or baseline and a component that is modulated as a function of the opthical path difference. One of the methods that may be employed to evaluate the interferogram baseline is to fit each of the derived interferograms sidelobes with a polynomial fitting (generally a first order function of the o.p.d. is more than sufficient). After the non-zero offset is evaluated and removed, all the interferograms have all been multiplied by a triangular apodization function centered at the z.p.d position, in order to remove the spectral artifacts at the sidelobes. The apodization function application produces a little reduction of the observed spectral resolution, as discussed in Sec. 3.3. The interferograms performed with FS, PM and AM procedures for the two channels of CASPER2 at MITO are shown in Figs. 3.9 3.10 and 3.11.
The spectral reconstruction is performed with the Fast Fourier Transform (FFT) procedure of IDL (Interactive Data Language) code on the measured interferograms. Atmospheric spectra measured by the two channels of CASPER2 with fast scan procedure on July 16th 2010 are shown in Figs. 3.12. The uncertainty associated to the data points is given by the standard deviation of the dataset and it is closely connected to the time on which the interferograms average is performed (see Fig. 3.8). Best fit ATM model corresponds to *pwv*= 6.64 ± 0.17 mm for CH1 and *pwv*=7.00 ± 0.17 mm for CH2 (red lines in Fig. 3.12). The uncertainty on the *pwv* value has been evaluated by a random generation of the ATM synthetic spectra within the brightness uncertainty range and it corresponds to less then 3 per cent.
In the same way spectra recorded by the two channels of CASPER2 on July 16th 2010 with PM procedure are shown in Figs. 3.13. Best fit ATM model corresponds to *pwv*= 7.00 ± 0.24 mm for CH1 and *pwv*= 7.41 ± 0.19 mm for CH2 (red lines in

Fig. 3.13).
Finally the spectra recorded with AM procedure are shown in Fig. 3.14. Best fit ATM model corresponds to $pwv = 8.3 \pm 0.3$ mm for CH1 and $pwv = 7.7 \pm 0.6$ mm for CH2 (red lines in Fig. 3.14).
Missing of consistency between data and ATM spectra with increasing the frequency, supports the necessity to accurately calibrate the dry continuum and the H_2O pseudocontinuum terms in the simulated atmosphere [83]. The ATM model is currently based on T/P typical profiles and the validation of the code is one of the future perspectives of this analysis.
Spectra recorded during the observational campaign highlights the instrumental capabilities and will permit to validate the results of the transfer radiative ATM code for this site and consequently to infer the *pwv* value as derived by fit with synthetic spectra or by skydips.

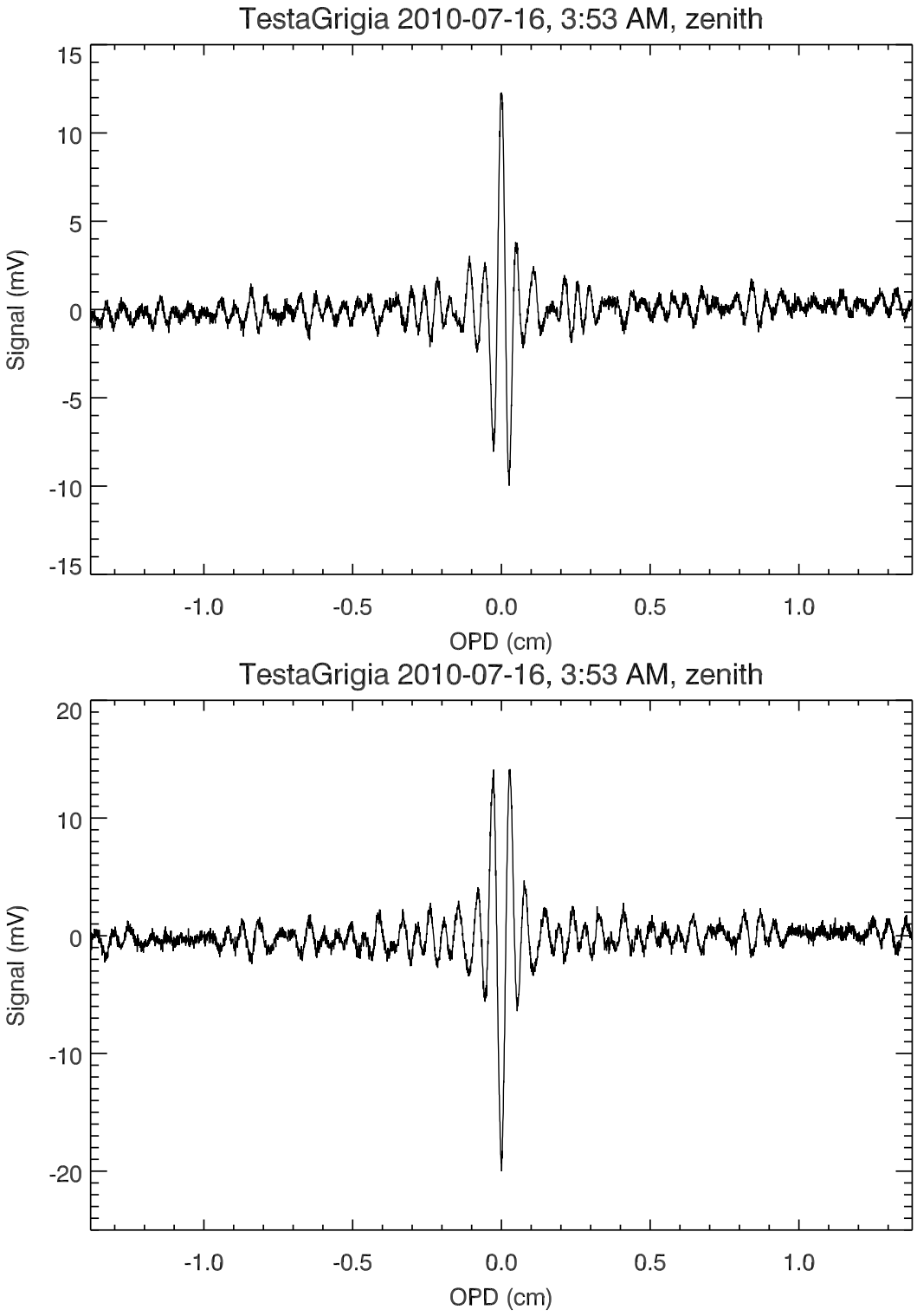

Figure 3.9. Averaged atmospheric zenithal interferograms recorded with fast scan procedure at MITO on July 16th 2010, 03:53 AM for CH1 (top panel) and CH2 (bottom panel).

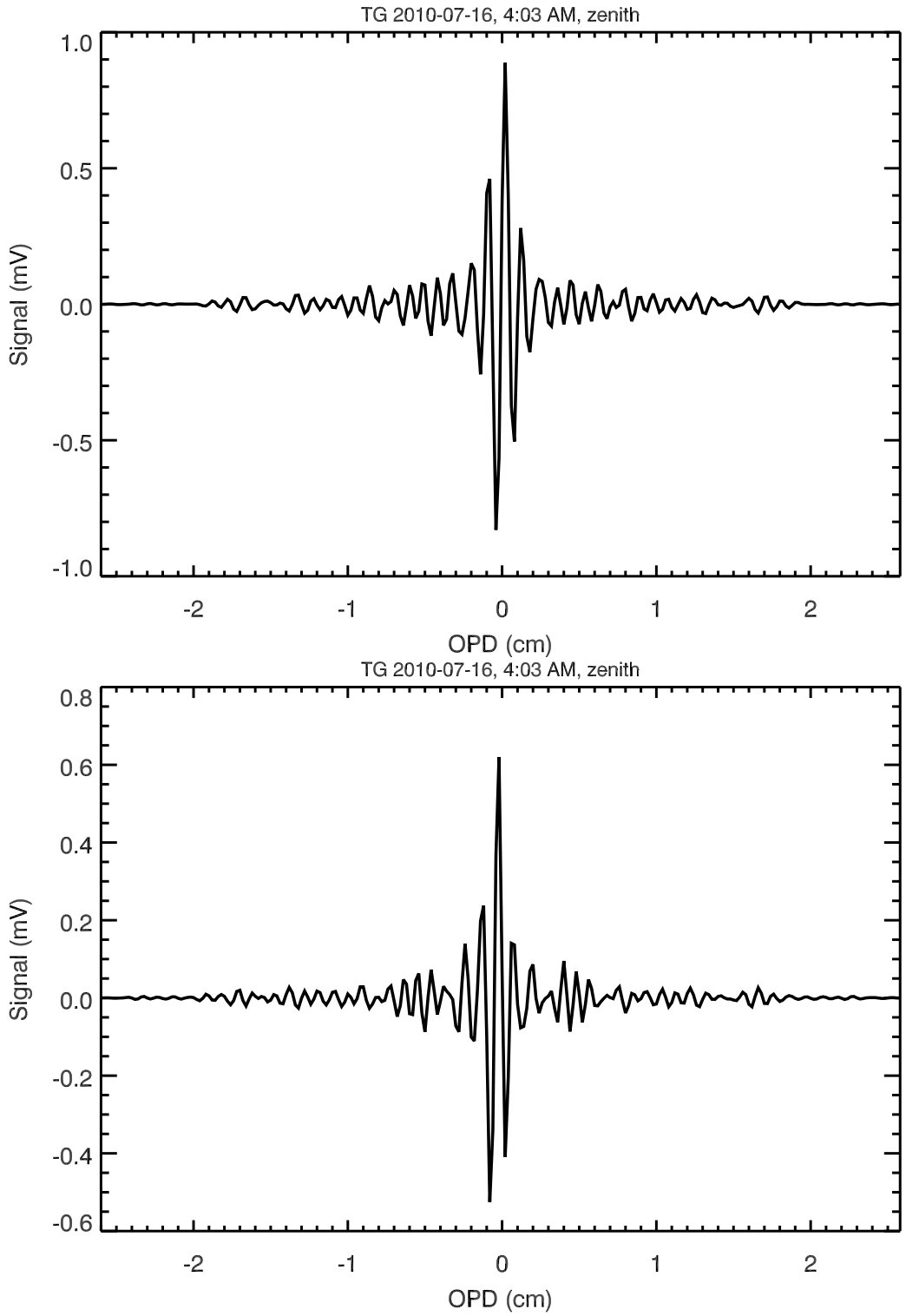

Figure 3.10. Atmospheric zenithal interferograms recorded with phase modulation procedure at MITO on July 16th 2010, 04:03 AM for CH1 (top panel) and CH2 (bottom panel).

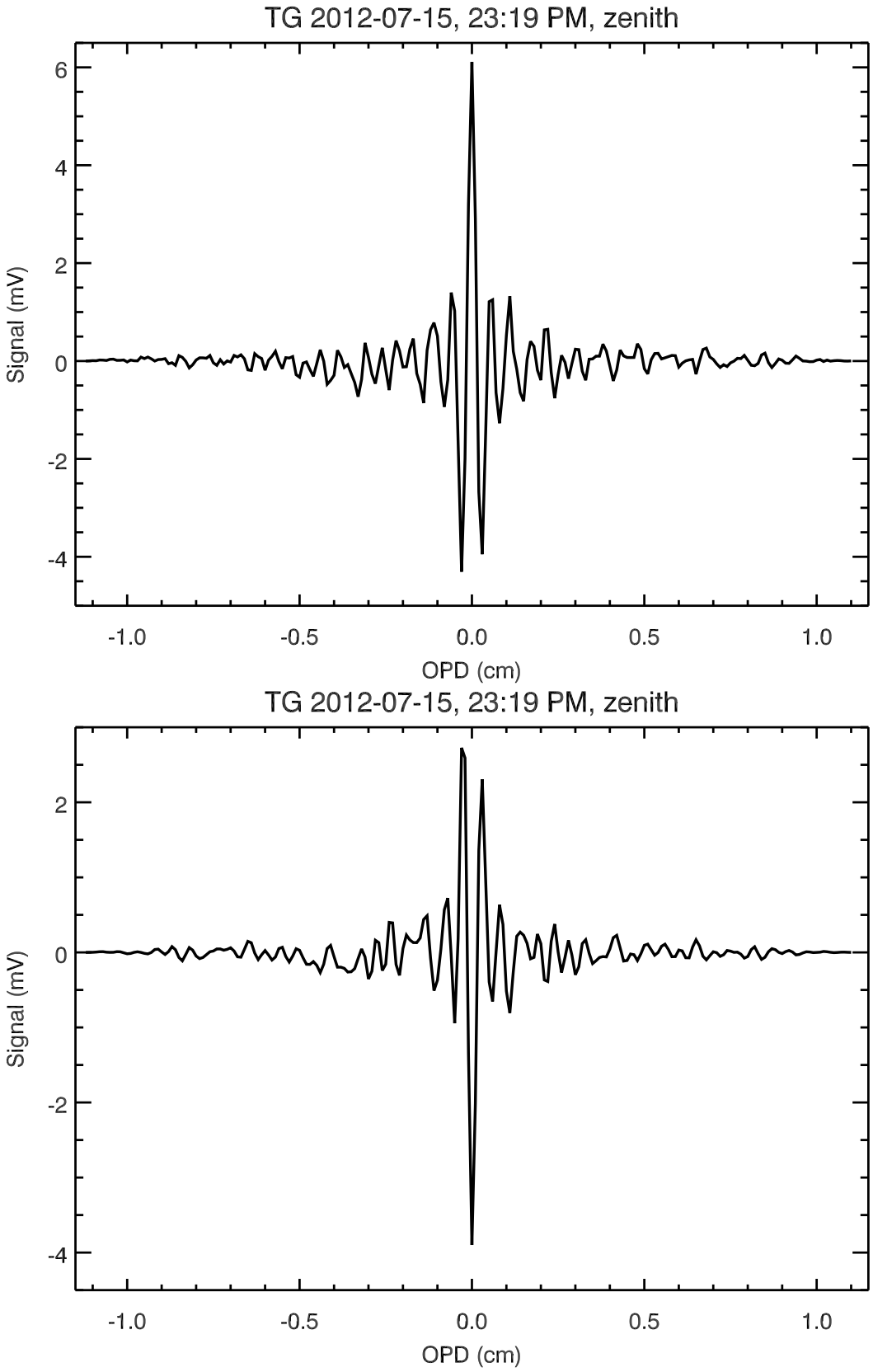

Figure 3.11. Atmospheric zenithal interferograms recorded with amplitude modulation procedure at MITO on July 15th 2010, 11:19 PM for CH1 (top panel) and CH2 (bottom panel).

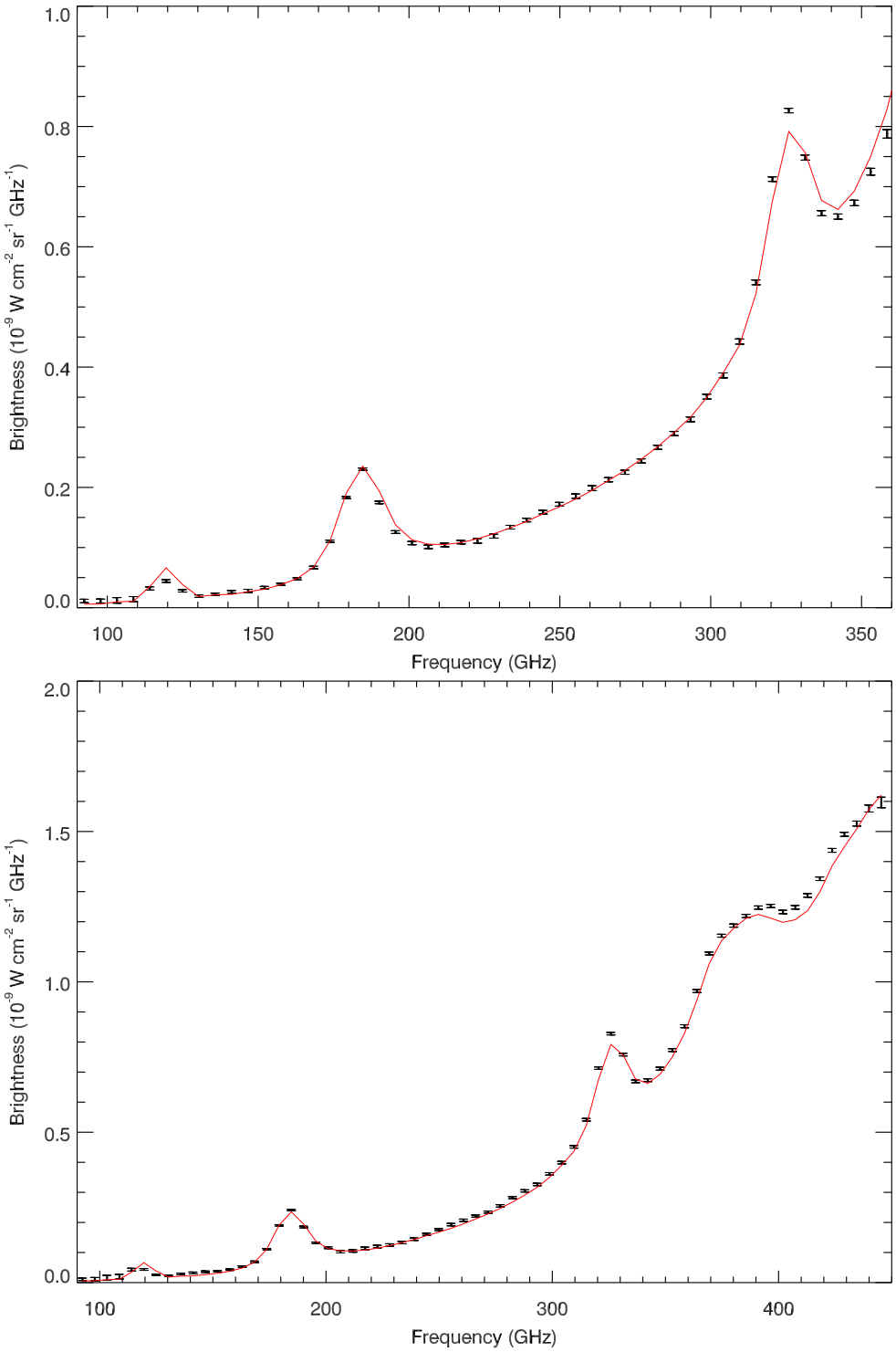

Figure 3.12. Averaged atmospheric zenithal spectra recorded with fast scan procedure at MITO on July 16th 2010, 03:53 AM. The red line is the best fit obtained with ATM model corresponding to $pwv = 6.53 \pm 0{,}16$ for CH1 (top panel) and $pwv = 6.84 \pm 0.16$ mm for CH2 (bottom panel).

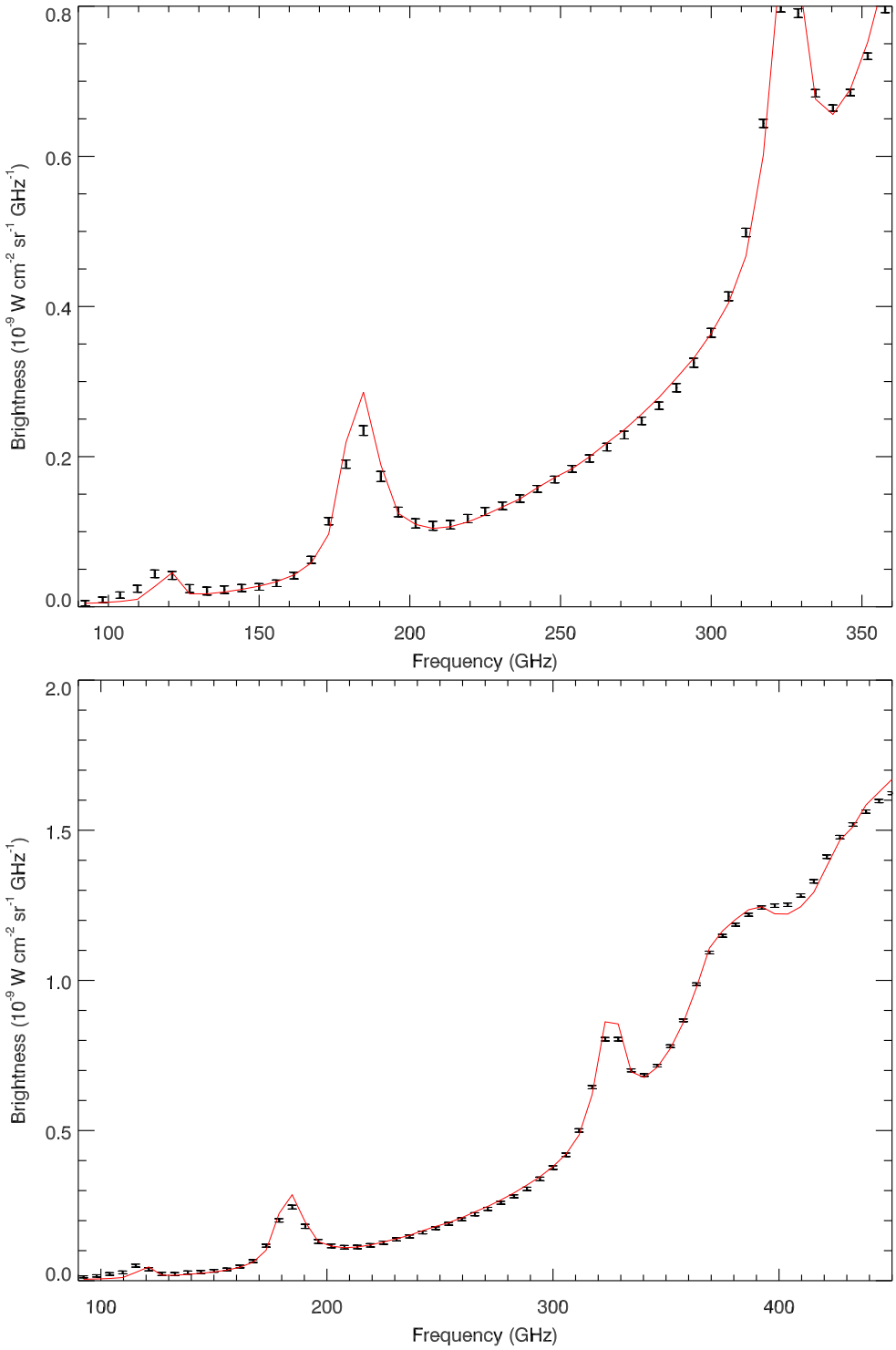

Figure 3.13. Atmospheric zenithal spectra recorded with phase modulation procedure at MITO on July 16th 2010, 04:03 AM. The red line is the best fit obtained with ATM model corresponding to $pwv = 7.00 \pm 0.24$ mm for CH1 (top panel) and $pwv = 7.41 \pm 0.19$ mm for CH2 (bottom panel).

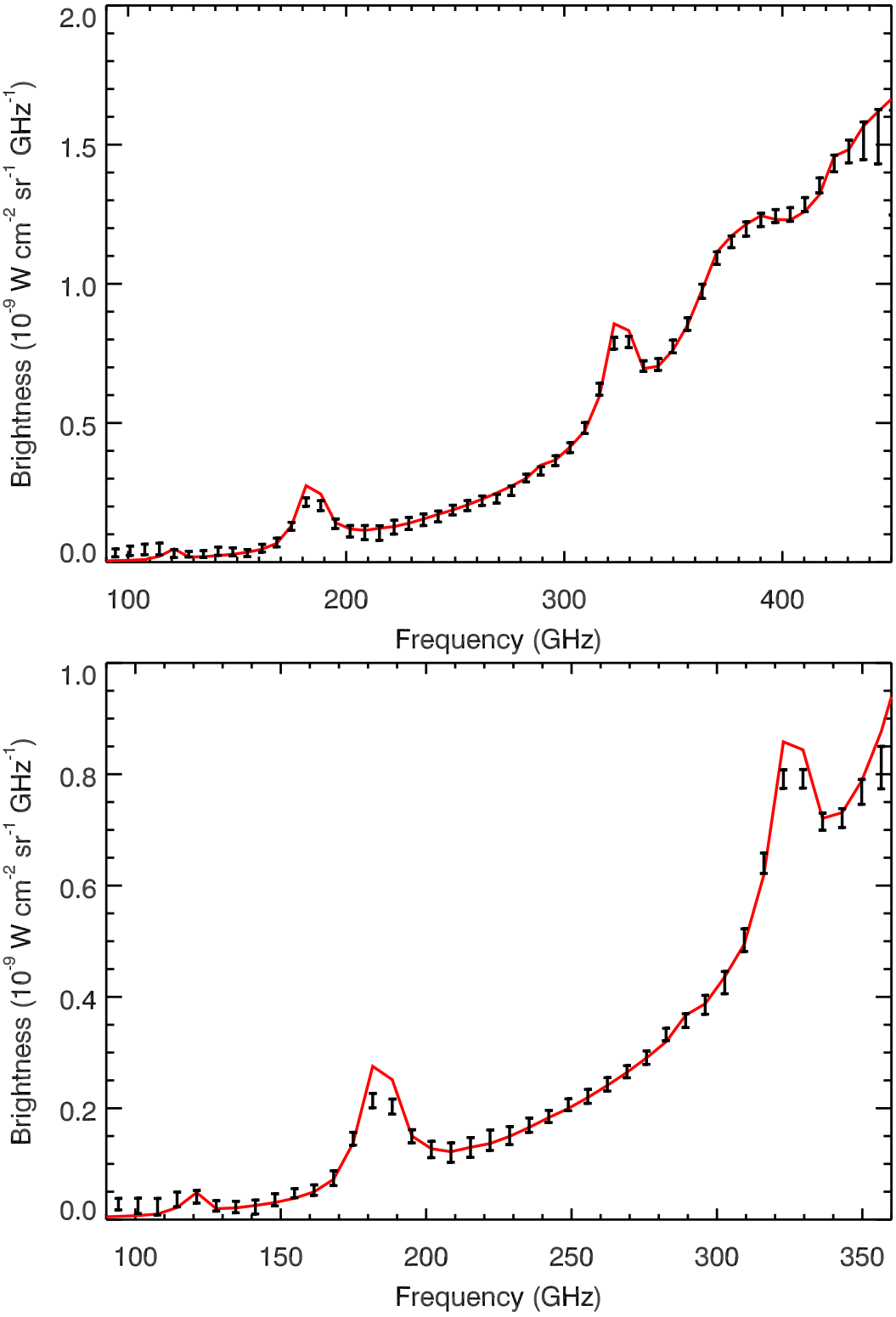

Figure 3.14. Atmospheric zenithal spectra recorded with amplitude modulation procedure at MITO on July 15th 2010, 11:19 PM. The red line is the best fit obtained with ATM model corresponding to $pwv = 8.3 \pm 0.3$ mm for CH1 (top panel) and $pwv = 7.7 \pm 0.6$ mm for CH2 (bottom panel).

Chapter 4

FPI at millimeter wavelengths

Three spectrometer designs have been considered to provide MAD experiment with spectroscopic capabilities: a grating spectrometer, a cooled Fabry-Perot Interferometer (FPI) and an external Fourier Transform Spectrometer (FTS). The grating spectrometer solution is characterized by low throughput and large size but with fixed elements, *i.e.* low mechanical complexity. Having only one spatial dimension available on the array, being the second one employed in the spectral elements separation, it is unsuitable for an imaging instrument. On the other hand a FTS provides high throughput, variable resolution with imaging capabilities too. Anyway the total power falling onto the detectors may create an unacceptable photon noise level in the presence of high emission foregrounds, especially in the case of ground-based measurements strongly affected by atmospheric emission fluctuations, even in a differential configuration. The FPI provides high throughput and intermediate or high resolution imaging spectroscopy, depending on the reflectivity of the plates. However the most important advantage for our interest is that the FPI limits the photon background and the photon noise on the detectors, making the FPI the best configuration to improve MAD capabilities (see Sec. 1.3).
The FPI acts as an optical filter operating by multiple-beam interference of reflected rays of light. The theory of this interferometer will be briefly presented in Sec. 4.1, while practical limitations on the performance are considered in Sec. 4.1.1. The requirement for high reflectivity coupled with low absorption loss at microwave wavelengths is met by metallic meshes employed as reflective surfaces of the resonant cavity [117]. The performance of a millimetric FPI made of two metal meshes are then discussed in Sec. 4.2. Finally a preliminary study of the information that can potentially be extracted by MAD + FP measurements is described in Sec. 4.3.

4.1 FPI theory

The FPI is composed of two parallel surfaces partially reflective in a resonance cavity configuration. The transmission profile of an ideal FPI composed by two infinite and identical extent plates, illuminated with a monochromatic plane wave at normal incidence is known as the Airy function [37]:

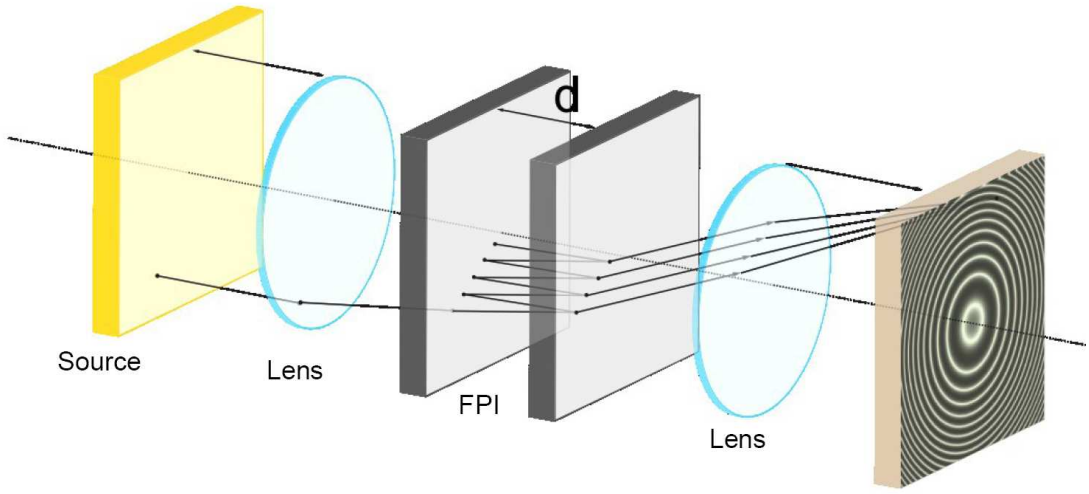

Figure 4.1. The optical configuration of a FPI composed by two partially reflective parallel surfaces at distance d.

$$T = \frac{1}{1 + Fsin^2(\frac{\phi_{tot}}{2})} \tag{4.1}$$

where the phase shift ϕ_{tot} is given by two terms, the first due to the round-trip between the two mirrors at distance d and the second due to the phase shift on reflection ϕ_r:

$$\phi_{tot} = \frac{4\pi d}{\lambda} - 2\phi_r \tag{4.2}$$

λ is the wavelength of the incoming radiation.

F is the $Finesse$ parameter, describing the efficiency of the resonant cavity. In the ideal case F is expressed only in terms of the reflection coefficient of the two mirrors R:

$$F = \frac{\pi\sqrt{R}}{1 - R} \tag{4.3}$$

but the total finesse which may be achieved by a practical device is limited by several factors (see Sec. 4.1.1). According to Eq. 4.1 the interference peaks are achieved when ϕ_{tot} is a multiple integer of π:

$$\frac{\phi_{tot}}{2} = N\pi \tag{4.4}$$

N is the interference order. In this formulation the first order corresponds to $N = 0$.

Combining Eq. 4.2 with Eq. 4.4 a relation between the distance d and the wavelength λ can be obtained:

$$\lambda = \frac{2d}{N + \frac{\phi_r}{\pi}} \tag{4.5}$$

For an interferometer consisting only of two ideal mirrors $\phi_r = \pi$ and the maxima of transmission occur when:

$$\lambda = \frac{2d}{N+1} = \frac{2d}{m} \tag{4.6}$$

The last equation is the well-known FPI interference condition, expressed in terms of the interference order $m = N + 1$ (see Eq. 4.4). Note that in most of the derivations found in literature, only the magnitude of the reflectivity is considered and not the phase shift on reflection [8]. In Eq. 4.6 the first order corresponds to $m = 1$ only due to the assumption $\phi_r = \pi$. If the cavity plates have a frequency-dependent phase shift on reflection, the more general expression of the resonance wavelength in Eq. 4.5 has to be employed instead of the well-known resonance condition in Eq. 4.6.
Eq. 4.1 means that we can use the FPI as an optical filter to selectively choose which wavelength λ of the incoming radiation will be transmitted, just by setting the mirror spacing d. The periodic nature of the FPI is expressed by the *Free Spectral Range* (FSR) parameter, defined as the spectral distance between two consecutive interference orders corresponding to the same wavelength:

$$FSR = \frac{1}{2d} \tag{4.7}$$

From Eq. 4.1 and Eq. 4.3, it is evident that the bandwidth of the transmitted light depends strongly on the reflectivity. For instance, if the reflectivity decreases from 0.90 to 0.85 (corresponding to 5 per cent), the bandwidth increases from 3 per cent to 5.2 per cent (corresponding to 58 per cent).
The ideal instrument resolution is determined only by the $Finesse$ parameter, being the resolution power equal to mF. In Fig. 4.2 the ideal Airy profile of a scanning FPI is shown. The $Finesse$ has been chosen equal to 60, in order to have 10 well-defined spectral elements in the 6-10 cm^{-1} (180-300 GHz) range. The first-order transmission maxima are obtained scanning the mirrors separation from 0.5 mm to 0.8 mm.

4.1.1 Practical limitations

All practical FPI have defects which affect the fringes width ideally achievable. The reflectivity finesse F defined in the Eq. 4.3 is only the upper limit on the real finesse which may be achieved in practice. The total finesse F_T can be expressed as follows [5]:

$$F_T = \left(\frac{1}{F^2} + \frac{1}{F_\theta^2} + \frac{1}{F_P^2} + \frac{1}{F_S^2} \right)^{-\frac{1}{2}} \tag{4.8}$$

1. The aperture finesse, $F_\theta \approx 2/(m\theta)$, is related to the finite range of angles of incidence θ passing through the instrument as well as to the order of interference m. Both for low values of the acceptance angle of the instrument and for lower orders, the aperture finesse becomes negligible.

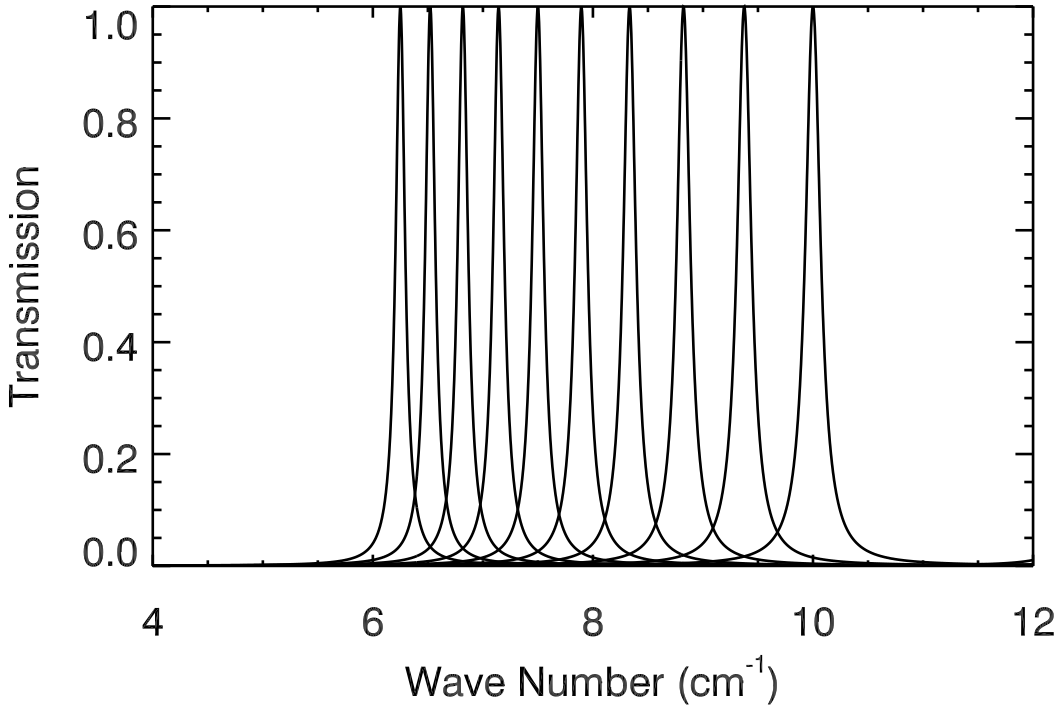

Figure 4.2. The ideal Airy profile of a FPI with $F = 60$. Spectral elements are obtained scanning the mirrors distance with ten steps among 0.5 mm and 0.8 mm.

2. The parallelism finesse F_P takes into account the lack of parallelism of the plates as well as the lack of flatness of the plate surfaces. If Δd is the the spacing variation between the two plates, the parallelism finesse can be expressed as $F_P = \lambda/(2\Delta d)$.

3. The defect finesse is given by $F_S = \lambda/(32ln2)^{1/2}\Delta s$, where Δs is the rms surface defects of the plates.

The spectral FPI transmission fringe pattern differs from an Airy distribution if the FPI mirrors deviate from parallel [88] or if the FPI is illuminated by a converging light beam [104]. The position of the peaks is determined by the joint effects of the non parallelism and the convergence/divergence of the incident beam (see Fig. 4.3). The transmission maximum position changes with the incident angle θ (see Eq. 4.6):

$$\lambda = \frac{2dcos\theta}{m} \tag{4.9}$$

A system in which light is collected through a collection angle θ_{max} has the effect of decreasing the profile height and broadening the profile as well. We can obtain an analytical expression of the FPI profile in terms of θ_{max} by integrating the Airy profile over the range of angles of incidence. As the FPI is now being illuminated with a cone of rays, a FPI fringe pattern is produced for each incident ray at angle θ. Assuming that the source radiates the same in all directions from the emitting surface, the amount of flux per solid angle (intensity) will depend on

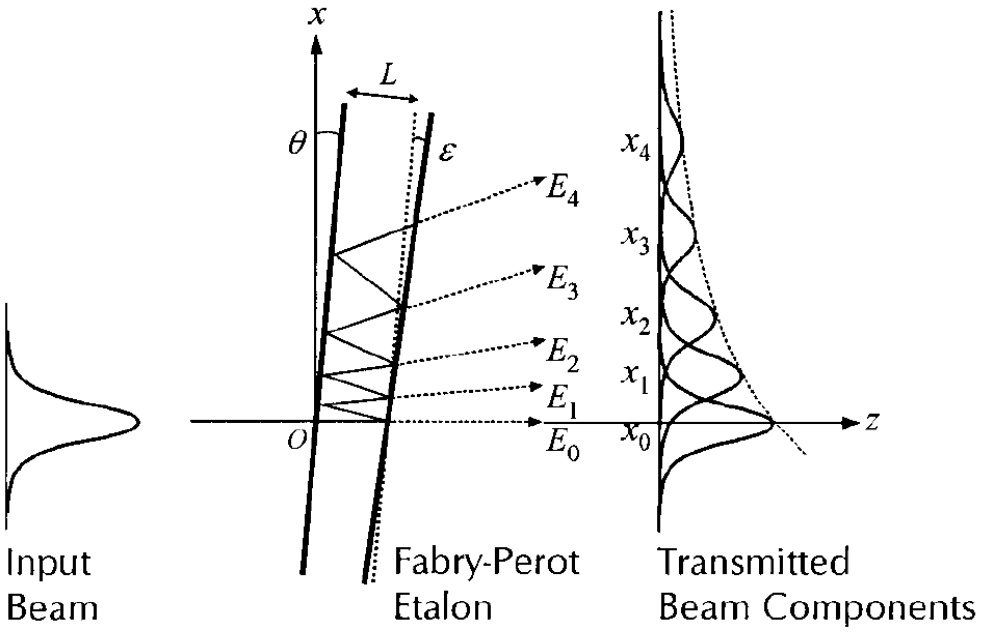

Figure 4.3. Optical geometry of a misaligned FPI: the transmitted profile shift on the x coordinate and the phase delay between adjacent outgoing beams does not remain constant (credits Lee *et al.* 2002).

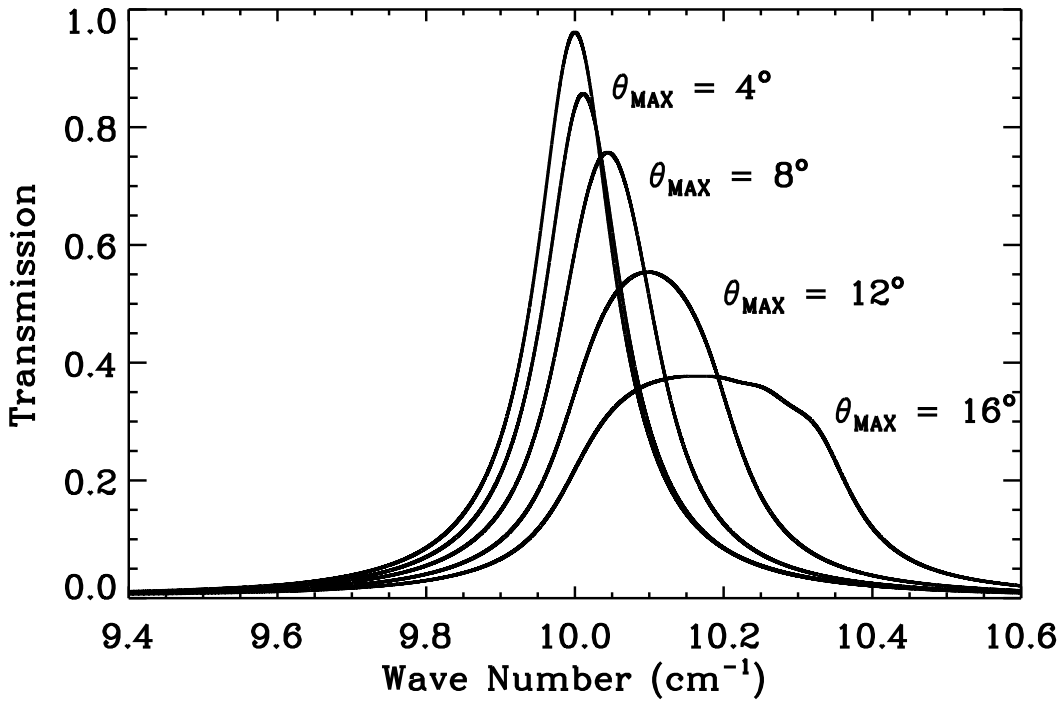

Figure 4.4. FPI fringe patterns produced by different angles of incidence.

θ [121]. Assuming a system composed only by the source and the detector, the flux filling the detector as a function of the solid angle is given by:

$$\phi \propto \int_0^{\theta_{max}} cos\theta sin\theta d\theta \tag{4.10}$$

The normalization factor for the transmitted flux can be expressed as:

$$\frac{1}{2sin^2\theta_{max}} \int_0^{\theta_{max}} cos\theta sin\theta d\theta = 1 \tag{4.11}$$

The final FPI fringe pattern is defined by the integration of the pattern produced for each angle θ multiplied by the flux correspondent to each angle [121] [58]:

$$T = \frac{1}{2sin^2\theta_{max}} \int_0^{\theta_{max}} \frac{cos\theta sin\theta d\theta}{1 + Fsin^2(2\pi md\nu cos\theta)} \tag{4.12}$$

For instance the fringe patterns produced by the same FPI of Fig. 4.2 for different angles of incidence are shown in Fig. 4.4 . The shifts of the transmission maximum towards larger wavenumbers and the decreasing of intensity becomes remarkable when $\theta_{max} > 8$ degree.

4.2 FPI at millimeter wavelengths

The two basic requirements of the reflecting elements of a practical device are high reflectivity coupled with low absorption losses. Metallic meshes are thin metal film perforated in a two-dimensional array acting as Frequency Selective Surfaces (FSS) at millimeter and sub-millimeter wavelengths: their optical behavior can be changed selecting the geometry and their parameters dimensions [117].

4.2.1 Metal meshes

Metal mesh technology is currently adopted in the mm and sub-mm ranges as the standard method for fabricating optical filters, beam-splitters, polarizers, wave-plate retarders, anti-reflection coatings and dichroics in many ground, balloon and space-based instruments [1]. Metallic meshes can be considered as circuit elements on a free space transmission line acting as inductive (square openings), capacitive (free-standing squares) and resonant (cross-shaped) elements: high pass, low pass and band-pass respectively (see Fig. 4.5) [78]. Originally inductive meshes were made of electroformed free-standing wire meshes, while the capacitive ones were obtained with thermal evaporation onto a thin dielectric using the inductive grid as a mask. In the last few years new technologies like ultra-violet photolithography on dielectric layers allow to replicate the metal patterns over large areas with excellent control of the grid geometrical properties. Freestanding filters present a high mechanical fragility so some support material with low absorption are employed as substrate (Mylar, polyamide, high-density polyethylene). Inductive and capacitive grids manifactured by the Jodrell Bank Centre for Astrophysics of The University of Manchester[1] are made of a thin dielectric substrate of Mylar (0.9-1.5 μm) or

[1] http://www.jb.man.ac.uk/

polypropylene (>3.3 μm) coated with a thin (0.1-0.4 μm) copper film. The interference filter can be formed stacking many single meshes together with plane parallel air-gaps or dielectric discs as spacers. Dielectric spacers can be fused (hot-pressed) together with the mesh sheets to make a solid disc. Absorption due to ohmic (skin effect) and dielectric losses are low but non-zero. These losses increase with frequency and decreases with temperature.
When a plane wave strikes the metal mesh at normal incidence, the E-vector forces the electrons in the metal and causes it to oscillate. Due to the fact that all the electrons are constrained to move along the wires of the grid, some electrons can not absorb energy and the wave is transmitted, while other electrons can absorb energy and the wave is not transmitted. In this second case the oscillating electron will itself radiate as an electric dipole in the plane orthogonal to the oscillation axis and this is what we refer to as the reflected wave. In general the transmission of the metal mesh is a function of wavelengths because the electrons will absorb and radiate some wavelengths with higher efficiency than others. The shape of the transmission curve depends on the geometrical pattern of the metal filter [48].
Transmission line theory can be applied to metallic meshes to understand the overall light transmission properties and also to manufacture of filters with the desired transmission properties. In the theory developed by [117] and [78] each grid is considered as one or more lumped circuit elements in a free-space transmission line to explain its optical properties. The grid period determines the wavelength at which diffraction causes grating lobes. This model works well in the non-diffraction region (when $\lambda >$ g) and for normal incidence. The grids are assumed to be thin and with infinite conductivity. In addition the supporting dielectric film is assumed to have no effect, *i.e.* no absorption.
As shown in Fig. 4.5, the shape parameters of the I-Grid and its complementary structure (C-grids) are:

- g: grid constant;
- $2a$: separation between two I-grid squares or thickness of the C-Grid wires;
- C=g-$2a$: square side;
- t: grid thickness;

Ulrich found that the resonance depends only on the dimensions of the grid and it takes place when $\lambda \approx g$ [117]. At the resonance I-grids become transparent while C-grids are totally reflective.
Geometrical parameters of R-grids are (see the bottom panel of Fig. 4.5):

- G: R-grid constant;
- L: cross width;
- C: metallic side length;
- $2a$: separation between two squares;
- $2b$: strip width;

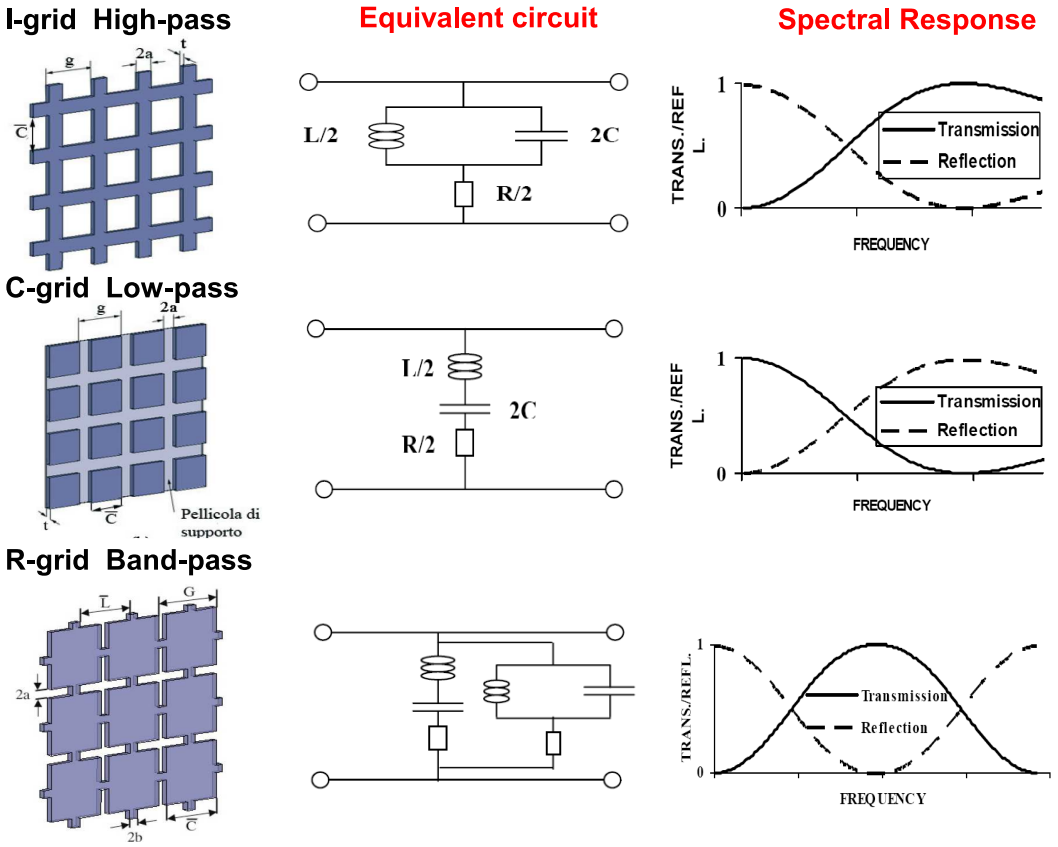

Figure 4.5. Inductive, capacitive and resonant grid transmission profiles, coupled with the corresponding geometrical patterns and their equivalent circuit.

The R-grid resonance frequency is determined by the following condition:

$$\nu_R = \frac{1}{1.5G} \tag{4.13}$$

It turns out to be lower then the diffraction limit, so this kind of meshes can be employed also at frequencies close to the resonance, without occurring in diffraction disturbs. The bandwidth can be reduced decreasing the ratio a/G and increasing the ratio b/G.

Several authors proposed new semi-empirical approaches to determine the optical response of thick meshes in the presence of a dielectric substrate. In Fig. 4.6 the transmission of an inductive grid derived with the models developed by [59], [21] and [4] are compared with [117]. When the wavelength λ becomes greater then the grid pass g, diffraction effects take place and the transmission line model becomes inapplicable. An alternative modeling approach is based on finite-element analysis software (HFSS), available commercially (see Sec. 5.3). This approach has been combined with laboratory measurements of real grid systems to make accurate predictions (see Chapter 5).

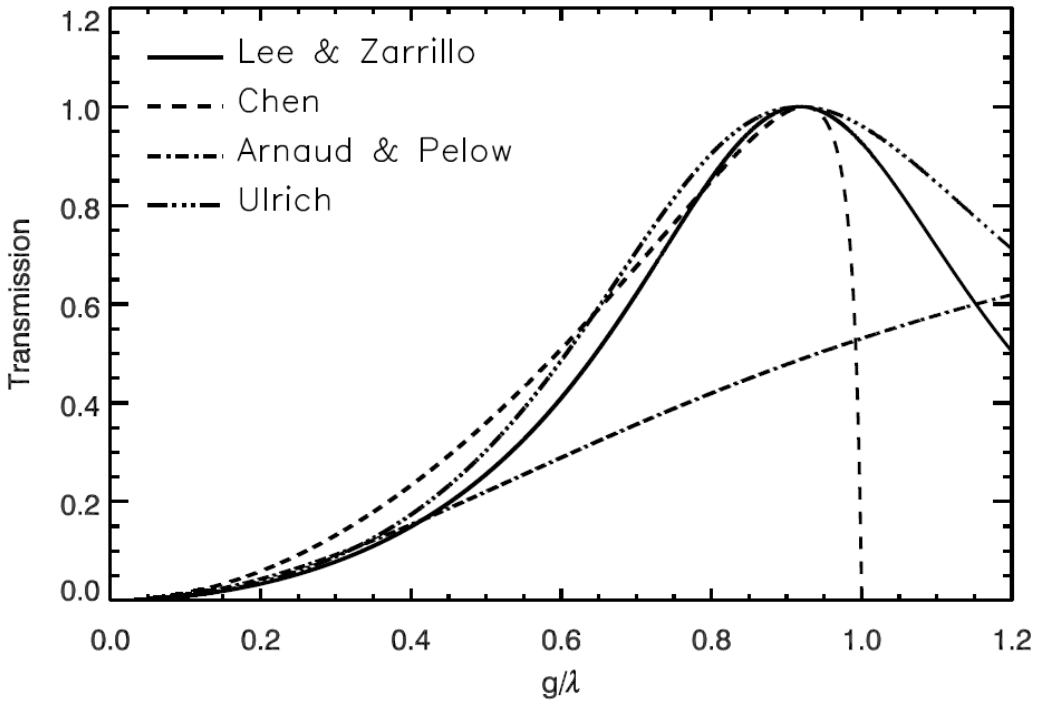

Figure 4.6. Transmission coefficient of an inductive grid illuminated by a normally incident plane wave in the free-space as a function of the ratio λ/g. The geometry of the grid is C = 0.7 g (credits D. Buzi).

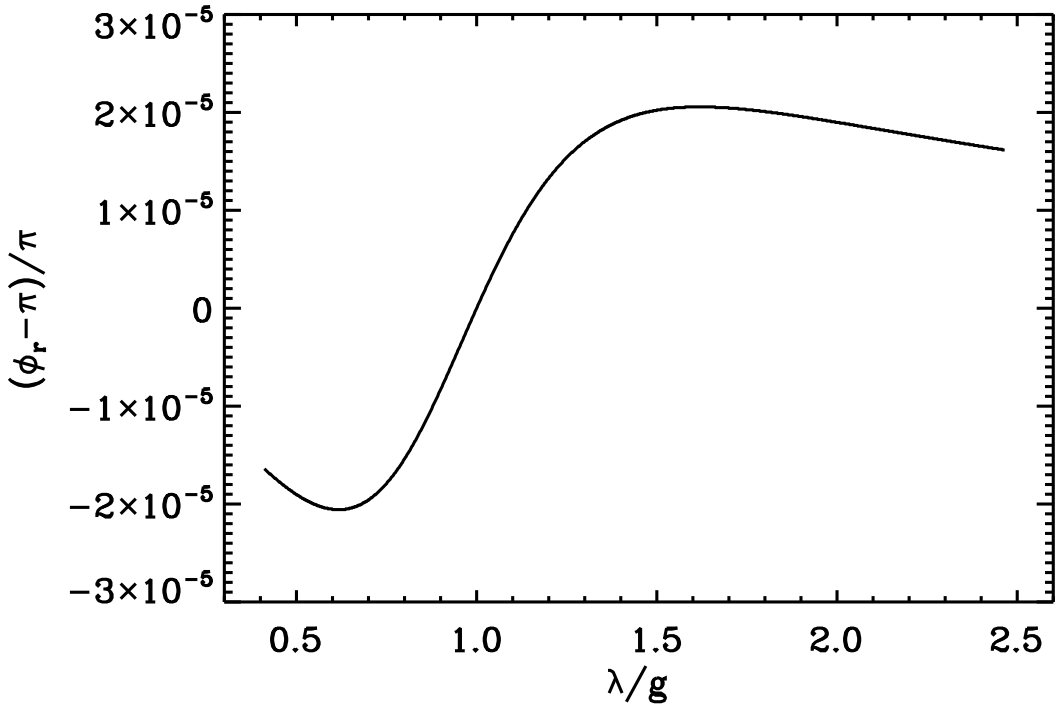

Figure 4.7. Phase shift of a resonant grid with G =(1.216 ± 0.003) mm and 2a = (0.152 ± 0.002) mm; σ_{Cu} = 56.6 10^6 m^{-1}.

4.2.2 Metal meshes in a FPI configuration

If two metal grids are used as reflectors in a FPI configuration the situation becomes more complex respect to the one described by Eq. 4.1, since the meshes are characterized by a complex wavelength-dependent reflectivity $R(\lambda)$ as well as by a reflection phase shift $\phi_r(\lambda)$. The relation between $\phi_r(\lambda)$ and the characteristic impedance of the grid Z_{grid} is [40]:

$$\phi_r = \pi - arctan\left(\frac{2Im(Z_{grid}/Z_s)}{1+2Re(Z_{grid}/Z_s)}\right) \tag{4.14}$$

where $Z_s = 377\Omega$ is the impedance of free-space. The phase shift of a resonant grid is shown in Fig. 4.14. It has been evaluated by Eq. 4.14 estimating the characteristic impedance of the R-grid with the values of the geometrical parameters in the caption. The phase shift is close to π when the reflectivity is high and it is smaller when the reflectivity drops. Note that the transmission maxima of the FPI occur when the total phase shift ϕ_{tot} is a multiple of 2π (see Eq. 4.4), so if $\phi_r < \pi$, for a given grid spacing, the resonant wavelength is larger than would occur for perfectly reflective mirrors. In the limit R $\rightarrow$ 1 we have $\phi_r \rightarrow \pi$ and transmission maxima occur as in the case of perfect mirrors.

The primary difference between millimeter Fabry-Perot interferometers and their counterparts at shorter wavelengths is the relative large aperture of the former, which are needed to accomodate the large beams required to avoid excessive diffrac-

tion loss. On the other hand the requirements on the reflector smoothness and parallelism are relaxed because the wavelengths are longer.

4.3 SZ spectrometry with MAD+FP

Multifrequency SZ observations can, in principle, determine cluster's gas temperature T_e, bulk velocity v_p, and optical depth τ [99]. However, the disentanglement of the degeneracy between them is not a simple task, even neglecting SZ signal foregrounds contamination. A preliminary investigation of information we can potentially extract from MAD + FP measurements has been performed. For simplicity, the effects of radio and infrared point sources, or instrumental systematic effects have been neglected. Galactic dust, primary CMB anisotropies and kSZ are the only contaminants considered in the analysis.
A Markov-chain Monte Carlo (MCMC) has been created using the parameters T_e, v_p, and τ to find realistic error regions for them. The MCMC is based on the Metropolis-Hastings algorithm, which randomly steps through a parameter space and accepts all points whose likelihood is greater than the previous point. If the likelihood is less than the previous point, the current point is accepted with a probability given by the ratio of the two likelihoods. To get the most conservative result weak input priors on each cluster parameter have been set.
This technique has been applied to one simulated galaxy cluster observed in MAD+FP bands (143, 200-300 (FPI) and 345 GHz) with 1 pixel (FWHM = 4.5 arcmin) and differential observation in the sky with a beamthrow of 10 arcmin. The input parameters of the cluster are: T_e = 6.9 keV, v_p=300 km s^{-1} and τ=1.7 10^{-2}.
The simulation of the microwave sky follows the approach presented in [100] and [98]. The contribution of galactic thermal dust emission has been evaluated by the prediction of [35], extrapolating the model to microwave frequencies. In Fig. 4.8 tSZ spectrum (combined with the relativistic corrections) is shown as a purple line. The contaminants such as galactic dust, primary CMB anisotropies and kSZ are the red, the green and the cyan lines respectively. The black line, marked as *total*, is obtained summing all the contributions listed previously. The corresponding MAD+FP data points (24 h observation time) are shown as black triangles. The MCMC recovered spectrum is the yellow band ($\pm 1\sigma$) and the corresponding output parameters are $T_e = (6.85 \pm 0.69)$ keV and $\tau = (1.77 \pm 0.18)10^{-2}$. They are in good agreement with the input ones.
The next step will be to improve this analysis adding more realistic observational conditions, including all the sources of possible contamination and confusion from astronomical sources and atmospheric fluctuations. Also all the instrumental effects should be considered, like the spatial features (map extension, angular resolution, observational strategy), the spectral capabilities (spectral coverage and resolution), and noise (due to CMB, telescope and atmospheric photon noise). The key topic is the determination of the SZ signature constraining both the cluster and foregrounds parameters by means of a Bayesan approach based on MCMC on simulated microwave sky maps.

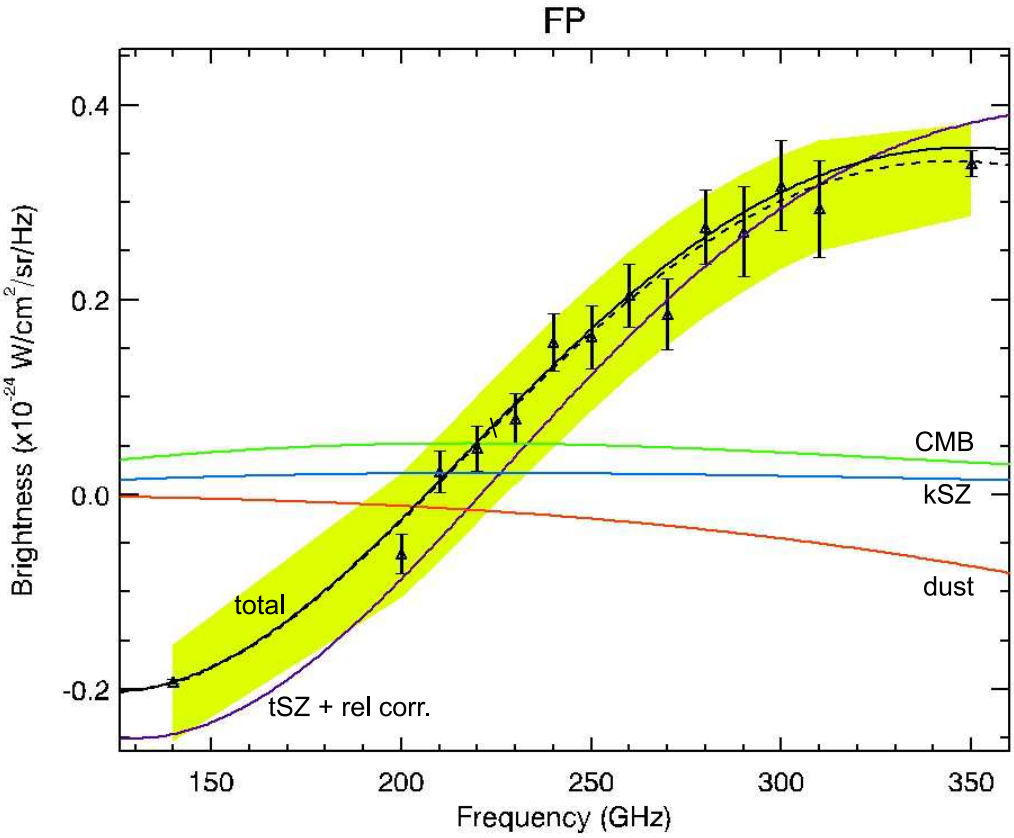

Figure 4.8. Simulated SZ brightness observed in MAD+FP bands (143, 200-300 (FPI) and 345 GHz) with 1 pixel (4.5 arcmin). The input parameters are: $T_e = 6.9keV$, $v_p = 300kms^{-2}$ and τ=1.7 10^{-2}. The yellow line is the MCMC recovered spectrum $\pm 1\sigma$. The corresponding output parameters are in good agreement with the input ones (credits L. Lamagna).

Chapter 5

Metal meshes transmission measurements and HFSS modeling.

The Fabry-Perot interferometer is composed of two reflecting mirrors inside which the reflected waves interfere constructively to produce a series of transmission maxima (see Sec. 4.1). The resonant fundamental standing wave has a wavelength of twice the optical path length of the cavity. The distance between the two reflective surfaces can be varied in order to produce a scanning pass-band optical filter.
In previous studies metallic meshes have been employed as partially reflecting surfaces in a Fabry-Perot interferometer configuration [93], [107], [84]. The main advantage is that metal grids allow the reflectivity coefficient of the reflecting surfaces to be tuned by adjusting the geometrical properties of the mesh. The required FPI transmission profile can be easily obtained by choosing the right geometrical path of the mesh.
Cross-shaped metal grids have been used for many years as band-stop filters in many microwave astronomy applications. In Sec. 4.1 we have seen that resonant grids show a resonant wavelength of $\approx$1.5 G, where G is the length of the cross bar that lies parallel to the incident electric field.
In this chapter the transmission response of a FPI composed of two resonant metal grids is explored. Since the arrays have a frequency dependent reflectivity and phase (see Sec. 4.2), they produce a shift of the frequency of the Fabry-Perot modes from that predicted by the classical model [53].
A full characterization of this innovative system is needed. To this purpose three experimental setups have been employed: the first is devoted to determine the optical properties of the cross-shaped metal grid alone (see Sec. 5.1); the last two are employed for the measurement of the transmission profile of the prototype of FPI composed by two metal grid in a resonant cavity configuration (see Sec. 5.2).
On the other hand, the comparison among experimental results and HFSS modeling allows the response of metal mesh structures to be predicted and tuned for exact requirements, reducing the financial costs that the production of several grids geometries should requires (see Sec. 5.4). A discussion of the results obtained by this work and future perspectives of this study will be presented in Sec. 5.6.

Figure 5.1. The resonant grid employed for reflection and transmission measurements. Geometrical parameters are listed in the text.

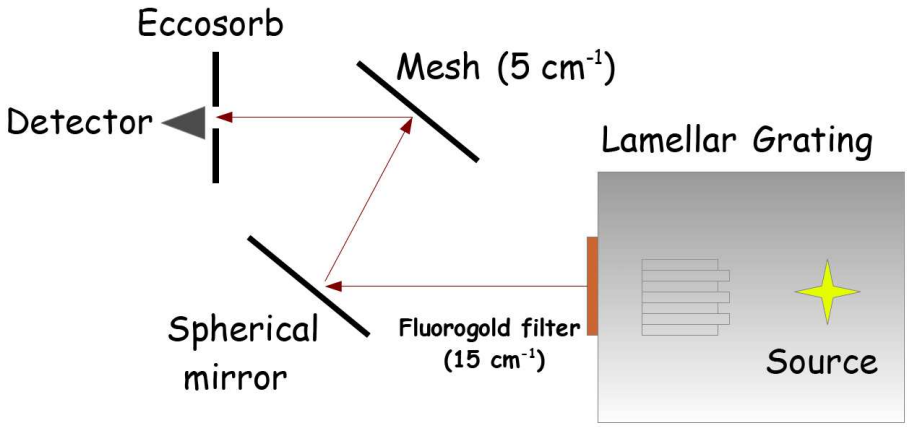

Figure 5.2. The experimental setup used for the measurements of the spectral behavior of the metal mesh reflection coefficient.

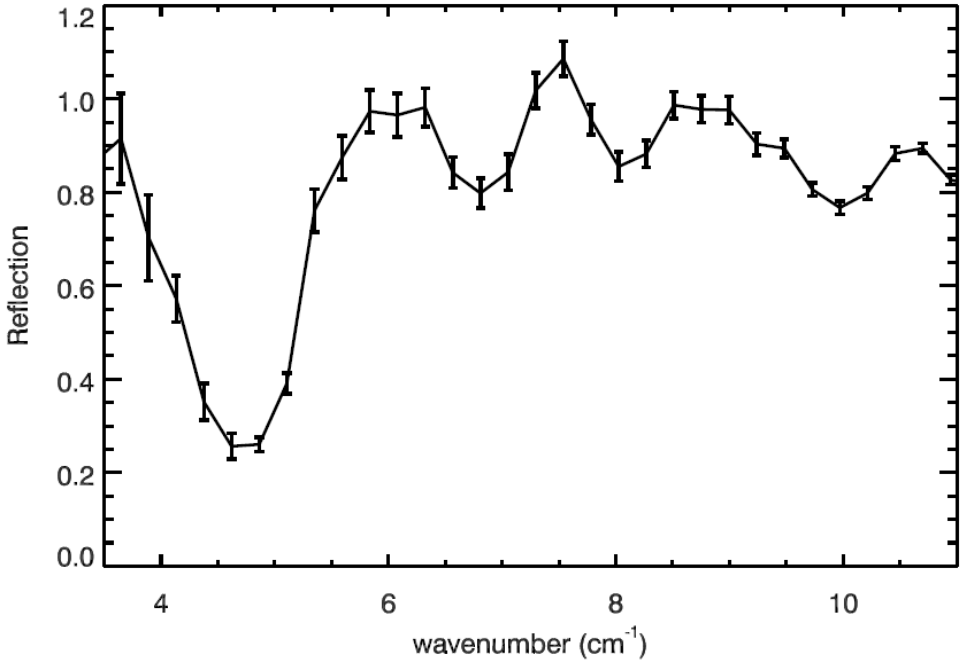

Figure 5.3. Reflection coefficient of the resonant grid in the 120 - 300 GHz range (4 - 10 cm^{-1}).

5.1 Reflection and Transmission measurements of the resonant grid

The first set of transmission measurements were performed on a single layer of a copper crosses-shaped grid, with the following geometrical properties:

- G = 1.216 mm
- 2a = 0.152 mm
- 2b = 0.186 mm

The metal mesh is shown in Fig. 5.1. The relation in Eq. 4.13 suggest a resonance frequency close to 150 GHz (5.48 cm^{-1}). The experimental setup to perform the measurement of the metal mesh reflection coefficient as a function of the frequency is shown in Fig. 5.2: the radiation emitted by the Hg lamp is sent inside the Lamellar Grating Interferometer LR-100 (see Fig. 5.7). After the interference process the radiation hits a spherical mirror, that collimates the beam. As last step the metal grid reflects the beam towards the detector.
The Lamellar Grating performs the interference process through the splitting of the wavefront obtained by two sets of mirrors, one fixed and one mobile, that introduce an optical path difference between the two beams. One of the two sets is fixed while the other is controlled by the linear position system M505.2PD (Physik Instrumente), managed by a Lab-View software.

When the two sets are at the same position respect to the incoming radiation (z.p.d.), they act as a plane mirror, otherwise an optical path difference is created and the interference between the two reflected beams takes place.
The source is a Hg lamp (Philips HPK, 125 Watt). Its spectral behavior can be approximated as a black body at 3000 K. A water refrigerator circuit guarantees the cooling of the whole instrument. In front of the lamp a chopper modulates the radiation with a 12 Hz reference frequency. Eccosorb on its blades acts as a black body at room temperature. At the exit of the interferometer there is a fluorogold filter in order to cut-off the IR radiation. The interferograms can be recorded by means of step by step and fast scan procedures (see Sec. 3.3.1 and Sec. 3.3.2). The detector is a bolometer maintained at 1.6 K inside a dewar by means of liquid ^{4}He. The detector has been vignetted by an Eccosorb surface with a 1.2 cm diameter hole matching the photometer window. The optical alignment can be performed placing a planar mirror instead of the two sets and using the visible radiation emitted by the lamp.
Step by step interferograms have been recorded setting a mechanical step length equal to 80 μm and the total number of steps equal to 260, in order to obtain a spectral resolution of about 0.24 cm^{-1} (7 GHz).
All the measured spectra need to be normalized to the one corresponding to the lamp emission (background). This kind of measurement is realized placing a plane mirror instead of the metal mesh. Fig. 5.3 shows the measured reflection coefficient: the profile has a minimum at 4.8 cm^{-1}, differently by the expected value (5.5 cm^{-1}).
The experimental setup adopted for the measurement of the transmission coefficient of the mesh is shown in Fig. 5.4: the spherical mirror has been eliminated while the metal mesh has been placed between the interferometer and the detector in a f/4 converging beam.
Interferograms have been recorded by means of fast scan procedure, with a scanning velocity equal to 0.5 cm s^{-1} and a total excursion of 2 cm, corresponding to a spectral resolution of about 0.25 cm^{-1}. Fig. 5.5 shows the measured transmission coefficient: even in this case the profile has a maximum at 4.8 cm^{-1}.
The filter FWHM is about 2 cm^{-1} and the resonance value is less then unity, probably due to ohmic losses induced bu surface currents and a partial oxidation of the metal. At frequencies above 210 GHz (7 cm^{-1}) the mesh operates in a diffraction regime but this problem seems to be attenuated by the convergence of the beam, unlike the reflection measurement, where the diffractive behavior is more evident (see Fig. 5.3). The results obtained by this set of measurements will be compared to HFSS modeling in Sec. 5.4.

5.2 FPI transmission measurements

In this chapter the behavior of the system composed of two cross-shaped arrays in a FPI configuration will be explored. Transmission measurements analyzed previously allow to predict the performance of this innovative FPI: the reflection coefficient varies with the frequency, then, following Eq. 4.1, the Airy profile is expected to be broad near the resonance (low reflection, few interfering rays) and becoming narrow toward high frequencies (high reflection, many interfering rays).

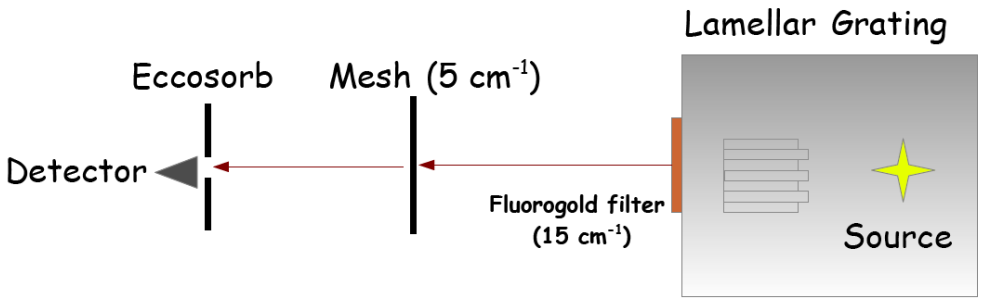

Figure 5.4. The experimental setup used for the measurements of the spectral behavior of the metal mesh transmission coefficient.

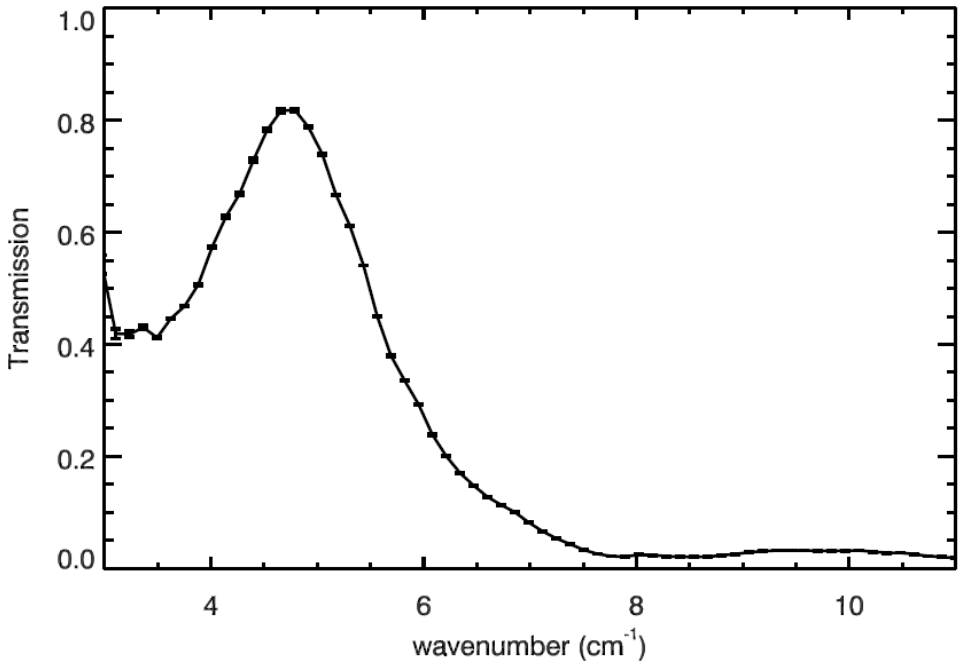

Figure 5.5. Transmission coefficient of the resonant grid in the 120 - 300 GHz range (4 - 10 cm^{-1}).

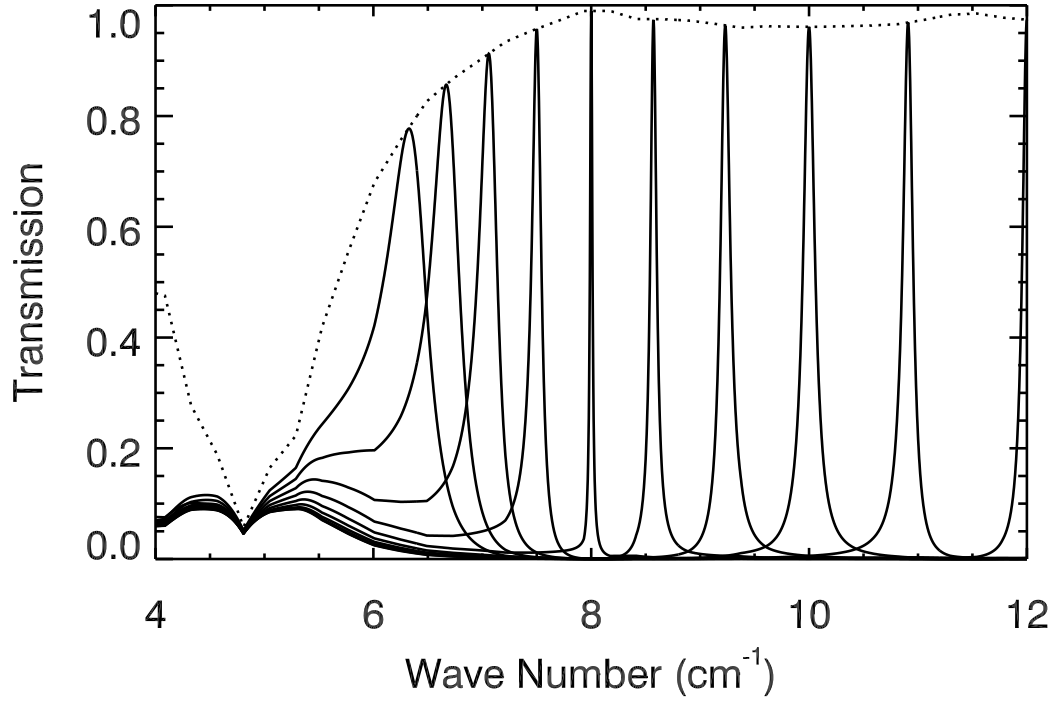

Figure 5.6. Analytical simulation of the transmission profiles of the system composed of two R-grids in a FP configuration (solid line). A complementary band-stop R-grid rejects unwanted radiation (dotted line). The FWHM of resonance peaks varies with frequency because of the reflection coefficient trend.

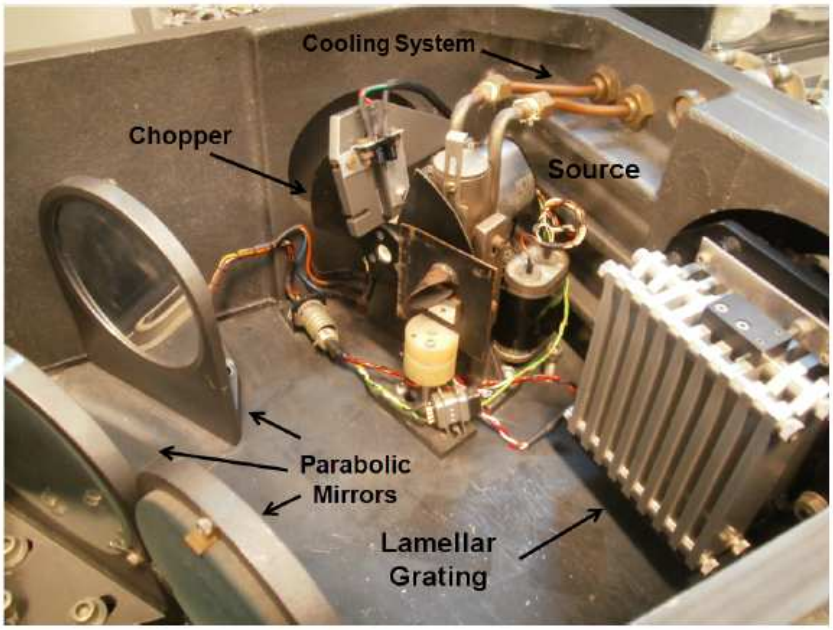

Figure 5.7. The Lamellar Grating LR - 100.

In Fig. 5.6 an analytical prediction of the FPI performance in the range of interest is shown: the Airy profile has been evaluated considering the dependency of the measured reflection coefficient on the frequency. Ten spectral elements, corresponding to the first order of ten values of the separation are shown. The distance among the reflective surfaces varies between 0.5 mm (the lowest frequency peak) and 0.5 mm (the highest frequency peak). Also the Finesse depends on frequency and its value is approximatively 20 in the range of interest.
In the ideal case the boundary conditions on the mirror surface would impose a 180 deg phase change on the electric field on reflection but the resonant behavior of the metal meshes was found to shift the frequency of the FPI modes from that predicted by the classical model (Eq. 4.6). The analytical simulation in Fig. 5.6 does not take in account of the phase shift, that has been explored both experimentally (see Sec. 5.2.2) and by means of HFSS models (see Sec. 5.4). Even near-field effects ($\lambda < d$) and diffraction above 250 GHz are not included in this calculation for simplicity.
Although this simulation does not consider all the real effects, some critic problems connected to this R-grid geometry can be already identified in Fig. 5.6: first of all, the diffraction region of the metal grid falls into the frequency range (200-300 GHz), where the MAD+FP instrument will perform measurements of SZ effect (see Sec. 1.3). Secondly the performance of the FP is strongly connected to the variation of the reflection coefficient, that show a variation of about 30 per cent in this range. However one of the advantages of a FPI composed by two metal meshes is that FP fringe pattern can be easily changed by modifying the geometry of the two grids. Once demonstrated that the experimental measurements match HFSS results for one particular geometry, one can tune the metal mesh geometry employing HFSS model until the required FPI fringe pattern is fulfilled. This approach reduces the financial costs connected to the production of several grid geometries.

5.2.1 Parallelism optimization

The first set of measurements is devoted to the optimization of the optical alignment of the metal meshes system, in order to reduce all the misalignment effects described in Sec. 4.1.1. In Fig. 5.9 the experimental setup is shown. It includes the Backward Wave Oscillator (BWO) [60], as source of microwave radiation, the chopper and the detector, a Golay cell. The supports on which the two meshes have been stretched are two brass hollow cylinders (diameter 2 cm), designed in order to make them as flat as possible. They are anchored on a mechanical stage, able to regulate the separation among the meshes with 10 μm resolution. The alignment of the system is controlled by two tilters, corresponding to the horizontal and vertical directions (see Fig. 5.8).

The beam emitted by the BWO is collimated by a plano-convex lens and then focused on the detector by a second lens. They are both made of High Density Polyethylene (HDPE), a material characterized by a low absorption index in the mm range. The ZEMAX optical layout of the system composed by the two lenses is shown in Fig. 5.11 [13]. The corresponding geometrical parameters are shown in Table 5.1.

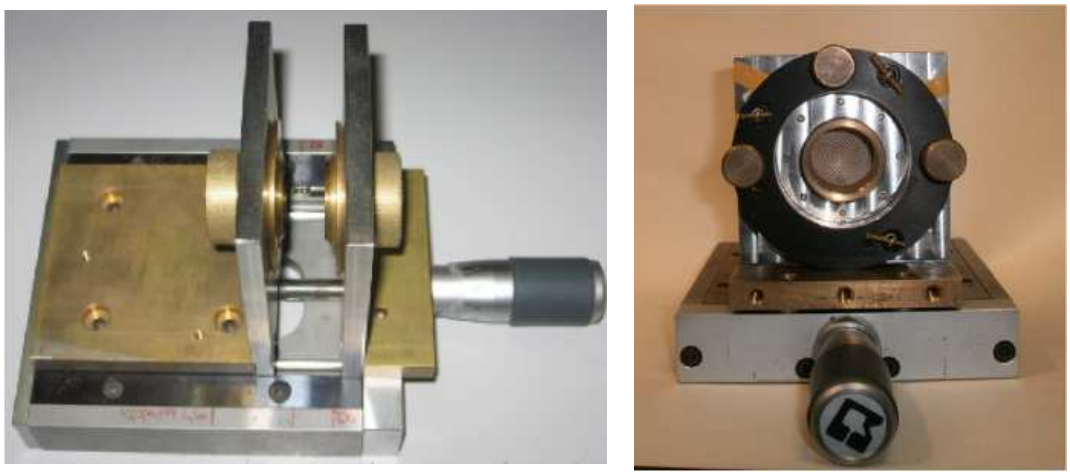

Figure 5.8. Metal meshes have been stretched on two cylindric supports: on the right the one that can tilt the position, on the left the one that can perform the scan, by means of the mechanical stage on which is mounted.

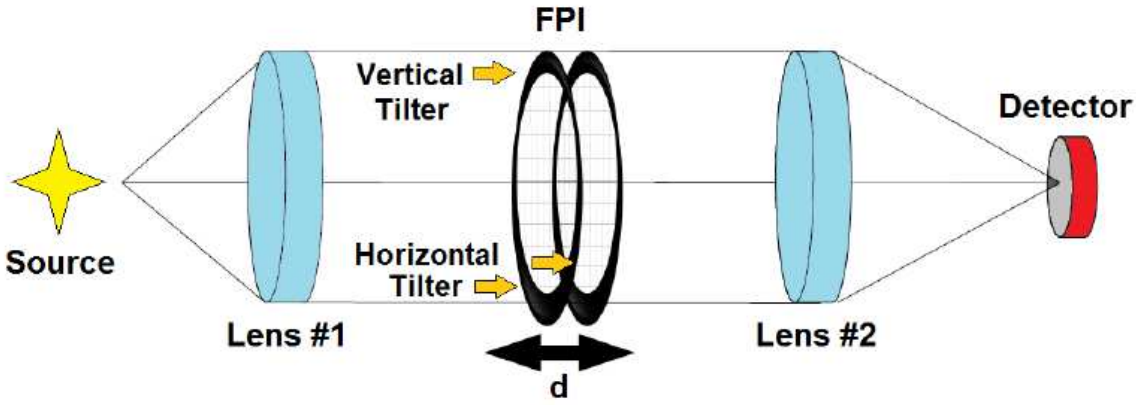

Figure 5.9. The experimental setup devoted to the optical alignment tests is shown: the Backward Wave Oscillator (BWO) is the source of microwave radiation while the detector is a Golay cell. The radiation is modulated by a chopper and the two meshes are stretched on the two brass supports.

Table 5.1. Geometrical parameters of the two lenses.

	Lens1	Lens2
Curvature radius (mm)	60	79
Diameter (mm)	75	64
Thickness (mm)	10	13
Refraction index	1.5	1.5
Focal length (mm)	150	114
f-number	2.35	2.1

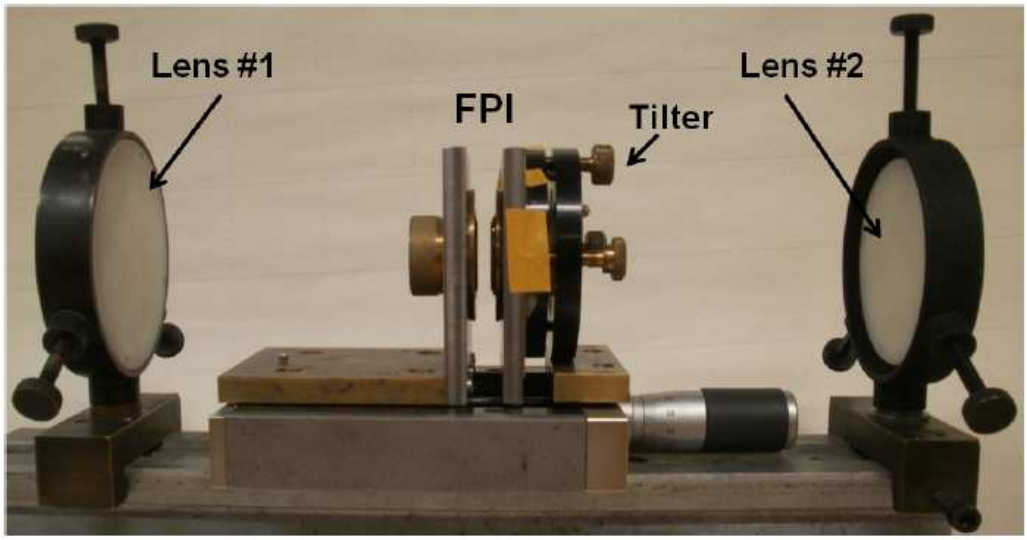

Figure 5.10. The experimental setup with two meshes stretched on the two brass supports, the mechanical stage and the two HDPE lenses.

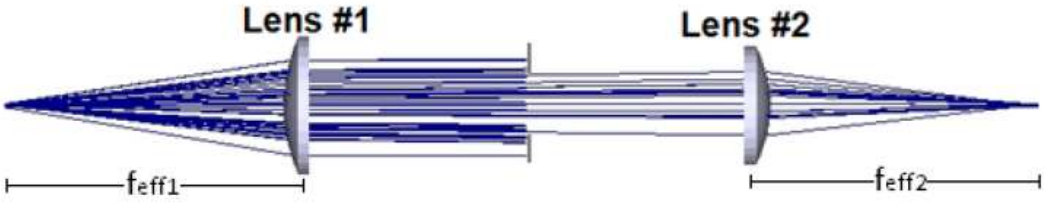

Figure 5.11. The ZEMAX optical layout of the system composed by the two lenses (credits D. Buzi).

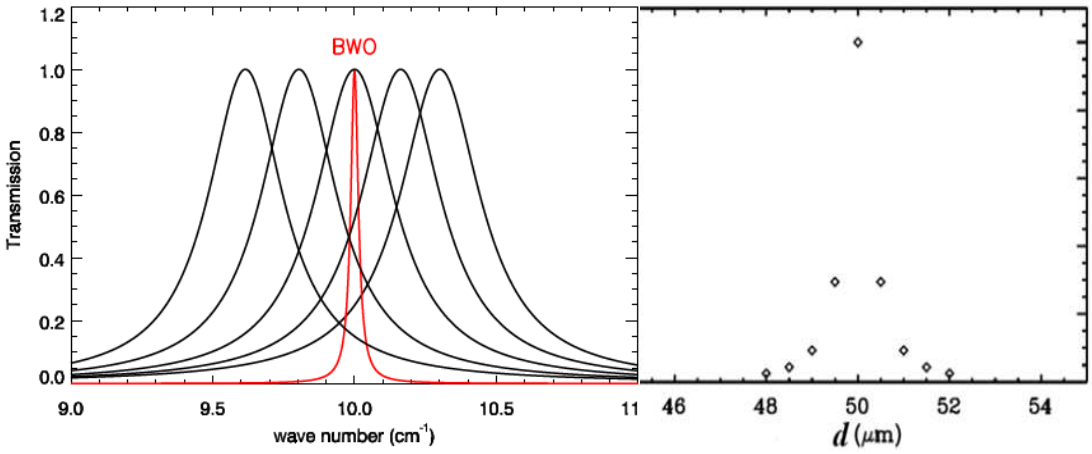

Figure 5.12. Left panel: the simulated BWO emission profile (red) with the FPI Airy profile evaluated for several spacing values (black). Right panel: the result of the convolution process.

The spectral emission of the BWO can be assumed monochromatic, while the transmission function of the FPI is given by the Airy profile, mainly depending on the distance between the two meshes and their reflection coefficient (see the left panel in Fig. 5.12). The measurement consists in varying the distance among the two plates in order to measure the convolution of the emission spectrum of the source and the transmission function of the FPI. The result is a good approximation of the Airy profile due to the fact that the BWO emission profile is close to a Dirac delta function (right panel in Fig. 5.12).

The two BWO frequencies adopted are ν_1=281.5 GHz and ν_2=362 GHz (σ_1=9.38 cm^{-1} and σ_2=12.06 cm^{-1}), corresponding to the first order spacings $d_1 = 0.532$ mm e $d_2 = 0.414$ mm. The BWO frequency range is all inside the diffraction region, so this setup does not allow measurements of the Airy profile before 250 GHz. Another kind of source is needed to explore the behavior at lower frequencies, where the diffraction does not affect the instrumental response and for this reason the setup described in the next section has been employed.
In order to have preliminary information about the peak, the distance among the meshes is incremented from the zero position with steps equal to 50 μm, recording the signal at each step. Then the transmission profile is sampled with 10 μm steps near the maximum. Once the position of the peak has been determined, the tilters allow the parallelism to be improved. Each tilter modification is followed by a new scan in distance, in order to determine the new maximum position. The first order transmission profile of the FPI, corresponding to several inclinations, is shown in Fig. 5.13. Acting on the tilters the bandwidth has been reduced and the signal at the resonance has been increased. The signal corresponding to the first three orders of interference is shown in Fig. 5.14.

The intensity of the interference peak at the third order is lower then the first and second orders because of the higher distance among the plates, that produces a

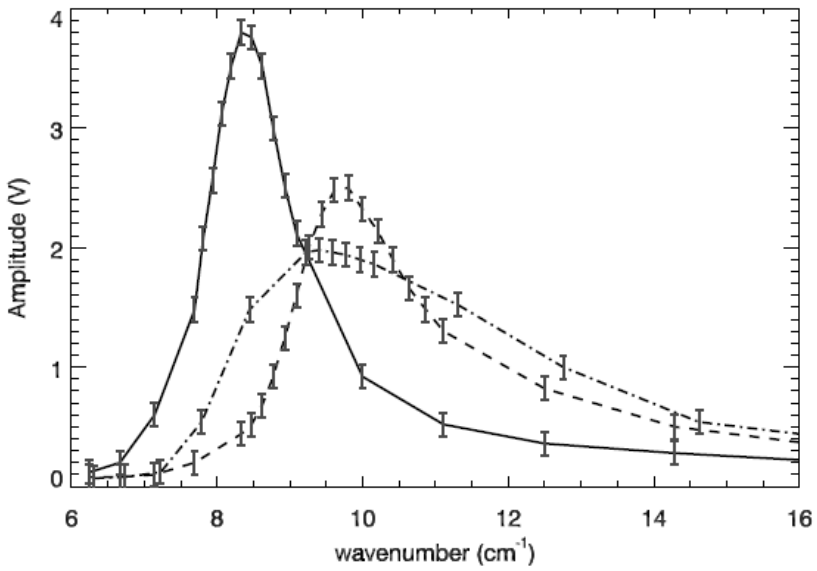

Figure 5.13. Measured FPI transmission profiles corresponding to three different mesh inclinations, for incoming radiation at ν_1=281.5 GHz and m = 1.

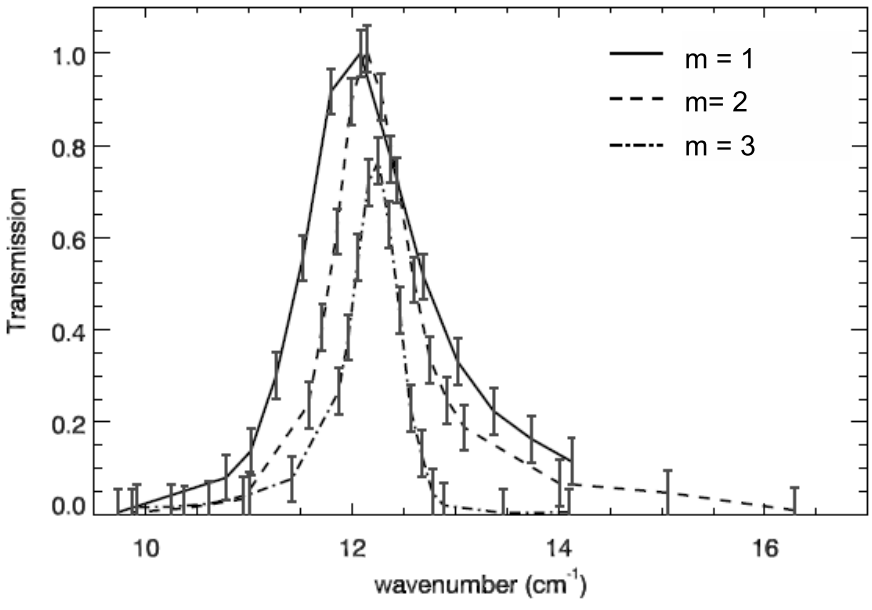

Figure 5.14. Measured transmission profile obtained for the first three orders of interference, with incoming radiation at ν_2=362 GHz.

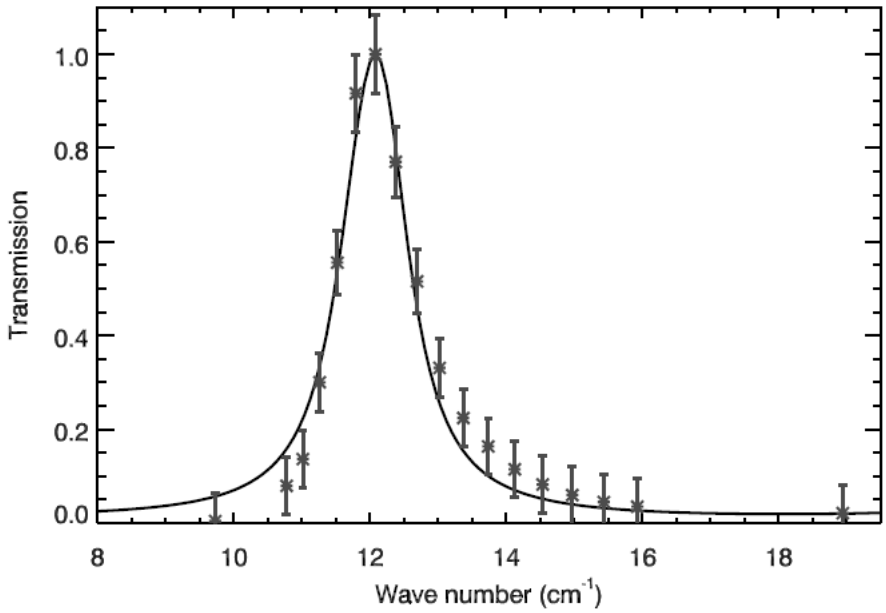

Figure 5.15. Transmission data of the first order are in agreement with the theoretical function (black line) determined by the set of parameters listed in Table 5.2 (credits D. Buzi).

Table 5.2. Set of parameters fitting the transmission profiles shown in Fig. 5.15 (credits D. Buzi).

Incidence angle (deg)	3 ± 1
Tilt angle (deg)	2.0 ± 0.2
Reflectivity	0.85 ± 0.02
Separation (mm)	0.43 ± 0.01

reduction of the instrumental efficiency. The spectral resolution of the FPI increases with the interference order varying from 60 GHz (2 cm^{-1}) at the first order to 15 GHz (0.5 cm^{-1}) at the third order.
The measured spectral profile has been compared with the expression derived in [88], where the spectral FPI transmission fringe pattern is expressed as a function of the angle of the incident beam, the tilt angle among the plates, the reflectivity and the distance. The set of parameters corresponding to the minimum of Chi Square variable of the transmission profile shown in Fig. 5.15 is listed in Table 5.2.

The experimental results discussed in this section highlight the FPI limitations connected to the convergence of the beam, the angle of incidence and the lack of parallelism among the two plates. The next step will be the improvement of the scanning and tilting strategy, replacing the manual stage with an automatic system suitable to a cryogenic environment like the one in proximity of the MAD array of detectors (4.2 K).
Higher values of the resolution power requires an automatic mechanical stage like the one employed in the sub-mm Fabry-Perot Interferometer Bolometer Research

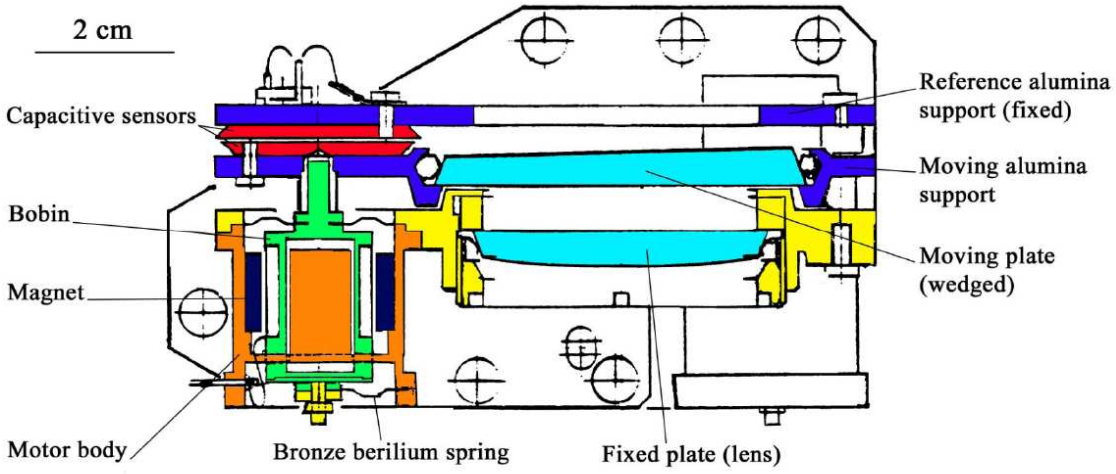

Figure 5.16. The design of the Fabry-Perot interferometer of the FIBRE experiment.

Experiment (FIBRE) [82] or in the imaging spectrometer for astronomy in the sub-mm band SPIFI (South Pole Imaging Fabry-Perot Interferometer) [11]. In the first case the scanning is provided by three push-pull motors composed of a mobile coil in a fixed magnetic field created by permanent magnets. The employment of superconducting wire bobins assures a low Joule power dissipation. Three capacitive sensors aligned with the three motors monitor the position of the moving plate: one part of the sensor is attached to the support of the moving plate, and the other part on a fixed plate acting as a position reference (see Fig. 5.16).
On the other hand SPIFI employees two scanning FPI, with the two mesh rings held magnetically to an aluminum frame, with one of them mounted rigidly to the optical bench while the other can translates, changing the cavity spacing. Two steel plates at either side of the frames assures the parallelism for relatively small distances. In this case the scanning is performed with a piezoelectric transducer specially made for cryogenic use and nulling capacitance bridge circuit set the piezoelectric transducer voltage to measure and control the cavity spacing (see Fig. 5.17).

5.2.2 Measurements of phase shift on reflection

In the derivation of the Airy function described in Sec. 4.1 both the magnitude of the reflectivity and the phase shift on reflection are considered. While an ideal mirror has a phase shift of 180 deg for all frequencies, a metal mesh can have a large variation in the phase shift as a function of frequency.
The resonant meshes adopted in this work were found to shift the frequency of the FPI modes from that derived by the classical analytical prediction. This is due to the frequency dependent phase shift inducing the cavity to appear longer or shorter depending on the position in frequency of the modes relative to the resonant frequency of the crosses.
At high orders, the major source of phase is the gap path difference and not the

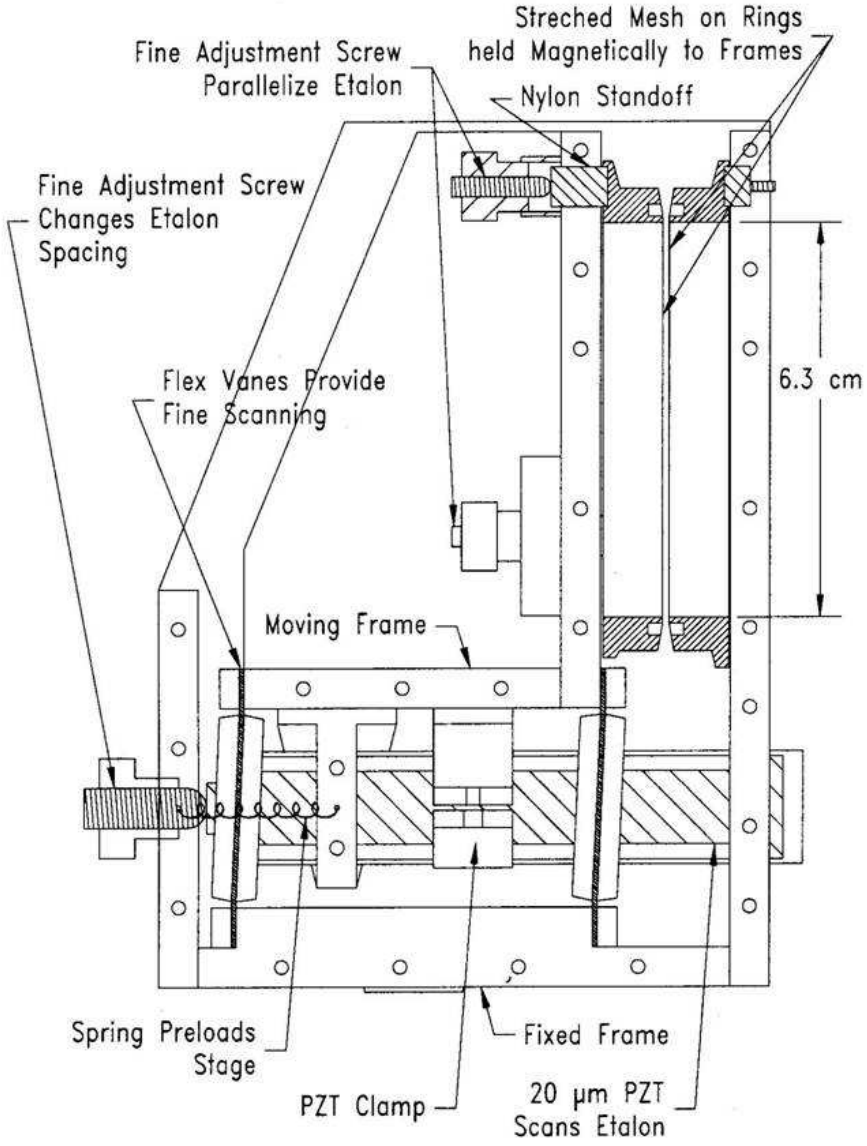

Figure 5.17. The design of the Fabry-Perot interferometer of the SPIFI experiment.

Table 5.3. Frequency shift due to the phase shift on reflection ϕ_r measured for the second and the third order, corresponding to the profiles shown in Fig. 5.18.

m	d (mm)	$\nu_{teo}(GHz)$	$\nu_{mis}(GHz)$	$\phi_r(deg)$
2	1.66	181	191 ± 3	200
2	1.60	188	195 ± 3	194
2	1.55	194	202 ± 3	196
2	1.50	200	206 ± 3	191
3	2.34	192	199 ± 3	197

mirror itself, so the deviations from an ideal behavior can be managed through care in maintaining mirror flatness and parallelism. At low orders, for a FPI constructed with metal meshes, the phase shift built up in the mesh itself has a more significant effect [71].
With good knowledge of the gap spacing d and the measurement of the FPI resonance wavenumber σ, one can determine the phase shift on reflection rewriting Eq. 4.5 in the following way:

$$\phi_r = 2\pi d\sigma - (m-1)\pi \tag{5.1}$$

The experimental setup is the same adopted for the transmission measurements described in Sec. 5.1 (see Fig. 5.4) with the FPI instead of the mesh. In this case the f/4 converging beam coming out from the Lamellar Grating is collimated by the first HDPE lens (see Table 5.1), then sent to the FPI interferometer and finally focused by the second lens on the bolometer after the interference process. Because the Lamellar Grating can reach a spectral resolution of about 0.2 cm^{-1} (6 GHz), at most two or three spectral elements for each FPI peak can be detected, being the FPI FWHM close to 0.6 cm^{-1} (18 GHz). Even if the Lamellar Grating resolution does not allow a good knowledge of the shape of the FPI transmission profile, it provides a precise measurement of the shift in frequency due to the phase shift on reflection. Both the measured and expected values of the resonance frequency are shown in Table 5.3), corresponding to several spacings d and interference orders m. The corresponding phase shift ϕ_r has been evaluated by means of Eq. 5.1. In Fig. 5.18 the measured transmission profiles for m = 2 are shown. The frequency range in which one can detect the interference peaks turns out to be only 50 GHz: for frequencies smaller then 150 GHz the resonance of the mesh makes the FPI interferometer not enough efficient because the reflectivity of the meshes drops down, while the diffraction region seems to take place at 200 GHz and not at 250 GHz as predicted by the transmission line theory. In addition we were not able to detect first order interference peaks because we did not know a priori the value of the distance needed to produce the peak in a so small frequency range, being the frequency shift unknown. This difficulty can be avoided by means of a different approach, consisting in determining a new relation among distance and frequency of the FPI peak taking in account the phase shift, by means of HFFS. If this new relation is consistent with values reported in Table 5.3, it can be assumed as the new FPI resonance condition instead of Eq. 4.6. This argument will be discussed in details in Sec. 5.4.

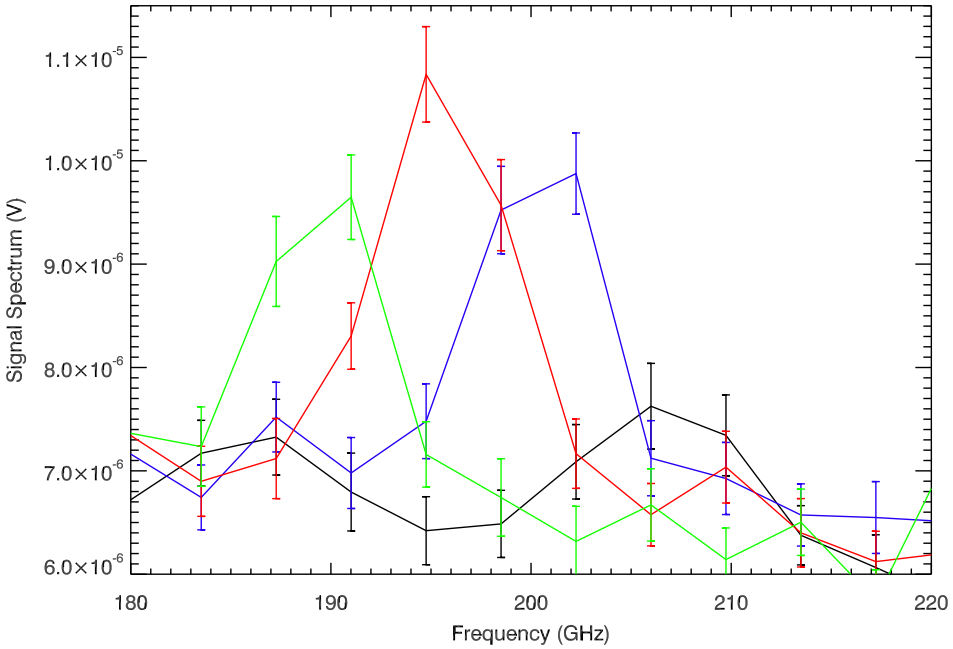

Figure 5.18. Measured transmission profiles corresponding to the second order, obtained scanning the distance between the two meshes for the four values reported in Table 5.3.

5.3 HFSS simulations

An usefull tool to explore the optical properties of metal grids systems is the Ansoft Corporation software HFSS (High Frequency Structure Simulator)[1], an interactive software package able to calculate the electromagnetic behavior of a generic device employing the Finite Element Method (FEM). A general FEM software is a design tool for engineers and physicists, employing rapid computations to solve large problems insoluble by analytical expressions. The FEM involves subdividing a large problem into individually simple constituent units which are each soluble via direct analytical methods, then reassembling the solution for the entire problem space as a matrix of simultaneous equations. FEM softwares can solve mechanical (stress, strain, vibration), aerodynamic or fluid flow, thermal, or electromagnetic problems. In the case of HFSS the full problem space is divided into thousands of tetrahedra and the field in each element is represented with a local function. By representing field quantities in this way, the system can transform Maxwell's equations into matrix equations that are solved using traditional numerical methods. There is a trade-off among the size of the mesh, the desired level of accuracy, and the amount of available computing resources. To produce the optimal solution, HFSS uses an iterative process, called adaptive analysis, in which the mesh is automatically refined in critical regions. First, it generates a solution based on a coarse initial mesh. Then, it refines the mesh in areas of high error density and generates a new solution. When selected parameters converge to within a desired limit, HFSS breaks out of

[1] www.ansys.com

the loop. HFSS employs a Computer Aided Design (CAD) interface to allow input of the model geometry. Once an object has been created, material parameters can be assigned, either chosen from the HFSS library which contains a large number of material parameters for microwave frequencies or defined manually by the user. In Fig. 5.19 the HFSS model for the unit cell of the infinite array representing the metal mesh to be analyzed is shown. The model consists of the metal grid periodic element inside a box of air (left panel in Fig. 5.19).
The wave equation that is solved by Ansoft HFSS is derived from the differential form of Maxwell Equations, requiring that the field vectors are single-valued, bounded, and have continuous distribution along with their derivatives. Along boundaries or sources, the fields are discontinuous and the derivatives have no meaning. Therefore Boundary Conditions specify the field behavior at the edges of the problem region and object interfaces (central panel in Fig. 5.19). They also allow to reduce the model complexity.

There are three types of boundary conditions:

- Excitations like wave ports or lumped ports
- Surface Approximations like symmetry planes, perfect electric or magnetic surfaces, radiation surfaces, background or outer surface.
- Material Properties, that is boundary between two dielectrics, finite conductivity of a conductor.

For example *Perfect E* condition represents a perfectly conducting surface while *Perfect H* represents a surface on which the tangential component of the H-field is the same on both sides. A *Radiation Boundary* condition could be used to simulate an open problem that allows waves to radiate infinitely far into space, absorbing the wave at the radiation boundary and carrying the boundary infinitely far away from the structure. A *Perfectly Matched Layer* (PML) boundary could be used to simulate materials that absorb outgoing waves. Assigning *Master and Slave Boundaries* enables to model planes of periodicity where the E-field at every point on the slave boundary surface is forced to match the E-field at every corresponding point on the master boundary surface to within a phase difference (see Fig. 5.20).

In order to specify the sources of electromagnetic fields one may assign several types of excitations. *Incident Plane Wave* is a wave that propagates in one direction and is uniform in the directions perpendicular to its direction of propagation. Other incident waves are available such as Gaussian beams and near field and far field waves. Most of the modeling in this thesis use *Wave Ports* placed on the interface coupling the model to the external world, through which excitation signals enter and leave the waveguide structure (right panel in Fig. 5.19). Assuming the x and y-axes lying in the cross-section of the port and the z-axis lying along the direction of propagation, the excitation field for a port can be expressed by:

$$\vec{E}_m(x,y,z,t) = \Re\left[\vec{E}_m(x,y)e^{j\omega t-\gamma_m z}\right] \tag{5.2}$$

where $\vec{E}_m(x,y)$ is the electric field mode pattern of mode m and γ_m is the complex propagation constant. The field pattern of a traveling wave inside a waveguide

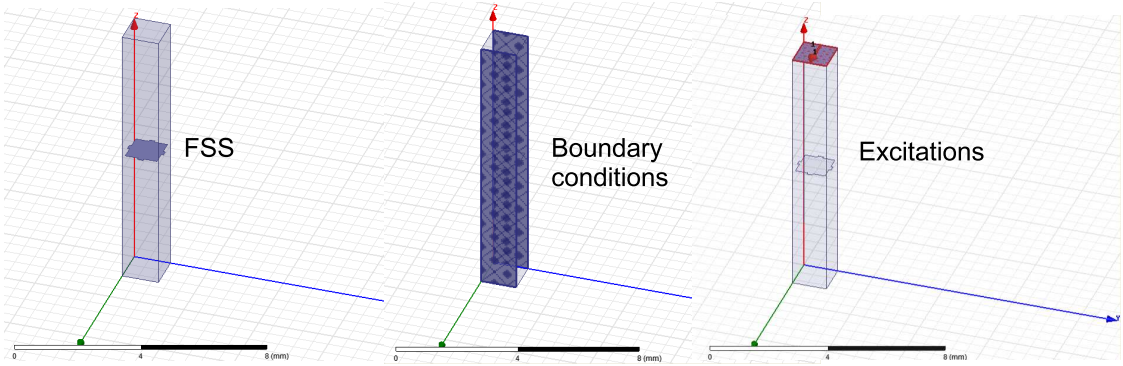

Figure 5.19. HFSS model for the computation of transmission properties of a FSS. The left panel shows the period element of the FSS infinite array placed inside an air box. The central panel highlights the boundary conditions at the edges of the model region. The left panel shows the electromagnetic field excitation on the interface of the model.

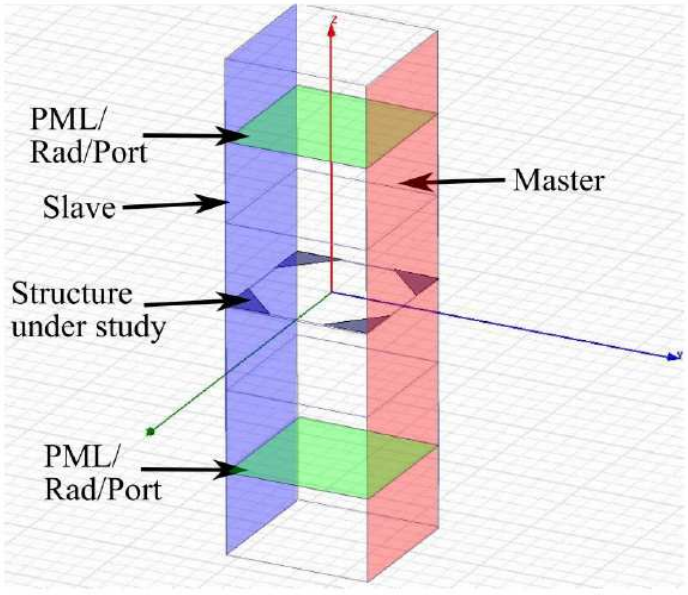

Figure 5.20. Typical HFSS unit cell with Master and Slave Boundary conditions terminated on the incident and exit faces by a PML.

is then determined by solving Maxwell equations for each mode. Unit cells for FSS simulations may be constructed using *Perfect E* and *Perfect H* linked boundaries combined with two wave ports acting as excitations, with one port above the plane of the structure and one port below. Being a_m and b_m the complex amplitudes of the incident and reflected modal E and H-fields, the generalized Scattering matrix (S-matrix hereafter) relates the incident and reflected/transmitted modal amplitudes in the following way:

$$\mathbf{b} = S\mathbf{a} \tag{5.3}$$

The size of the two vectors **a** and **b** is the total number of modes N obtained by adding up the number of the modes on all ports of the model (the modeling of this wok includes two ports). The element S_{ij} specifies the factor to be applied to the incident amplitude a_j to get the reflected and transmitted amplitude b_i if all the other incident modes are turned off. This can be described mathematically as:

$$S_{ij} = \frac{b_i}{a_j}|_{a_k=0, k\neq 0} \tag{5.4}$$

As a direct result of the field solution, the reflection and transmission properties of the FSS are cast in terms of the computed S-matrix entries interrelating the ports modes. The incident fields, total field, scattered fields of the plane waves and other derived field quantities such as Poynting vector can all be exported.
The adaptive meshing algorithm searches for the largest gradients in the E-field or error and sub-divides the mesh in those regions, in order to give the most accurate and efficient mesh possible. It also targets singularities, such as the edge of a conductor. The Tetrahedron Refinement controls the mesh growth for each adaptive pass, ensuring that between each pass the mesh is sufficiently perturbed and guarantying the elimination of false convergences. After each adaptive pass, HFSS compares the S-Parameters from the current mesh to the results of the previous mesh (Delta S), stopping the analysis when there is no significant improvement by adding more tetrahedral elements.
If a frequency sweep is added to a model, it will solve the fields for a range of frequencies using the mesh generated at the so-called solution frequency, corresponding to the last adaptive pass before convergence.
The main steps of a HFSS simulation are summarized in Fig. 5.21. The simulations described in the next pages were carried out using HFSS 13.0.

5.4 HFSS modeling for the R-grid

A complete characterization of the system composed by two cross-shaped grids in a FPI configuration requires the comparison among the experimental results presented previously and HFSS predictions. In this manner new meshes geometries can be tuned to obtain the instrumental requirements discussed in Chapter 1.
First of all the reflection and transmission measurements of the resonant grid will be compared to HFSS results in order to be sure of the agreement among experimental and model data.
Each HFSS simulation starts with the definition of the elementary cell representing

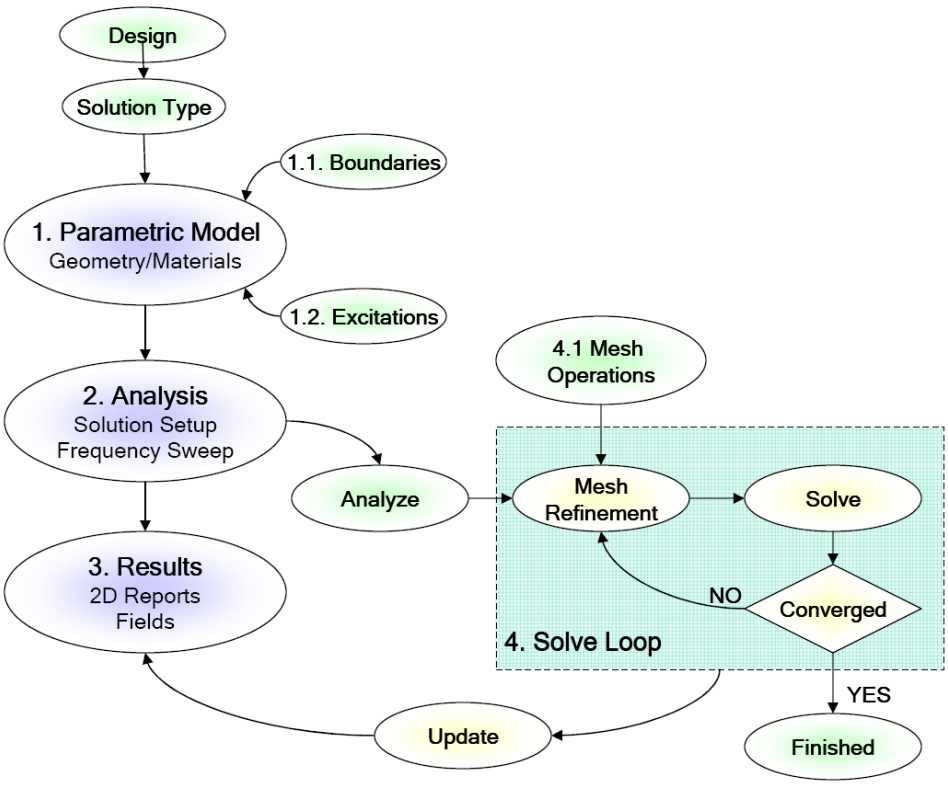

Figure 5.21. An overview of the main HFSS processes: the Parametric Model Generation allows to create the geometry, the boundaries and the excitations. Analysis Setup consists in defining the solution setup and frequency sweeps. By means of the Solve Loop the solution process is fully automated. 2D reports and field plots are shown in Results.

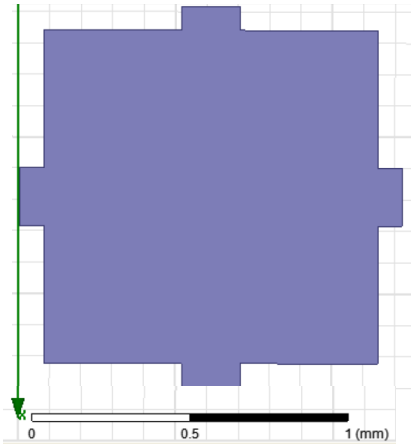

Figure 5.22. Elementary cell of the cross shaped resonant grid.

the periodic structure to be analyzed. This cell is repeated to the infinity by means of a specific boundary condition, as seen in Sec. 5.3. In Fig. 5.22 the elementary cell adopted for the cross shaped grid is shown.

The geometrical parameters adopted for the model are the following:

- G = 1.216 mm
- C = 1.064 mm
- L = 1.030 mm
- 2a = 0.152 mm
- 2b = 0.186 mm

The air box in which the elementary cell is placed has to be longer then the grid constant G. The metal mesh is assumed to be a perfect conductor, then the *Perfect E* condition is associated on its surface. Two *Wave Ports* placed on the two interfaces of the air box allow the excitation signals enter and leave the waveguide. *Perfect E* and *Perfect H* boundaries on the lateral interfaces of the air box, combined with the two wave ports, guarantee the infinite extension of the array. The reflection properties of the structure are evaluated in terms of the computed diagonal S-matrix elements S_{11} or S_{22}, while transmission coefficient corresponds to out of diagonal elements S_{12} or S_{21}. Fig. 5.23 shows the interaction of the incident plane wave with the metal mesh placed at the center of the air box, as evaluated by HFSS.
Transmission and reflection coefficients evaluated with HFSS are shown in Fig. 5.24, while experimental data (obtained with the setup described in Sec. 5.1) have been compared with HFSS results in Fig. 5.25 [13]: even if transmission line theory predicts a resonance frequency of about 164 GHz, the simulated transmission spectrum

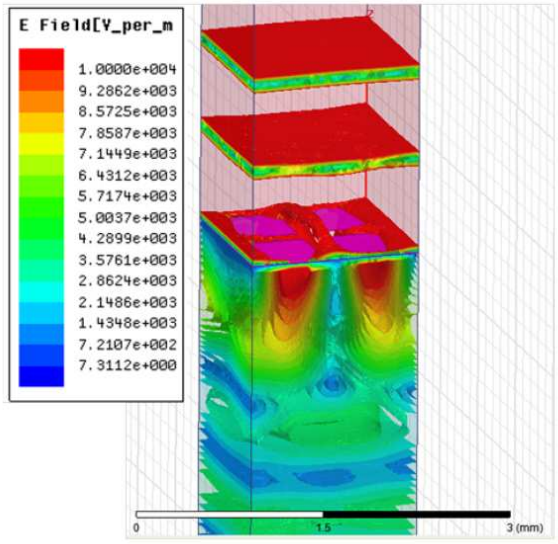

Figure 5.23. E-field interacting with the elementary cell.

show a resonance close to 150 GHz. On the other hand the shift between the two resonances, measured and modeled with HFSS, is about 6 GHz. This means that HFSS succeeds in taking in account of real effects much more then Transmission Line Theory. Anyway the maximum of the measured transmission is 20 per cent less then the unity, probably because of ohmic losses due to surface currents among the metal elements of the grid. The anomalies above 250 GHz derive from diffraction effects ($\lambda > G$) and a far-field computation would be required [87]. Experimental data seem to be not affected by diffraction, probably because of the convergence of the incident beam that damps all the anomalies, making them negligible.

5.5 HFSS model for two R-grids in a FPI configuration

Two R-grids in a FPI configuration have been modeled in order to reproduce the behavior observed experimentally, especially concerning the phase shift on reflection inducing a translation of the resonances of the interferometer. The comparison among the transmission profiles, measured and modeled, is not possible because HFSS simulations neglect real effects such as the plates displacement, the convergence of the beam or the lack of parallelism. On the other hand the classical approach is suitable to properly consider those effects, as seen in Sec. 5.2.1.

In Fig. 5.26 the wavenumber corresponding to the FPI peaks, as estimated by HFSS, is plotted as a function of the inverse of the separation d among the plates for the first three interference orders. The classical theory previsions are also shown as solid lines. The two horizontal lines remark the diffraction region above 250 GHz and the resonance of the single layer at 150 GHz, that limits the FP performance due to the decreasing of the reflectivity. The dots deviate from the classical behavior when approaching to the mesh resonance, where the phase between the incident electric field and the reflected one goes through a 180 deg shift. This phase shift

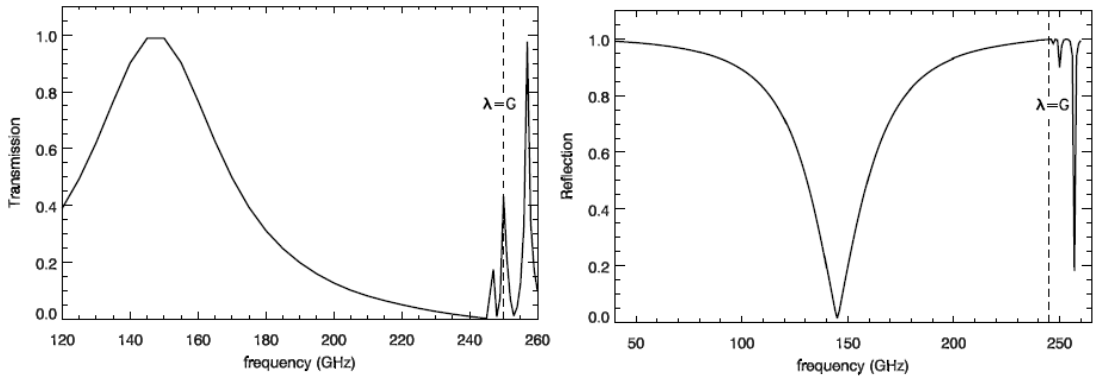

Figure 5.24. Transmission and reflection coefficients evaluated for the R-grid, as a function of the frequency.

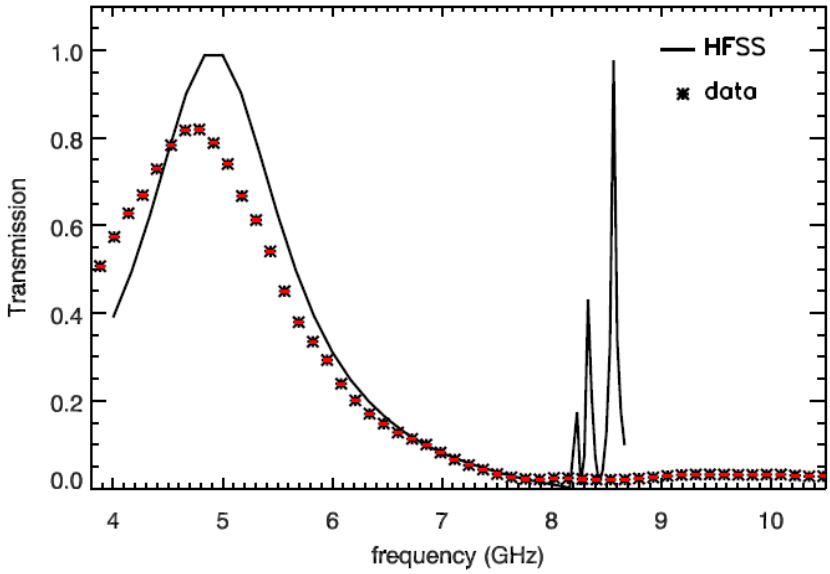

Figure 5.25. R-grid transmission coefficient derived by HFSS compared with the measured one.

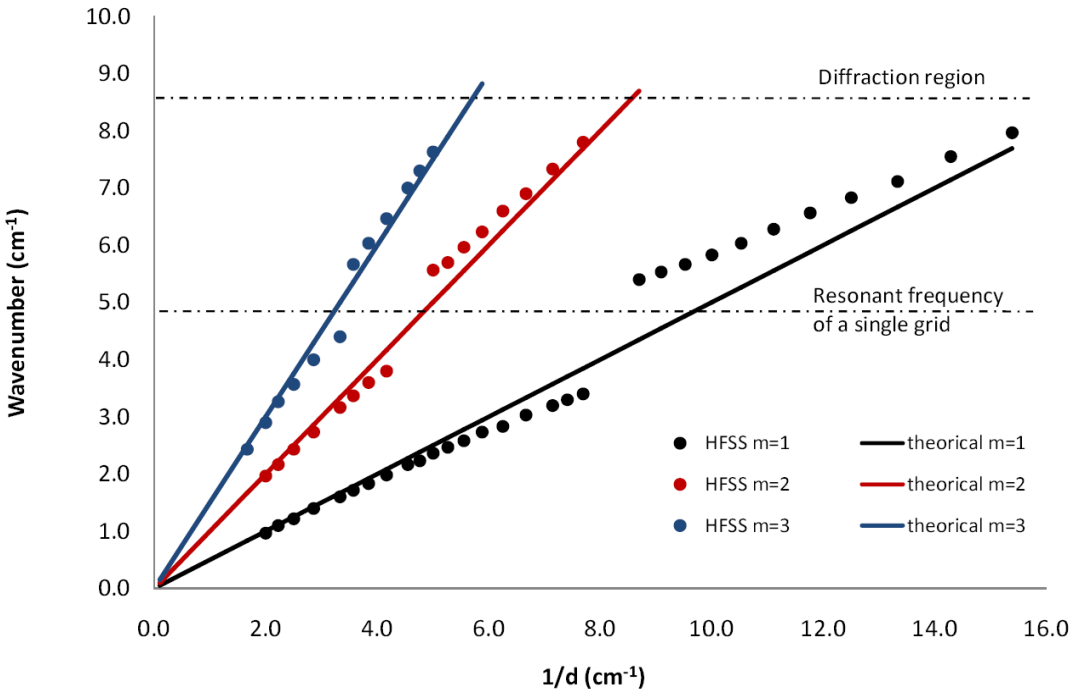

Figure 5.26. FP resonances wavenumber as a function of the inverse of the plates separation as evaluated by HFSS (dots) for the first three interference orders. The classical theory is shown with the three solid lines.

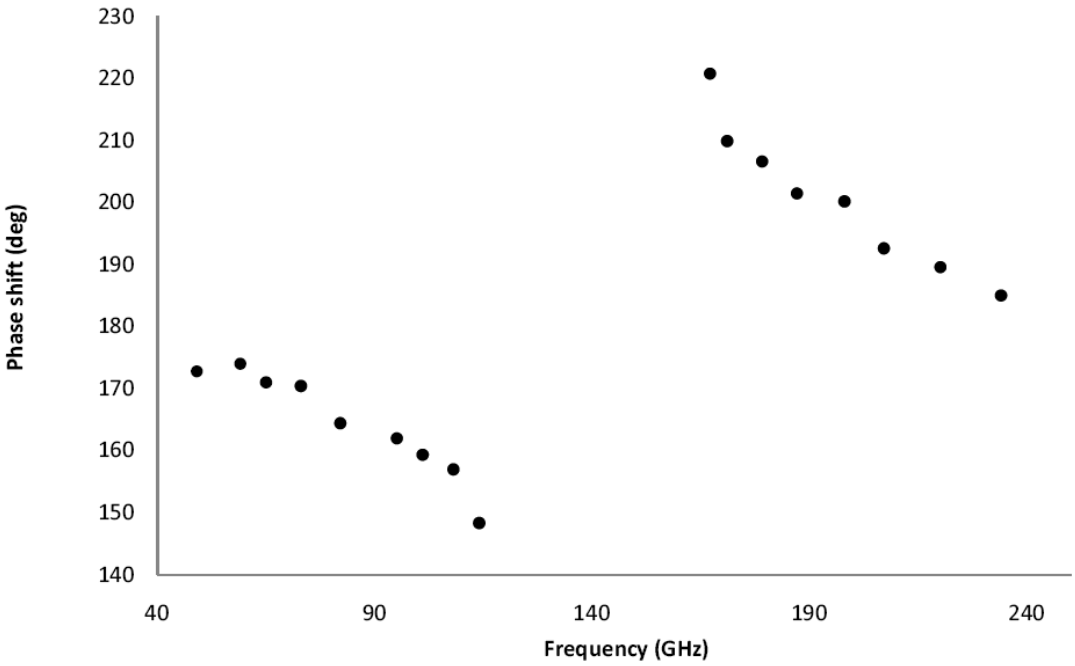

Figure 5.27. The phase shift on reflection as modeled by HFSS. The resonance of the mesh produces a jump from values lower then 180 deg to values higher then 180 deg. Asymptotically the phase shift approaches to 180 deg, reproducing the ideal mirror behavior.

changes the boundary conditions of the electric field, producing a displacement of the resonant frequency of the FPI (see Fig. 5.27). The deviation from the classical model recall the behavior of the transmission of the single mesh changing with frequency: at low frequencies the phase is close to 180 deg and the mesh is acting as an ideal mirror, allowing the cavity to support FPI modes. On resonance the array is totally transmissive then the phase change becomes 0 deg. Near the resonance FPI modes can not be distinguishable from the single mesh band. At high frequencies the phase becomes 180 deg and the FPI approaches again to the typical response but above 250 GHz diffraction take places. The mesh resonance is located where the phase jumps from values lower then 180 deg to higher ones. This means that the FPI cavity length can be assumed to be longer then the physical distance d at low frequencies and shorter above the resonance, due to the phase shift induced at each reflection by the mesh. As a consequence the FPI peaks are at frequencies lower then expected before the resonance and at higher frequencies above 150 GHz. This shift from the classical prediction turns out to be smaller and smaller going towards high orders.
The HFSS previsions are in agreement with the FPI resonances displacement measured for the second and the third order, shown in Table 5.3 (see Figs. 5.28).

The plot in Fig. 5.26 suggests two possible approaches: the first is working far from the resonance, where the phase shift is close to 180 deg and the peak position is in agreement with the classical theory; the second is working near the resonance,

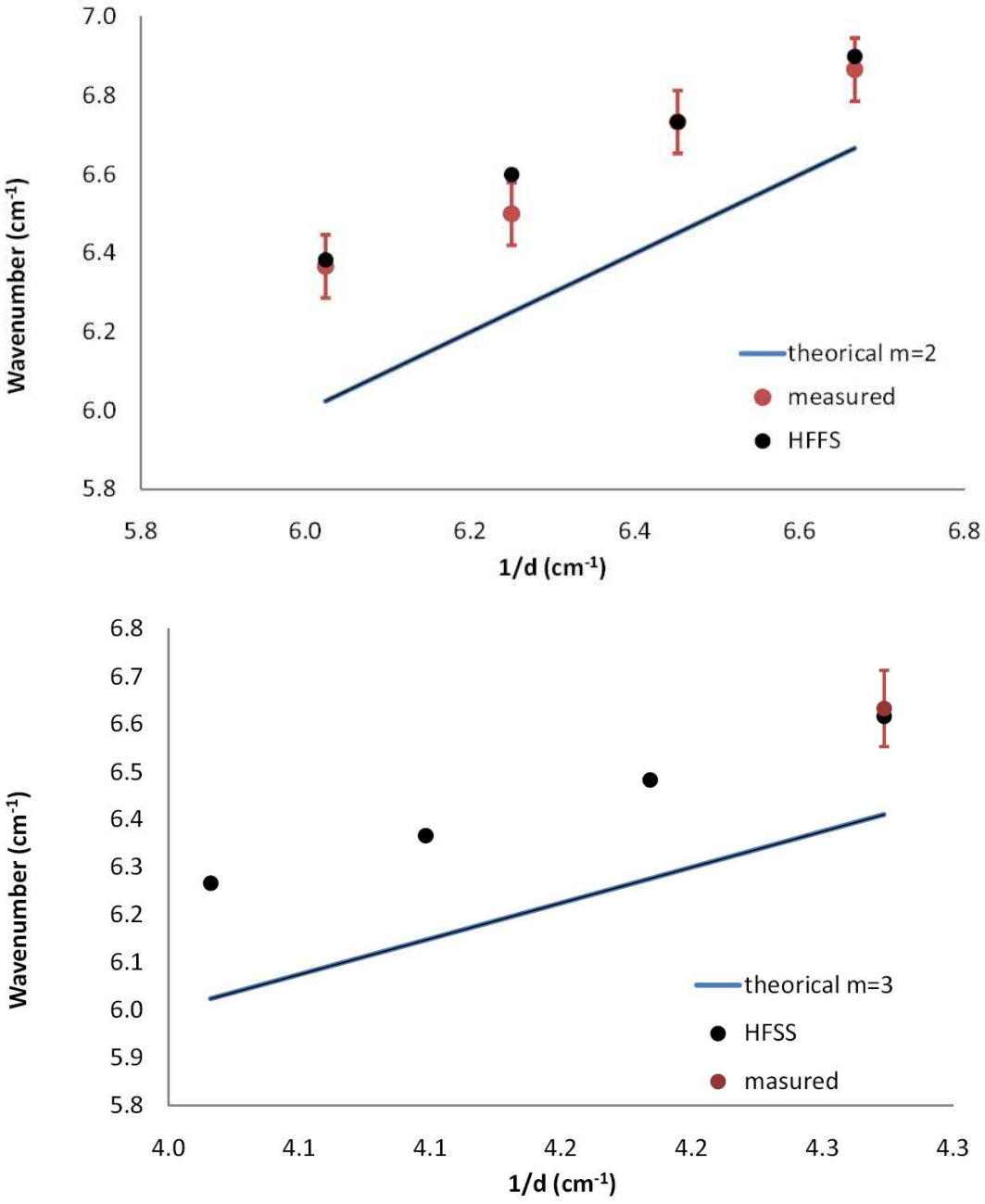

Figure 5.28. FP peaks wavenumber as a function of the inverse of the plates separation as evaluated by HFSS model (black dots) compared with measured values (red dots). The uncertainty is due to the spectral resolution of the Lamellar Grating. The classical trend is shown as the blue line. Top panel refers to m=2, while the bottom panel show third order results.

where the classical theory does not work adequately, and defining a new distance-frequency relation like the one in Eq. 4.6, by means of HFSS. In any case HFSS turns out to be an useful tool to predict and model all the non classical effects arising in a system of this kind.
In conclusion experimental results presented in Sec. 5.2, combined with HFSS models discussed in this Section, show that two cross-shaped metal grids can be adopted to realize a FPI. The non classical effects concerning this configuration can be fully predicted by HFSS simulations.
Anyway this kind of geometry is not the ideal solution if we consider the observational topics described in Chapter 1. In fact the measured profiles show that the efficiency of the FPI interferometer is affected by diffraction from 210 GHz and not from 250 GHz, as both the transmission line theory and HFSS would predict. The motivation of this behavior is still misunderstood and would need a careful characterization. In general the best solution is to work far from the resonance, where diffraction effects are negligible. In addition the experimental measurements have been performed only in the high frequency range, while low frequencies profiles could highlight the FPI response when the non classical effects are negligible so the cross-shaped meshes seem to be an ideal mirror. The next step will be to explore other mesh geometries focusing our attention on the inductive grid, the ideal solution to have a constant and high Finesse in the whole range of interest. Details of this solution are provided in the next section.

5.6 Future perspectives

As we discussed in Chapter 1, MAD spectroscopic capabilities can be achieved by means of a FPI operating in correspondence of the 220 GHz channel. The interferometer will be placed in a f/4 converging beam before the bolometer array, with an optical configuration that limits the spectral resolution given by the reflectivity of the plates alone. Anyway an high resolution SZ spectral sampling is not required and the high values of the reflectivity of the meshes are enough to balance the profile enlargement due to the incident beam convergence.
Laboratory tests on cross-shaped grids, employed as reflective elements of the FPI cavity, have shown the viability of the solution. In addition HFFS simulations reveal capable of predicting the electromagnetic response of the system, taking in account both diffraction and phase shift on reflection. The correspondence among experimental results and modeling is encouraging and new geometries can be explored in order to fulfill our goals, without the need to fabricate numerous samples. In particular we would prefer a frequency independent spectral response combined with diffraction effects far from the range of interest. Both of the two requirements are missing by 150 GHz resonant grids: diffraction begins at 210 GHz and the Finesse is strongly depending on frequency due to the resonance being close to the range of interest. The other two possible geometries discussed in Chapter 3 (see Fig. 4.5) are square openings (inductive, high pass) and free-standing squares (capacitive, low pass). C-grids are not the ideal solution because of diffraction effects below 300 GHz. Otherwise inductive meshes with resonance above 300 GHz (to avoid in-band diffraction effects), are the best solution in order to have reflection close to

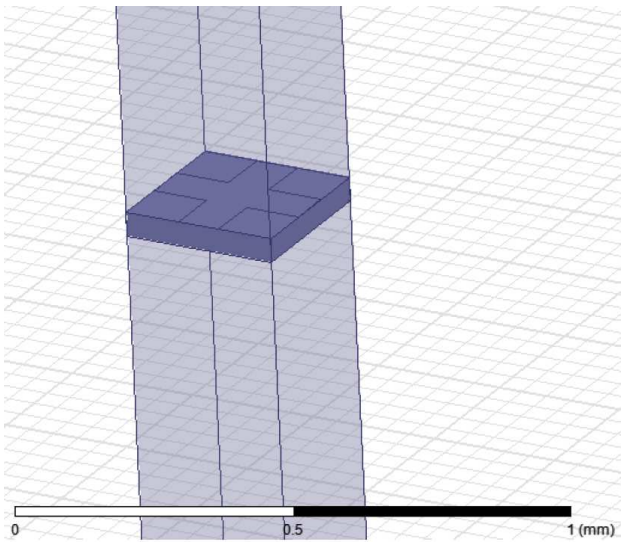

Figure 5.29. Elementary cell of the inductive grid geometry made of a copper film evaporated onto a thin PP substrate.

Table 5.4. I-grid geometries, with a/g ratio equal to 0.14, given by manufacturing constrains.

grid	g (mm)	2a (mm)
1	0.30	0.084
2	0.35	0.098
3	0.50	0.140

1 and steep slope only near the frequency cut-off. The mesh samples are designed as copper films evaporated onto a 47 μm thick polypropylene (PP) substrate (see Fig. 5.29), following the filter production technology of the Jodrell Bank Centre for Astrophysics (The University of Manchester), that will provide the final devices. The dielectric substrate assures good structural stability and flatness, introducing a little fraction of absorption. The electromagnetic response of three inductive grids geometries has been calculated with HFSS and it is shown in Fig. 5.30. The corresponding geometrical parameters are shown in Table 5.4. Polypropylene parameters needed to be set into HFSS library are the following [56]:

- Refraction index n = 1.5016
- Relative dielectric constant $\epsilon_r = 2.2549$
- Relative permeability $\mu_r = 1$
- Electric conductivity $\sigma = 0$
- Loss tangent $tan\delta = 0.00062$

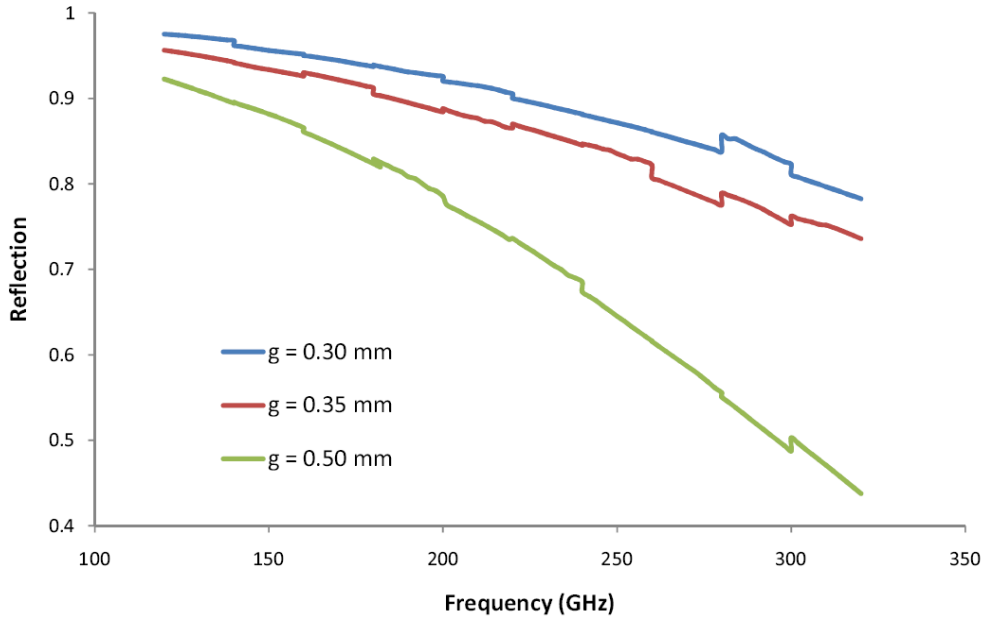

Figure 5.30. Simulated reflection coefficient spectra of the three inductive grids described in Table 5.4.

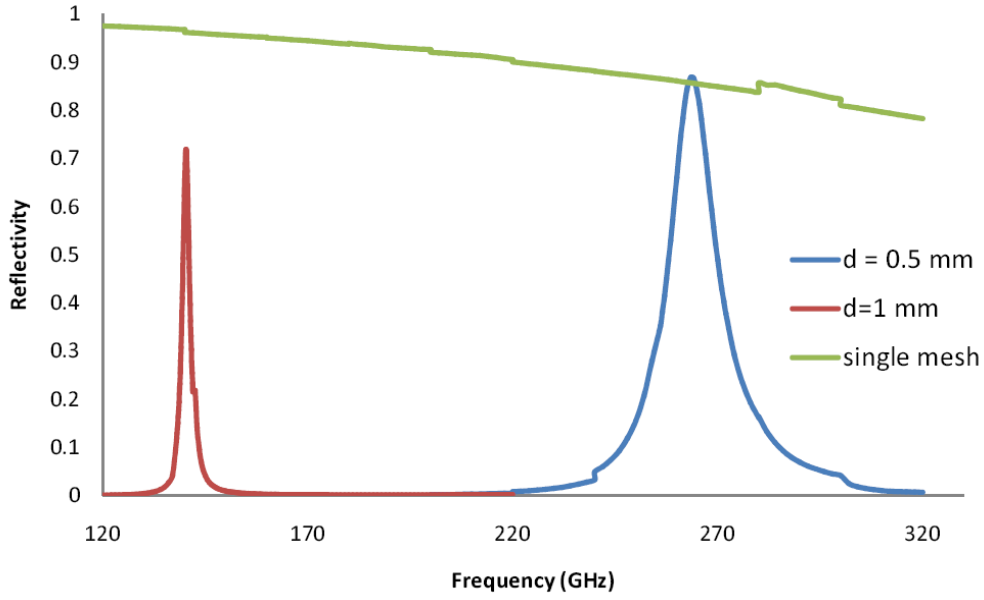

Figure 5.31. First order FPI peaks corresponding to the two extreme separation values. The cavity is made of two inductive grids with g=0.30. FWHM is 3 GHz at low frequencies and grows up to 15 GHz at high frequencies.

Irregularities of the reflection profiles in Fig. 5.30 are the result of convergence problems. They are only a computational effect that can be easily eliminated increasing the mesh refinement at the expense of a longer running time. Anyway the reflection increases for lower values of g, with the ratio a/g constant. In addition the grid 1 shows a 20 per cent variation in the range of interest and transmission always under 80 per cent. The best choice to perform a FPI simulation seems to be the grid 1, with the highest reflection coefficient. In the FPI HFSS model, the two identical I-grids have been placed with the two metallic crosses towards the cavity, and the spectral features of this system have been analyzed in the 120-300 range, varying the separation among the plates (see Fig. 5.31). The separation corresponding to the 220 GHz resonance is $d = 1$ mm, and the Airy profile FWHM is about 3 GHz (red line). Going towards high frequencies, the reflectivity of the single mesh goes down due to its high pass feature (green line), and the Finesse of the interferometer decreases. In fact the 270 GHz resonance has a FWHM of about 15 GHz (blue line). In addition 220 GHz resonance seems to be not correctly normalized but this is only a computational effect that can be eliminated reducing the convergence criterion at the expense of computational time. Even if high orders allow a reduction of the resolution power, they produce also a reduction of the FSR. Only first order has a FSR large enough to avoid secondary orders falling in the range of interest. Also in the case of the I-grids, the phase shift on reflection deviates from 180 deg, producing a frequency shift of the resonances, depending on frequency: at low frequencies, the reflectivity approaches to 1, the reflection phase shift is close to 180 deg and the metal mesh acts as an ideal mirror. Going towards high frequencies reflectivity decreases and the resonance shift becomes larger and larger. The main advantage of I-grids respect to the R-grids analyzed previously, is that the new resonant condition, including the dependence of ϕ_r on frequency, is linear. In Fig. 5.32 the wavenumber of the resonance frequency is plotted as a function of the inverse of the separation among the plates. The dots evaluated by HFSS deviates from the classical resonance condition (solid line) but they are well fitted by the line with the equation shown in the plot. This equation represent the new resonance condition instead of Eq. 4.6 given by the FPI classical approach. It allows to predict the position of the resonance given the plates separation, taking in account the phase shift on reflection. In Table 5.5 the values of the quantities plotted in Fig. 5.32 are shown. The values of ϕ_r corresponding to the four resonances, has been evaluated by means of Eq. 5.1. In summary HFSS previsions of the electromagnetic response of a FPI made of two identical I-grids with g=0.30 mm and a/g ratio equal to 0.14 shows encouraging results, that need to be confirmed by laboratory tests. The production of the two I-grids prototypes is on going and it consists on the photolithographic process to produce the mask with the required grid geometry and on the Copper evaporation on the thin polypropylene (PP) substrate mounted on a 20 cm diameter metallic ring. The experimental tests will be realized as soon as possible. On the other hand the scanning and tilting strategy need to be improved in order to arrange a new automatic system in the cryogenic environment of the MAD array of detectors. This system will have to reduce both alignment defects and lack of parallelism in order to improve the FPI performances. At the moment the two considered solutions are the ones proposed by the FIBRE experiment and SPIFI spectrometer but also other options need to be explored.

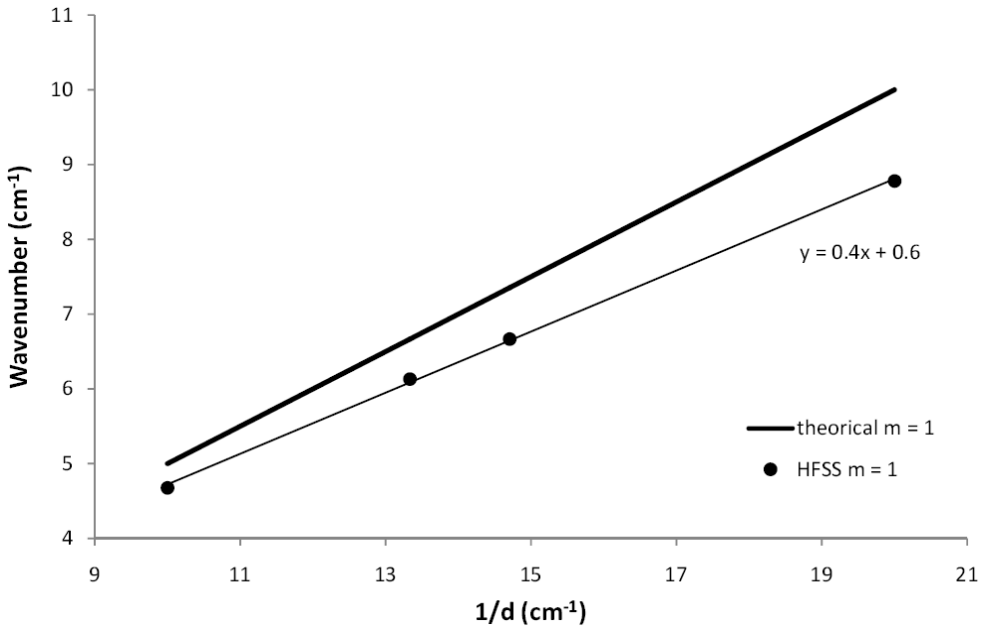

Figure 5.32. FP resonances wavenumber as a function of the inverse of the plates separation as evaluated by HFSS (dots) for m=1 and inductive meshes, compared with the classical theory linear trend (thick solid lines). Also the new resonant condition, including the dependence of ϕ_r on frequency, is linear.

Table 5.5. Frequency shift due to the phase shift on reflection ϕ_r measured for the first order, corresponding to data shown in Fig. 5.5.

d (mm)	$\nu_{teo}(GHz)$	$\nu_{HFSS}(GHz)$	$\phi_r(deg)$
0.50	300	264	25
0.68	221	200	16
0.75	200	184	14
1.00	150	140	10

Conclusions

The Sunyaev Zel'dovich effect is undoubtedly one of the best known cosmological probes, useful to study the evolution of structures in the Universe, the nature of dark energy and the physics that drives galaxies formation. The inverse Compton-scattering of CMB photons when they interact with the hot electrons of the intra-cluster medium in a cluster of galaxies boosts the energy of the CMB photons leading to a decrease in the intensity of the CMB in the Rayleigh Jeans region and an increase at higher microwave frequencies. Thus the modified spectrum cuts the original CMB Planck spectrum at the crossover frequency which is typically 217 GHz. On the other hand the kinematic SZ effect is the Doppler shift on the CMB spectrum, due to the line-of-sight peculiar velocity of the electrons with respect to the CMB rest frame. Accurate mapping of galaxy clusters at high redshift, combined to a spectral sampling of the SZ signal, allow to explore the thermodynamical history of the hot gas in clusters, determining the impact of nonthermal electron populations due to merging events, AGN feedback or cold fronts. To this purpose we have explored the Fabry-Perot interferometer configuration, mainly for its simplicity and compactness, to improve the capabilities of MAD (Multi Array of Detectors), a 4-channel photometer optimized for multi-frequency observation of SZ effect that will operate at Millimetre and Infrared Testagrigia Observatory (MITO), a 2.6-m in diameter telescope located in the Alps in Val d'Aosta (3480 m a.s.l.). The FPI provides MAD experiment with spectroscopic capabilities, combining the pre-existent photometric bands at 143, 270 and 345 GHz with a spectral sampling operating on the 220 GHz channel. In Chapter 1 we have shown how the FPI, reducing the instantaneous bandwidth, limits the photon background on the detectors and the photon noise mainly due to atmospheric emission for ground based measurements. Ground-based astronomical observations can be made only at the driest and most stable sites, like deserts or mountains summits, where a low vertical content of water vapor as well as high atmospheric emission stability are guaranteed. In Chapter 2 we have remarked that the high quality of ground-based cosmological and astrophysical observations can be reached only by a continuous monitoring of atmospheric performance on a wide spectral range. Even if there are several simulation codes able to provide synthetic atmospheric spectra, starting from the knowledge of climatic and geographic properties of the site of interest, they need in situ measurements for their validation. A spectrometer turns out to be the natural solution for sky monitoring over a wide spectral range. CASPER (Concordia Atmospheric SPectroscopy of Emitted Radiation) is the atmospheric spectrometer proposed to the P.N.R.A. (Programma Nazionale Ricerche in Antartide) devoted to the correction by atmospheric absorption of the astrophysical measurements realized by the

Concordia Italian-French station at Dome C, on the Antarctic plateau. Although Dome C is considered one of the best sites in the world to perform mm and submm observations, a wide spectral coverage transmission measurements campaign at Dome C was never carried out. In order to compensate for this lack a semi-empirical approach able to infer the transmission at Dome C generating ATM synthetic spectra derived by radiosounding data in the period from May 2005 to January 2007 has been illustrated. Excellent performance of Dome C transmission have been highlighted in the low frequency bands while large emission fluctuations have been pointed out in the high frequency bands. In addition, large timescales fluctuations of the atmospheric performance have been detected during two consecutive years. *Pwv* and transmission quartiles derived by the approach presented in this thesis have been validated by the comparison with other site-testing campaigns performed at Dome C during the last years also at different wavelengths.
From an experimental point of view the instrument CASPER2 has been developed specifically to record atmospheric emission spectra in the millimeter band for assisting cosmological observations with the 2.6-m in diameter Cassegrain telescope at MITO (see Chapter 3). Being an ancillary instrument, it is provided by an its own altazimuthal mount allowing to point the same direction of a telescope dedicated to cosmological millimeter observations from the ground. The spectra recorded during the observational campaign at MITO in July 2010 have highlighted the instrumental capabilities and will permit to validate the results of ATM code for MITO and consequently to infer the *pwv* value as derived by fit with synthetic spectra or by skydips.
Chapter 4 focused on the Fabry-Perot interferometer, considering all the practical limitations affecting the ideal behavior. The performance of the system made of two metal meshes in a resonant cavity configuration has been predicted by means of transmission line theory and the software HFSS. The effects on the spectral FPI transmission fringe pattern due to the converging beam and the lack of parallelism among the plates have been discussed. In addition since the array have a frequency dependent reflectivity and phase shift on reflection, they produce a shift in the Fabry-Perot resonant frequency from that predicted by the classical model. A preliminary investigation of information that could be potentially extracted from MAD+FP measurements of SZE towards cluster of galaxies has provided encouraging results. Anyway the analysis described in this thesis needs to be improved adding more realistic observational conditions, including all the sources of possible contamination and confusion from astronomical sources and atmospheric fluctuations, even considering the main instrumental effects.
A full characterization of the transmission profile of a FPI made of two resonant metal grids has been performed in Chapter 5. Three experimental setups have been employed. The first of them was devoted to the determination of the optical properties of the cross-shaped metal grid alone and the results have been compared both with transmission line previsions and HFSS results. The mesh resonance frequency predicted by Transmission Line Theory turned out to be 164 GHz, while HFFS simulated transmission spectrum showed a resonance close to 150 GHz. On the other hand the shift between the two resonances, experimental and modeled, was about 6 GHz, meaning that HFSS succeeded in taking in account of real effects much more then Transmission Line Theory. However the maximum of the measured

transmission was 20 per cent less then the unity, probably because of ohmic losses due to surface currents among the metal elements of the grid, neglected by HFSS. The HFFS transmission anomalies above 250 GHz, derived from diffraction effects, are not evident in the experimental data probably because of the convergence of the incident beam that damped the anomalies.
The last two experimental setups were employed for the measurement of the transmission profile of the prototype of FPI composed by two resonant grid. The FPI limitations connected to the convergence of the beam, the angle of incidence and the lack of parallelism among the two plates have been characterized. The next step will be the improvement of the scanning and tilting strategy, replacing the manual stage with an automatic system suitable to a cryogenic environment like the one in proximity of MAD array of detectors.
The resonant meshes adopted in this work were found to shift the frequency of the FPI modes due to the dependence of phase shift on reflection on frequency. The deviation from the classical model recalled the behavior of the transmission of the single mesh changing with frequency. This means that the FPI cavity length could be assumed to be longer then the physical distance at low frequencies and shorter above the resonance, due to the phase shift induced at each reflection by the mesh. As a consequence the FPI peaks were at frequencies lower then expected before the resonance and at higher frequencies above 150 GHz. The shift from the classical prediction turned out to be smaller and smaller going towards high orders. The HFSS previsions were in agreement with the FPI resonances displacement measured for the second and the third order.
Finally new geometries have been explored by means of HFSS in order to fulfill our goals, without the need to fabricate numerous samples. In particular the electromagnetic response of three inductive grids geometries has been calculated and two identical I-grids have been employed for a simulation of a FPI cavity. Also in this case, the phase shift on reflection deviated from 180 deg, producing a frequency shift of the resonances, depending on frequency. Anyway the main advantage of inductive grids respect to the resonant ones was that the new resonant condition, including the dependence of phase shift on frequency, turned out to be linear, then easy to be modeled.
The production of the two I-grids prototypes is on going and the experimental tests on the final arrays will be realized as soon as possible.

Conclusioni

L'effetto Sunyaev Zel'dovich (SZ) rappresenta indubbiamente uno degli strumenti cosmologici più potenti per lo studio della nascita e dell'evoluzione delle strutture che popolonano il nostro Universo. Esso consiste nell'effetto Compton inverso subito dai fotoni del fondo cosmico a microonde (CMB) ad opera degli elettroni altamente energetici contenuti all'interno degli ammassi di galassie (effetto SZ termico). Questa interazione determina una diminuzione di intensità di fotoni CMB nella regione di Rayleigh-Jeans dello spettro di corpo nero, e un corrispondente aumento ad alte frequenze, con una frequenza di taglio (*crossover*) tra i due regimi pari a 217 GHz. Se gli elettroni coinvolti nello scattering presentano una velocità peculiare rispetto ai fotoni incidenti, lo spettro CMB subirà uno spostamento per effetto Doppler (effetto SZ cinematico). Lo sforzo compiuto negli ultimi anni per realizzare misure di mappe millimetriche ad alta risoluzione angolare di ammassi di galssie è giustificato dal fatto che tali osservazioni permettono, in linea di principio, di ricostruire l'evoluzione e la dinamica del gas di elettroni fino ad alti redshift. Se opportunamente combinate ad un campionamento in frequenza del segnale SZ, tali osservazioni fornirebbero inoltre uno strumento insostituibile per la determinazione di tutti quei processi non termici di varia natura che influenzano lo stato termodinamico del mezzo intracluster.
In questo lavoro di tesi ho sviluppato un Interferometro Fabry-Perot (FPI) al fine di migliorare le potenzialità di MAD (Multi Array of Detectors), un fotometro a 4 canali ottimizzato per osservazioni multi-frequenza dell'effetto SZ che opererà presso MITO (Millimetre and Infrared Testagrigia Observatory), in Val d'Aosta a 3480 m di quota. Grazie a questa implementazione MAD sarà dotato di un spettrometro a modesta risoluzione in corrispondenza del canale a 220 GHz, che va ad aggiungersi alle tre bande fotometriche preesistenti a 143, 270 e 345 GHz. Nel Capitolo 1 è stato sottolineato il fatto che, essendo caratterizzato da una banda spettrale di qualche decina di GHz per ciascun elemento campionato, il FPI riduce sensibilmente il rumore fotonico sui rivelatori, associato principalemte all'emissione atmosferica nel caso di misure realizzate da terra. Uno studio preliminare delle prestazioni dello strumento MAD+FP ha fornito risultati incoraggianti ma l'analisi andrà implementata considerando condizioni osservative più realistiche, includendo tutte le forme di contaminazione di carattere astrofisico e strumentale.
Sebbene negli ultimi decenni gli esperimenti da pallone o da satellite abbiano ampiamente dimostrato le loro potenzialità, le limitazioni legate al peso, alle dimensioni del telescopio e l'accesso alla strumentazione in fase di misura, ostacolano sensibilmente lo sviluppo di grandi telescopi su pallone, satellite o aereo. La soluzione da terra appare l'unica al giorno d'oggi in grado di consentire la realizzazione di

telescopi ad alta risoluzione angolare a queste lunghezze d'onda.
Le osservazioni di natura astrofisica vanno effettuate nei siti più secchi e stabili, quali ad esempio regioni desertiche o ad alta quota, dove sono assicurati sia un basso contributo di vapore acqueo precipitabile, sia un'alta stabilità dell'emissione atmosferica. A questo proposito va sottolineato il fatto che un'alta qualità delle misure astrofisiche e cosmologiche da terra può essere raggiunta solo tramite un monitoraggio continuo delle performance atmosferiche su un ampio intervallo di frequenze. Pur disponendo di codici di simulazione in grado di produrre spettri atmosferici sintetici a partire dalle caratteristiche climatiche del sito d'interesse, essi richiedono comunque misure in situ per la loro validazione. Uno spettrometro costituisce la soluzione naturale a questa problematica. CASPER (Concordia Atmospheric SPectroscopy of Emitted Radiation) è lo spettrometro atmosferico proposto al P.N.R.A. (Programma Nazionale Ricerche in Antartide) dedicato alla correzione di misure astrofisiche dall'assorbimento atmosferico realizzate dalla stazione italo-francese Concordia, a Dome C, sul plateau Antartico. Sebbene Dome C sia considerato uno dei migliori siti al mondo in cui realizzare misure mm e sub-mm, una campagna continuativa di misure di trasmissione atmosferica su un ampio intervallo spettrale non è ancora stata mai effettuata. Per compensare questa mancanza nel Capitolo 2 abbiamo proposto un approccio semi-empirico in grado di ricostruire la trasmissione atmosferica a Dome C a partire da misure di radiosondaggi. Gli spettri sintetici generati mediante il modello ATM (Atmospheric Transmission at Microwaves) sono stati infatti ottenuti a partire dai dati relativi ai profili di temperatura, pressione ed umidità relativa misurati presso la stazione Concordia da Maggio 2005 a Gennaio 2007. Le statistiche di *pwv* e di trasmissione derivate in questo modo sono consistenti con le diverse campagne osservative di *site-testing* condotte a Dome C negli ultimi anni. L'analisi ha permesso di evidenziare le eccellenti prestazioni nelle bande a bassa frequenza e le ampie fluttuazioni presenti nelle finestre sub-millimetriche. Ampie fluttuazioni su grandi tempi scala sono state evidenziate confrontando le prestazioni corrispondenti allo stesso periodo dell'anno relativi a due anni consecutivi.
Dal punto di vista strumentale ho collaborato allo sviluppo dello spettrometro CASPER2, dedicato a misure di spettri atmosferici durante le osservazioni di carattere cosmologico realizzate a MITO (Capitolo 3). Essendo uno strumento ancillare, CASPER2 è dotato di una montatura alt-azimuthale propria, rendendo possibile il puntamento nella stessa direzione del telescopio dedicato a misure cosmologiche. Gli spettri di emissione atmosferica misurati durante le campagna osservativa a MITO del mese di Luglio 2010 hanno evidenziato le potenzialità dello strumento e, combinati alle stesse misure effettuate durante i diversi periodi dell'anno, permetteranno di validare il codice ATM per MITO.
Il Capitolo 4 ha riguardato prevalentemente la teoria classica dell'interferometro Fabry-Perot, considerando tutte quelle limitazioni pratiche che vanno a degradare le prestazioni ideali. La risposta in frequenza del sistema ottico costituito da due mesh metalliche in configurazione di cavità risonante è stata determinata sia tramite la teoria della linea di trasmissione, sia tramite il *software* HFSS. Sono stati inoltre trattati gli effetti relativi alla convergenza del fascio, così come quelli relativi all'assenza di mancanza di parallelismo tra le lamine. L'attenzione si è infine concentrata sullo spostamento in frequenza della risonanza del Fabry-Perot rispetto

a quella prevista dalla teoria classica, dovuto alla dipendenza dello sfasamento in riflessione di ciascuna mesh dalla frequenza.
La caratterizzazione completa del profilo di trasmissione associato al prototipo di FPI realizzato impiegando due mesh risonanti identiche è stata presentata nel Capitolo 5. Il primo dei tre setup sperimentali adottati a questo scopo ha permesso di misurare la risposta in frequenza della singola mesh, che successivamente è stata confrontata con i corrispondenti profili determinati tramite teoria della linea di trasmissione e HFSS. Mentre la risonanza prevista dalla teoria della linea di trasmissione è pari a 164 GHz, lo spettro della trasmissione simulato con HFSS ha evidenziato una risonanza a 150 GHz, discostato di soli 6 GHz dal valore misurato sperimentalmente. L'analisi mediante HFSS si è mostrata in grado di tenere in considerazione di diversi effetti molto più di quanto non sia in grado di fare la teoria della linea di trasmissione. Nonostante ciò il massimo di trasmissione misurato è risultato circa il 20 per cento in meno rispetto all'unità, probabilmente a causa di perdite ohmiche dovute a correnti superficiali originatesi tra gli elementi metallici della mesh, di cui HFSS non tiene in considerazione nel calcolo. Le anomalie nel profilo di trasmissione evidenziate oltre 250 GHz da HFSS sono da ricondursi a effetti diffrattivi che sperimentalmente non sono state rivelate, probabilmente a causa della convergenza del fascio incidente che potrebbe portare allo smorzamento tali anomalie. Gli altri due setup sperimentali hanno invece permesso di caratterizzare la risposta in frequenza del FPI in funzione sia della convergenza del fascio e del relativo angolo di incidenza, sia dell'inclinazione tra le lamine. Il prossimo passo consiterà nell'adottare un sistema di movimentazione meccanico che permetterà di automazzare sia la scansione che l'allineamento ottico dell'interferometro. Tale sistema di movimentazione andrà scelto anche in funzione del fatto che dovrà lavorare nell'ambiente criogenico in prossimità della matrice di rivelatori di MAD. Le misure di laboratorio hanno evidenziato lo spostamento in frequenza delle risonanze del FPI derivanti dalla non idealità dello sfasamento in riflessione di ciascuna mesh. A causa di questo effetto la lunghezza della cavità risonante appare maggiore (minore) della lunghezza effettiva a seconda che ci si trovi a frequenze minori (maggiori) della frequenza di risonanza della mesh. Le previsioni di HFSS sono in ottimo accordo con lo spostamento in frequenza misurato sperimentalmente. Questo ha permesso di utilizzare il *software* di simulazione per prevedere le prestazioni di tre diverse geometrie di mesh induttive, evitando i costi relativi alla produzione dei relativi prototipi. Anche nel caso di due mesh induttive in configurazione FPI lo sfasamento in riflessione introdotto per ciascuna riflessione della mesh determina uno spostamento in frequenza delle risonanze. Uno dei vantaggi principali correlati all'impiego di mesh induttive consiste nel fatto che l'andamento dello spostamento in frequenza in funzione della distanza tra le lamine risulta lineare. Al momento la produzione dei due prototipi è in corso e non appena sarà possibile si procederà con i test sperimentali relativi alla loro caratterizzazione.

Bibliography

[1] Ade, P. A. R., Pisano, G., Tucker, C., and Weaver, S. A review of metal mesh filters. In *Society of Photo-Optical Instrumentation Engineers (SPIE) Conference Series*, vol. 6275 of *Society of Photo-Optical Instrumentation Engineers (SPIE) Conference Series* (2006). doi:10.1117/12.673162.

[2] Allan, D. W. Statistics of atomic frequency standards. **54**.

[3] Allen, S. W., Evrard, A. E., and Mantz, A. B. Cosmological Parameters from Observations of Galaxy Clusters. ARA&A, **49** (2011), 409. arXiv:1103.4829, doi:10.1146/annurev-astro-081710-102514.

[4] Arnaud, J. A. and Pelow, F. A. Resonant-grid quasi-optical diplexers. *AT T Technical Journal*, **54** (1975), 263.

[5] Baker, E. A. M. and Walker, B. REVIEW ARTICLE: Fabry-Perot interferometers for use at submillimetre wavelengths. *Journal of Physics E Scientific Instruments*, **15** (1982), 25. doi:10.1088/0022-3735/15/1/003.

[6] Battistelli, E. S., et al. Cosmic Microwave Background Temperature at Galaxy Clusters. ApJ, **580** (2002), L101. arXiv:arXiv:astro-ph/0208027, doi:10.1086/345589.

[7] Battistelli, E. S., et al. Intensity and polarization of the atmospheric emission at millimetric wavelengths at Dome Concordia. MNRAS, **423** (2012), 1293. arXiv:1203.5615, doi:10.1111/j.1365-2966.2012.20951.x.

[8] Bennet, J. M. Precise Method for Measuring the Absolute Phase Change on Reflection. *Journal of the Optical Society of America (1917-1983)*, **56** (1966), 409.

[9] Birkinshaw, M. The Sunyaev-Zel'dovich effect. Phys. Rep., **310** (1999), 97. arXiv:arXiv:astro-ph/9808050, doi:10.1016/S0370-1573(98)00080-5.

[10] Bolton, D. The Computation of Equivalent Potential Temperature. *Monthly Weather Review*, **108** (1980), 1046. doi:10.1175/1520-0493(1980)108<1046:TCOEPT>2.0.CO;2.

[11] Bradford, C. M., Stacey, G. J., Swain, M. R., Nikola, T., Bolatto, A. D., Jackson, J. M., Savage, M. L., Davidson, J. A., and Ade, P. A. R. SPIFI: a direct-detection imaging spectrometer for submillimeter

wavelengths. Appl. Opt., **41** (2002), 2561. arXiv:arXiv:astro-ph/0205159, doi:10.1364/AO.41.002561.

[12] Brodwin, M., et al. SPT-CL J0546-5345: A Massive z = 1 Galaxy Cluster Selected Via the Sunyaev-Zel'dovich Effect with the South Pole Telescope. ApJ, **721** (2010), 90. arXiv:1006.5639, doi:10.1088/0004-637X/721/1/90.

[13] Buzi D. *Sviluppo di un interferometro Fabry-Perot per osservazioni cosmologiche in banda millimetrica da MITO.*

[14] Calisse, P. G., Ashley, M. C. B., Burton, M. G., Phillips, M. A., Storey, J. W. V., Radford, S. J. E., and Peterson, J. B. Submillimeter Site Testing at Dome C, Antarctica. PASA, **21** (2004), 256. doi:10.1071/AS03018.

[15] Carlstrom, J. E. Cosmology with the Sunyaev-Zel'dovich Effect. In *APS April Meeting Abstracts* (2002).

[16] Carlstrom, J. E., Holder, G. P., and Reese, E. D. Cosmology with the Sunyaev-Zel'dovich Effect. ARA&A, **40** (2002), 643. arXiv:arXiv:astro-ph/0208192, doi:10.1146/annurev.astro.40.060401.093803.

[17] Carlstrom, J. E., et al. The 10 Meter South Pole Telescope. PASP, **123** (2011), 568. arXiv:0907.4445, doi:10.1086/659879.

[18] Catalano, A., Conversi, L., De Gregori, S., De Petris, M., Lamagna, L., Maoli, R., Savini, G., Battistelli, E. S., and Orlando, A. A far infrared polarimeter. New A, **10** (2004), 79. arXiv:arXiv:astro-ph/0405399, doi:10.1016/j.newast.2004.05.002.

[19] Chamberlain, J. Phase modulation in far infrared (submillimetre-wave) interferometers. I - Mathematical formulation. *Infrared Physics*, **11** (1971), 25. doi:10.1016/0020-0891(71)90031-5.

[20] Chamberlain, J. and Gebbie, H. A. Phase modulation in far infrared (submillimetre-wave) interferometers. II - Fourier spectrometry and Terametrology. *Infrared Physics*, **11** (1971), 57. doi:10.1016/0020-0891(71)90032-7.

[21] Chen, C.-C. Transmission through a Conducting Screen Perforated Periodically with Apertures. *IEEE Transactions on Microwave Theory Techniques*, **18** (1970), 627. doi:10.1109/TMTT.1970.1127298.

[22] Comis B. *Scaling Relation between Sunyaev-Zel'dovich Effect Flux and Clusters of Galaxies Mass: Study of the Impact of Cool-Core Clusters* (2011).

[23] Coster, A. J., Niell, A. E., Solheim, F. S., Mendes, V. B., C., T. P., Buchmann, K. P., and Upham, C. A. Measurements of Precipitable Water Vapor by GPS, Radiosondes, and a Microwave Water Vapor Radiometer. In *Proceedings of the 9th International Technical Meeting of the Satellite Division*

of The Institute of Navigation (ION GPS 1996), Kansas City, MO, pp. 625–634 (1996).

[24] da Silva, A. C., Kay, S. T., Liddle, A. R., and Thomas, P. A. Hydrodynamical simulations of the Sunyaev-Zel'dovich effect: cluster scaling relations and X-ray properties. MNRAS, **348** (2004), 1401. arXiv:arXiv:astro-ph/0308074, doi:10.1111/j.1365-2966.2004.07463.x.

[25] De Bernardis, P., et al. SAGACE: the Spectroscopic Active Galaxies And Clusters Explorer. *ArXiv e-prints*, (2010). arXiv:1002.0867.

[26] De Gregori, S., De Petris, M., Decina, B., Lamagna, L., Pardo, J. R., Petkov, B., Tomasi, C., and Valenziano, L. Millimetre and submillimetre atmospheric performance at Dome C combining radiosoundings and ATM synthetic spectra. MNRAS, **425** (2012), 222. arXiv:1204.0975, doi:10.1111/j.1365-2966.2012.21430.x.

[27] De Petris, M., De Gregori, S., Decina, B., Lamagna, L., and Pardo, J. R. Atmospheric monitoring in the millimetre and submillimetre bands for cosmological observations: CASPER2. MNRAS, (2012), 328. arXiv:1211.2929, doi:10.1093/mnras/sts380.

[28] De Petris, M., et al. MITO Measurements of the Sunyaev-Zeldovich Effect in the Coma Cluster of Galaxies. ApJ, **574** (2002), L119. arXiv:arXiv:astro-ph/0203303, doi:10.1086/342418.

[29] De Petris, M., et al. CASPER: Concordia Atmospheric SPectroscopy of Emitted Radiation. In *EAS Publications Series* (edited by M. Giard, F. Casoli, & F. Paletou), vol. 14 of *EAS Publications Series*, pp. 233–238 (2005). doi:10.1051/eas:2005036.

[30] Decina B. *Caratterizzazione dello spettrometro atmosferico CASPER2.* (2009).

[31] Dempsey, J. T., Friberg, P., Jenness, T., Bintley, D., and Holland, W. S. Extinction correction and on-sky calibration of SCUBA-2. In *Society of Photo-Optical Instrumentation Engineers (SPIE) Conference Series*, vol. 7741 of *Society of Photo-Optical Instrumentation Engineers (SPIE) Conference Series* (2010). arXiv:1008.0890, doi:10.1117/12.856476.

[32] DePetris, M., et al. A ground-based experiment for CMBR anisotropy observations: MITO. New A Rev., **43** (1999), 297. doi:10.1016/S1387-6473(99)00023-8.

[33] Dicker, S. R., et al. MUSTANG: 90 GHz science with the Green Bank Telescope. In *Society of Photo-Optical Instrumentation Engineers (SPIE) Conference Series*, vol. 7020 of *Society of Photo-Optical Instrumentation Engineers (SPIE) Conference Series* (2008). arXiv:0907.1306, doi:10.1117/12.788361.

[34] Dobbs, M., et al. APEX-SZ first light and instrument status. New A Rev., **50** (2006), 960. doi:10.1016/j.newar.2006.09.029.

[35] Finkbeiner, D. P., Davis, M., and Schlegel, D. J. Extrapolation of Galactic Dust Emission at 100 Microns to Cosmic Microwave Background Radiation Frequencies Using FIRAS. ApJ, **524** (1999), 867. arXiv:arXiv:astro-ph/9905128, doi:10.1086/307852.

[36] Foley, R. J., et al. Discovery and Cosmological Implications of SPT-CL J2106-5844, the Most Massive Known Cluster at z 1. ApJ, **731** (2011), 86. arXiv:1101.1286, doi:10.1088/0004-637X/731/2/86.

[37] G. Hernï£¡ndez. *Fabry-Perot Interferometers*, vol. 15 (1988).

[38] Gervasi, M., de Bernardis, P., De Petris, M., Masi, S., and Pisano, G. Baffling and Shielding System for a Millimeter-Wave balloonborne Telescope. Appl. Opt., **37** (1998), 4277. doi:10.1364/AO.37.004277.

[39] Glenn, J., et al. Current status of Bolocam: a large-format millimeter-wave bolometer camera. In *Society of Photo-Optical Instrumentation Engineers (SPIE) Conference Series* (edited by T. G. Phillips and J. Zmuidzinas), vol. 4855 of *Society of Photo-Optical Instrumentation Engineers (SPIE) Conference Series*, pp. 30–40 (2003). doi:10.1117/12.459369.

[40] Goldsmith, Paul F. *Quasioptical systems : Gaussian beam, quasioptical propagation and application* (1998).

[41] Griffin, M., et al. Herschel-SPIRE: design, performance, and scientific capabilities. In *Society of Photo-Optical Instrumentation Engineers (SPIE) Conference Series*, vol. 6265 of *Society of Photo-Optical Instrumentation Engineers (SPIE) Conference Series* (2006). doi:10.1117/12.670783.

[42] Hanany, S., Niemack, M., and Page, L. CMB Telescopes and Optical Systems. *ArXiv e-prints*, (2012). arXiv:1206.2402.

[43] Hand, N., et al. Evidence of Galaxy Cluster Motions with the Kinematic Sunyaev-Zel'dovich Effect. *Physical Review Letters*, **109** (2012), 041101. arXiv:1203.4219, doi:10.1103/PhysRevLett.109.041101.

[44] Harris, F. J. On the Use of Windows for Harmonic Analysis with the Discrete Fourier Transform. *IEEE Proceedings*, **66** (1978), 51.

[45] Hincks, A. D., et al. The Atacama Cosmology Telescope (ACT): Beam Profiles and First SZ Cluster Maps. ApJS, **191** (2010), 423. arXiv:0907.0461, doi:10.1088/0067-0049/191/2/423.

[46] Holland, W. S., et al. SCUBA: a common-user submillimetre camera operating on the James Clerk Maxwell Telescope. MNRAS, **303** (1999), 659. arXiv:arXiv:astro-ph/9809122, doi:10.1046/j.1365-8711.1999.02111.x.

[47] Holzapfel, W. L., Arnaud, M., Ade, P. A. R., Church, S. E., Fischer, M. L., Mauskopf, P. D., Rephaeli, Y., Wilbanks, T. M., and Lange, A. E. Measurement of the Hubble Constant from X-Ray and 2.1 Millimeter Observations of Abell 2163. ApJ, **480** (1997), 449. arXiv:arXiv:astro-ph/9702224, doi:10.1086/303979.

[48] Hooberman B. *Everything You Ever Wanted to Know About Frequency-Selective Surface Filters but Were Afraid to Ask.*

[49] Hudson, S. R., Town, M. S., Walden, V. P., and Warren, S. G. Temperature, Humidity, and Pressure Response of Radiosondes at Low Temperatures. *Journal of Atmospheric and Oceanic Technology*, **21** (2004), 825. doi:10.1175/1520-0426(2004)021<0825:THAPRO>2.0.CO;2.

[50] Kashlinsky, A., Atrio-Barandela, F., and Ebeling, H. Measuring the Dark Flow with Public X-ray Cluster Data. ApJ, **732** (2011), 1. arXiv:1012.3214, doi:10.1088/0004-637X/732/1/1.

[51] Kay, S. T., Powell, L. C., Liddle, A. R., and Thomas, P. A. The Sunyaev-Zel'dovich temperature of the intracluster medium. MNRAS, **386** (2008), 2110. arXiv:0706.3668, doi:10.1111/j.1365-2966.2008.13183.x.

[52] Keisler, R. The Statistical Significance of the "Dark Flow". ApJ, **707** (2009), L42. arXiv:0910.4233, doi:10.1088/0004-637X/707/1/L42.

[53] Knudtson, J. T., Levy, D. S., and Herr, K. C. Electronically tunable, first-order fabry-peï£¡rot infrared filter. *Optical Engineering*, **35** (1996), 2313. Available from: +http://dx.doi.org/10.1117/1.600806, doi:10.1117/1.600806.

[54] Lamagna, L., de Petris, M., Melchiorri, F., Battistelli, E., de Grazia, M., Luzzi, G., Orlando, A., and Savini, G. MAD-4-MITO, a multi array of detectors for ground-based mm/submm SZ observations. In *Experimental Cosmology at Millimetre Wavelengths* (edited by M. de Petris and M. Gervasi), vol. 616 of *American Institute of Physics Conference Series*, pp. 92–96 (2002). arXiv:arXiv:astro-ph/0203427, doi:10.1063/1.1475609.

[55] Lamarre, J. M., et al. First Measurement of the Submillimeter Sunyaev-Zeldovich Effect. ApJ, **507** (1998), L5. arXiv:arXiv:astro-ph/9806128, doi:10.1086/311678.

[56] Lamb, J. W. Miscellaneous data on materials for millimetre and submillimetre optics. *International Journal of Infrared and Millimeter Waves*, **17** (1996), 1997. doi:10.1007/BF02069487.

[57] Lawrence, J. S. Infrared and Submillimeter Atmospheric Characteristics of High Antarctic Plateau Sites. PASP, **116** (2004), 482. doi:10.1086/420757.

[58] Lee, J. Y., Hahn, J. W., and Lee, H.-W. Spatiospectral transmission of a plane-mirror Fabry-Perot interferometer with nonuniform finite-size diffraction beam illuminations. *Journal of the Optical Society of America A*, **19** (2002), 973. doi:10.1364/JOSAA.19.000973.

[59] Lee, S.-W., Zarrillo, G., and Law, C.-L. Simple formulas for transmission through periodic metal grids or plates. *IEEE Transactions on Antennas and Propagation*, **30** (1982), 904. doi:10.1109/TAP.1982.1142923.

[60] Leifeste, G. T., Earley, L. M., Swegle, J. A., Poukey, J. W., Miller, R. B., Crist, C. E., Wharton, C. B., and Ballard, W. P. Ku 2010;band radiation produced by a relativistic backward wave oscillator. *Journal of Applied Physics*, **59** (1986), 1366 . doi:10.1063/1.336531.

[61] Luers, J. K. Temperature Error of the Vaisala RS90 Radiosonde. *Journal of Atmospheric and Oceanic Technology*, **14** (1997), 1520. doi:10.1175/1520-0426(1997)014<1520:TEOTVR>2.0.CO;2.

[62] Luers, J. K. and Eskridge, R. E. Temperature Corrections for the VIZ and Vaisala Radiosondes. *Journal of Applied Meteorology*, **34** (1995), 1241. doi:10.1175/1520-0450(1995)034<1241:TCFTVA>2.0.CO;2.

[63] Luzzi, G., Shimon, M., Lamagna, L., Rephaeli, Y., De Petris, M., Conte, A., De Gregori, S., and Battistelli, E. S. Redshift Dependence of the Cosmic Microwave Background Temperature from Sunyaev-Zeldovich Measurements. ApJ, **705** (2009), 1122. arXiv:0909.2815, doi:10.1088/0004-637X/705/2/1122.

[64] Mak, D. S. Y., Pierpaoli, E., and Osborne, S. J. Measuring Bulk Flow of Galaxy Clusters Using Kinematic Sunyaev-Zeldovich Effect: Prediction for Planck. ApJ, **736** (2011), 116. arXiv:1101.1581, doi:10.1088/0004-637X/736/2/116.

[65] Marriage, T. A., et al. The Atacama Cosmology Telescope: Sunyaev-Zel'dovich-Selected Galaxy Clusters at 148 GHz in the 2008 Survey. ApJ, **737** (2011), 61. arXiv:1010.1065, doi:10.1088/0004-637X/737/2/61.

[66] Marsden, G., et al. BLAST: Resolving the Cosmic Submillimeter Background. ApJ, **707** (2009), 1729. arXiv:0904.1205, doi:10.1088/0004-637X/707/2/1729.

[67] Masi, S., et al. OLIMPO. Mem. Soc. Astron. Italiana, **79** (2008), 887.

[68] Matsuo, H., Sakamoto, A., and Matsushita, S. FTS Measurements of Submillimeter-Wave Atmospheric Opacity at Pampa la Bola. PASJ, **50** (1998), 359.

[69] Matsushita, S., Matsuo, H., Pardo, J. R., and Radford, S. J. E. FTS Measurements of Submillimeter-Wave Atmospheric Opacity at Pampa la Bola II : Supra-Terahertz Windows and Model Fitting. PASJ, **51** (1999), 603.

[70] Menanteau, F., et al. The Atacama Cosmology Telescope: ACT-CL J0102-4915 "El Gordo," a Massive Merging Cluster at Redshift 0.87. ApJ, **748** (2012), 7. arXiv:1109.0953, doi:10.1088/0004-637X/748/1/7.

[71] Mielke, S. L., Ryan, R. E., Hilgeman, T., Lesyna, L., Madonna, R. G., and Nostrand, W. C. V. Measurements of the phase shift on reflection for low-order infrared fabry-perot interferometer dielectric stack mirrors. *Appl. Opt.*, **36** (1997), 8139. Available from: http://ao.osa.org/abstract.cfm?URI=ao-36-31-8139, doi:10.1364/AO.36.008139.

[72] Miloshevich, L. M., Paukkunen, A., Vömel, H., and Oltmans, S. J. Development and Validation of a Time-Lag Correction for Vaisala Radiosonde Humidity Measurements. *Journal of Atmospheric and Oceanic Technology*, **21** (2004), 1305. doi:10.1175/1520-0426(2004)021<1305:DAVOAT>2.0.CO;2.

[73] Miloshevich, L. M., Vömel, H., Paukkunen, A., Heymsfield, A. J., and Oltmans, S. J. Characterization and Correction of Relative Humidity Measurements from Vaisala RS80-A Radiosondes at Cold Temperatures. *Journal of Atmospheric and Oceanic Technology*, **18** (2001), 135. doi:10.1175/1520-0426(2001)018<0135:CACORH>2.0.CO;2.

[74] Miloshevich, L. M., Vömel, H., Whiteman, D. N., Lesht, B. M., Schmidlin, F. J., and Russo, F. Absolute accuracy of water vapor measurements from six operational radiosonde types launched during AWEX-G and implications for AIRS validation. *Journal of Geophysical Research (Atmospheres)*, **111** (2006), D09S10. doi:10.1029/2005JD006083.

[75] Minier, V., et al. Submm/FIR Astronomy in Antarctica: Potential for a large telescope facility. In *EAS Publications Series* (edited by H. Zinnecker, N. Epchtein, & H. Rauer), vol. 33 of *EAS Publications Series*, pp. 21–40 (2008). arXiv:0805.2487, doi:10.1051/eas:0833005.

[76] Monfardini, A., et al. A Dual-band Millimeter-wave Kinetic Inductance Camera for the IRAM 30 m Telescope. ApJS, **194** (2011), 24. arXiv:1102.0870, doi:10.1088/0067-0049/194/2/24.

[77] Morandi, A., Nagai, D., and Cui, W. Reconstructing three-dimensional parameters of galaxy clusters via multifrequency SZ observations. *ArXiv e-prints*, (2012). arXiv:1211.7096.

[78] N. Marcuvitz. *Waveguide Handbook* (1951).

[79] Netterfield, C. B., et al. A Measurement by BOOMERANG of Multiple Peaks in the Angular Power Spectrum of the Cosmic Microwave Background. ApJ, **571** (2002), 604. arXiv:arXiv:astro-ph/0104460, doi:10.1086/340118.

[80] Osborne, S. J., Mak, D. S. Y., Church, S. E., and Pierpaoli, E. Measuring the Galaxy Cluster Bulk Flow from WMAP Data. ApJ, **737** (2011), 98. arXiv:1011.2781, doi:10.1088/0004-637X/737/2/98.

[81] Paine, S., Blundell, R., Papa, D. C., Barrett, J. W., and Radford, S. J. E. A Fourier Transform Spectrometer for Measurement of Atmo-

spheric Transmission at Submillimeter Wavelengths. PASP, **112** (2000), 108. doi:10.1086/316497.

[82] Pajot, F. P., et al. Design and performances of a cryogenic Fabry-Perot for submillimeter astronomy. In *Society of Photo-Optical Instrumentation Engineers (SPIE) Conference Series* (edited by J. B. Heaney and L. G. Burriesci), vol. 5172 of *Society of Photo-Optical Instrumentation Engineers (SPIE) Conference Series*, pp. 13–20 (2003). doi:10.1117/12.506858.

[83] Pardo, J. R., Cernicharo, J., and Serabyn, E. Atmospheric transmission at microwaves (ATM): an improved model for millimeter/submillimeter applications. *IEEE Transactions on Antennas and Propagation*, **49** (2001), 1683. doi:10.1109/8.982447.

[84] Peterson, D. B. and Pickett, H. M. Cryogenic far-infrared Fabry-Perot etalon. Appl. Opt., **30** (1991), 4493. doi:10.1364/AO.30.004493.

[85] Peterson, J. B., Radford, S. J. E., Ade, P. A. R., Chamberlin, R. A., O'Kelly, M. J., Peterson, K. M., and Schartman, E. Stability of the Submillimeter Brightness of the Atmosphere above Mauna Kea, Chajnantor, and the South Pole. PASP, **115** (2003), 383. arXiv:arXiv:astro-ph/0211134, doi:10.1086/368101.

[86] Pilbratt, G. L., et al. Herschel Space Observatory. An ESA facility for far-infrared and submillimetre astronomy. A&A, **518** (2010), L1. arXiv:1005.5331, doi:10.1051/0004-6361/201014759.

[87] Pisano, G., Ade, P. A. R., and Weaver, S. Polarisation effects investigations in quasi-optical metal grid filters. *Infrared Physics and Technology*, **48** (2006), 89. doi:10.1016/j.infrared.2005.04.004.

[88] Pisareva, N. A. and Frudko, T. F. Intensity distribution from a Fabry-Perot interferometer with nonparallel plates. *Journal of Applied Spectroscopy*, **35** (1981), 1168. doi:10.1007/BF00605670.

[89] Planck Collaboration, et al. Planck early results. I. The Planck mission. A&A, **536** (2011), A1. arXiv:1101.2022, doi:10.1051/0004-6361/201116464.

[90] Planck Collaboration, et al. Planck early results. VIII. The all-sky early Sunyaev-Zeldovich cluster sample. A&A, **536** (2011), A8. arXiv:1101.2024, doi:10.1051/0004-6361/201116459.

[91] Radford, S. J. and Holdaway, M. A. Atmospheric conditions at a site for submillimeter-wavelength astronomy. In *Society of Photo-Optical Instrumentation Engineers (SPIE) Conference Series* (edited by T. G. Phillips), vol. 3357 of *Society of Photo-Optical Instrumentation Engineers (SPIE) Conference Series*, pp. 486–494 (1998).

[92] Reichardt, C. L., et al. Galaxy clusters discovered via the Sunyaev-Zel'dovich effect in the first 720 square degrees of the South Pole Telescope survey. *ArXiv e-prints*, (2012). arXiv:1203.5775.

[93] Renk, K. F. and Genzel, L. Interference filters and fabry-perot interferometers for the far infrared. *Appl. Opt.*, **1** (1962), 643. Available from: http://ao.osa.org/abstract.cfm?URI=ao-1-5-643, doi:10.1364/AO.1.000643.

[94] Rephaeli, Y. Comptonization Of The Cosmic Microwave Background: The Sunyaev-Zeldovich Effect. ARA&A, **33** (1995), 541. doi:10.1146/annurev.aa.33.090195.002545.

[95] Ruze, J. Antenna Tolerance Theory – A Review. *IEEE Proceedings*, **54** (1966), 633.

[96] Schaffer, K. K., et al. The First Public Release of South Pole Telescope Data: Maps of a 95 deg^2 Field from 2008 Observations. ApJ, **743** (2011), 90. arXiv:1111.7245, doi:10.1088/0004-637X/743/1/90.

[97] Schieder, R. and Kramer, C. Optimization of heterodyne observations using Allan variance measurements. A&A, **373** (2001), 746. arXiv:arXiv:astro-ph/0105071, doi:10.1051/0004-6361:20010611.

[98] Sehgal, N., Bode, P., Das, S., Hernandez-Monteagudo, C., Huffenberger, K., Lin, Y.-T., Ostriker, J. P., and Trac, H. Simulations of the Microwave Sky. ApJ, **709** (2010), 920. arXiv:0908.0540, doi:10.1088/0004-637X/709/2/920.

[99] Sehgal, N., Kosowsky, A., and Holder, G. Constrained Cluster Parameters from Sunyaev-Zel'dovich Observations. ApJ, **635** (2005), 22. arXiv:arXiv:astro-ph/0504274, doi:10.1086/497258.

[100] Sehgal, N., Trac, H., Huffenberger, K., and Bode, P. Microwave Sky Simulations and Projections for Galaxy Cluster Detection with the Atacama Cosmology Telescope. ApJ, **664** (2007), 149. arXiv:arXiv:astro-ph/0612140, doi:10.1086/518880.

[101] Shimon, M. and Rephaeli, Y. Cosmic Microwave Background Comptonization by Energetic Nonthermal Electrons in Clusters of Galaxies. ApJ, **575** (2002), 12. doi:10.1086/341268.

[102] Sifon, C., et al. The Atacama Cosmology Telescope: Dynamical Masses and Scaling Relations for a Sample of Massive Sunyaev-Zel'dovich Effect Selected Galaxy Clusters. *ArXiv e-prints*, (2012). arXiv:1201.0991.

[103] Siringo, G., et al. The Large APEX BOlometer CAmera LABOCA. A&A, **497** (2009), 945. arXiv:0903.1354, doi:10.1051/0004-6361/200811454.

[104] Spelman, J., Skrien, S., and Parker, T. E. Design Methodology for a Fabry-Perot Interferometer used as a Concentration Sensor. Appl. Opt., **41** (2002), 2847. doi:10.1364/AO.41.002847.

[105] Stalder, B., et al. SPT-CL J0205-5829: A z = 1.32 Evolved Massive Galaxy Cluster in the South Pole Telescope Sunyaev-Zel'dovich Effect Survey. *ArXiv e-prints*, (2012). arXiv:1205.6478.

[106] Sunyaev, R. A. and Zeldovich, Y. B. The Observations of Relic Radiation as a Test of the Nature of X-Ray Radiation from the Clusters of Galaxies. *Comments on Astrophysics and Space Physics*, **4** (1972), 173.

[107] Swain, M. R., Bradford, C. M., Stacey, G. J., Bolatto, A. D., Jackson, J. M., Savage, M. L., and Davidson, J. A. Design of the South Pole imaging Fabry-Perot interferometer (SPIFI). In *Society of Photo-Optical Instrumentation Engineers (SPIE) Conference Series* (edited by A. M. Fowler), vol. 3354 of *Society of Photo-Optical Instrumentation Engineers (SPIE) Conference Series*, pp. 480–492 (1998).

[108] Swetz, D. S., et al. Overview of the Atacama Cosmology Telescope: Receiver, Instrumentation, and Telescope Systems. ApJS, **194** (2011), 41. arXiv:1007.0290, doi:10.1088/0067-0049/194/2/41.

[109] The Planck Collaboration. The Scientific Programme of Planck. *ArXiv Astrophysics e-prints*, (2006). arXiv:arXiv:astro-ph/0604069.

[110] Tomasi, C., Cacciari, A., Vitale, V., Lupi, A., Lanconelli, C., Pellegrini, A., and Grigioni, P. Mean vertical profiles of temperature and absolute humidity from a 12-year radiosounding data set at Terra Nova Bay (Antarctica). *Atmospheric Research*, **71** (2004), 139. doi:10.1016/j.atmosres.2004.03.009.

[111] Tomasi, C., Petkov, B., Benedetti, E., Valenziano, L., and Vitale, V. Analysis of a 4 year radiosonde data set at Dome C for characterizing temperature and moisture conditions of the Antarctic atmosphere. *Journal of Geophysical Research (Atmospheres)*, **116** (2011), D15304. doi:10.1029/2011JD015803.

[112] Tomasi, C., Petkov, B., Dinelli, B. M., Castelli, E., Arnone, E., and Papandrea, E. Monthly mean vertical profiles of pressure, temperature and water vapour volume mixing ratio in the polar stratosphere and low mesosphere from a multi-year set of MIPAS-ENVISAT limb-scanning measurements. *Journal of Atmospheric and Solar-Terrestrial Physics*, **73** (2011), 2237. doi:10.1016/j.jastp.2011.06.018.

[113] Tomasi, C., et al. Characterization of the atmospheric temperature and moisture conditions above Dome C (Antarctica) during austral summer and fall months. *Journal of Geophysical Research (Atmospheres)*, **111** (2006), D20305. doi:10.1029/2005JD006976.

[114] Tremblin, P., Schneider, N., Minier, V., Durand, G. A., and Urban, J. Worldwide site comparison for submillimetre astronomy. *ArXiv e-prints*, (2012). arXiv:1210.4930.

[115] Tremblin, P., et al. Site testing for submillimetre astronomy at Dome C, Antarctica. A&A, **535** (2011), A112. arXiv:1110.4311, doi:10.1051/0004-6361/201117345.

[116] Turner, D. D., Lesht, B. M., Clough, S. A., Liljegren, J. C., Revercomb, H. E., and Tobin, D. C. Dry Bias and Variability in Vaisala RS80-H Radiosondes: The ARM Experience. *Journal of Atmospheric and Oceanic Technology*, **20** (2003), 117. doi:10.1175/1520-0426(2003)020<0117:DBAVIV>2.0.CO;2.

[117] Ulrich, R. Far-infrared properties of metallic mesh and its complementary structure. *Infrared Physics*, **7** (1967), 37. doi:10.1016/0020-0891(67)90028-0.

[118] Urban, J., Baron, P., Lautiï£¡, N., Schneider, N., Dassas, K., Ricaud, P., and Noï£¡, J. D. L. Moliere (v5): a versatile forward- and inversion model for the millimeter and sub-millimeter wavelength range. *Journal of Quantitative Spectroscopy and Radiative Transfer*, **83** (2004), 529 . Available from: http://www.sciencedirect.com/science/article/pii/S0022407303001043, doi:10.1016/S0022-4073(03)00104-3.

[119] Valenziano, L. and Dall'Oglio, G. Millimetre astronomy from the High Antarctic Plateau: Site testing at Dome C. PASA, **16** (1999), 167. arXiv:arXiv:astro-ph/9905105.

[120] Vanderlinde, K., et al. Galaxy Clusters Selected with the Sunyaev-Zel'dovich Effect from 2008 South Pole Telescope Observations. ApJ, **722** (2010), 1180. arXiv:1003.0003, doi:10.1088/0004-637X/722/2/1180.

[121] Vargas-Rodriguez, E., Rutt, H. N., Rojas-Laguna, R., and Alvarado-Mendez, E. Calibration of a gas sensor based on cross-correlation spectroscopy. *Journal of Optics A: Pure and Applied Optics*, **10** (2008), 104018. doi:10.1088/1464-4258/10/10/104018.

[122] Voit, G. M. Tracing cosmic evolution with clusters of galaxies. *Reviews of Modern Physics*, **77** (2005), 207. arXiv:arXiv:astro-ph/0410173, doi:10.1103/RevModPhys.77.207.

[123] Wang, J., Cole, H. L., Carlson, D. J., Miller, E. R., Beierle, K., Paukkunen, A., and Laine, T. K. Corrections of Humidity Measurement Errors from the Vaisala RS80 Radiosonde Application to TOGA COARE Data. *Journal of Atmospheric and Oceanic Technology*, **19** (2002), 981. doi:10.1175/1520-0426(2002)019<0981:COHMEF>2.0.CO;2.

[124] Ward-Thompson, D., et al. First ground-based 200-μm observing with THUMPER on JCMT - sky characterization and planet maps. MNRAS, **364** (2005), 843. arXiv:arXiv:astro-ph/0509674, doi:10.1111/j.1365-2966.2005.09625.x.

[125] Wiedner, M., Hills, R., and Pardo-Carrión, J. 183 GHz water vapor monitors. In *Astronomical Site Evaluation in the Visible and Radio Range* (edited by J. Vernin, Z. Benkhaldoun, and C. Muñoz-Tuñón), vol. 266 of *Astronomical Society of the Pacific Conference Series*, p. 278 (2002).

[126] Wiedner, M. C., Hills, R. E., Carlstrom, J. E., and Lay, O. P. Interferometric Phase Correction Using 183 GHZGHz Water Vapor Monitors. ApJ, **553** (2001), 1036. doi:10.1086/320943.

[127] Yang, H., et al. Exceptional Terahertz Transparency and Stability above Dome A, Antarctica. PASP, **122** (2010), 490. doi:10.1086/652276.

[128] Young, E. T., et al. Early Science with SOFIA, the Stratospheric Observatory For Infrared Astronomy. ApJ, **749** (2012), L17. arXiv:1205.0791, doi:10.1088/2041-8205/749/2/L17.

[129] Zemcov, M., et al. First detection of the Sunyaev Zel'dovich effect increment at λ 650 μm. A&A, **518** (2010), L16. arXiv:1005.3824, doi:10.1051/0004-6361/201014685.

[130] Zemcov, M., et al. High Spectral Resolution Measurement of the Sunyaev-Zel'dovich Effect Null with Z-Spec. ApJ, **749** (2012), 114. arXiv:1202.0029, doi:10.1088/0004-637X/749/2/114.

Publications

- M. De Petris, S. De Gregori, **B. Decina**, L. Lamagna and J. R. Pardo, Mon. Not. R. Astron. Soc. 429 (2013), 849
- S. De Gregori, M. De Petris, **B. Decina**, L. Lamagna, J. R. Pardo, B. Petkov, C. Tomasi and L. Valenziano, Mon. Not. R. Astron. Soc. 425 (2012), 222
- **B. Decina**, S. De Gregori, M. De Petris and L. Lamagna, EAS Publications Series vol. 40 pp. 107-110 (2010)